ANTHROPOGENIC HEAT FLUX ESTIMATION OVER HONG KONG – A MULTI MODELLING APPROACH

YOGESWARAN NITHIYANANDAM

Ph.D

The Hong Kong Polytechnic University

2015

THE HONG KONG POLYTECHNIC UNIVERSITY

Department of Land Surveying and Geo-Informatics

ANTHROPOGENIC HEAT FLUX ESTIMATION OVER HONG KONG – A MULTI MODELLING APPROACH

YOGESWARAN Nithiyanandam

A thesis submitted in partial fulfillment of the requirements for the degree of Doctor of Philosophy

AUGUST 2014

CERTIFICATE OF ORIGINALITY

I hereby declare that this is my own work and that, to the best of my knowledge and belief, it reproduces no material previously published or written nor material which has been accepted for the award of any other degree or diploma, except where due acknowledgement has been made in the text.

__________________________(Signed)

<u>YOGESWARAN NITHIYANANDAM</u> (Name of Student)

DEDICATION

“ I dedicate this P.hD. to God and my family “

ABSTRACT

The main objective of this study is to measure anthropogenic heat flux using satellite remote sensing, and evaluate the results using GIS-based modelling. In cities, anthropogenic heat emissions are sourced mainly for buildings, vehicles and human metabolic activities. The emissions vary significantly over time and space, and are not easily measured, so detailed models of anthropogenic heat emissions are not available for most cities. Previous studies have mainly used three approaches: inventory, energy balance enclosure, and building energy models. The present study is the first to model anthropogenic heat using three different approaches.

Thermal infrared Images from the Advanced Spaceborne Thermal Emission and Reflection Radiometer, Level 1B (ASTER, L1B) satellite are used to estimated anthropogenic heat emissions using the energy balance approach. A new technique is developed to calculate the emissivity with a higher spatial resolution. This study measures urban morphometric parameters using the Geographic Information Systems (GIS) at a much finer scale, compared to previous studies, which only calculate approximate morphometric parameters of the city. Anthropogenic heat emissions are estimated from six different ASTER images of Hong Kong captured between 2007 and 2009. These images represent diurnal (day and night) periods and seasons (summer and winter).

In this study, a global anthropogenic heat model called the Large-scale Urban Consumption of energY (LUCY) is adopted for application to Hong Kong, with the spatial resolution increased to 100 m from 2.5-arc minutes (~5-km spatial resolution). The anthropogenic heat emissions in LUCY greatly depend on population density data. Therefore, a new population scheme is introduced, in which daytime population data are included so as to consider the migration of population within grid cells at any given time. Other input parameters like energy consumption, air temperature, traffic information, and temperature schemes are also modified to match Hong Kong conditions.

A GIS-based model using a bottom-up approach is utilized to account for anthropogenic heat emitted from each building block and every road in Hong Kong. Since these emission sources are captured at a finer resolution in the GIS-based model, the model data are used as the reference for evaluating the remote sensing and LUCY models. It may be noted that the model estimations are limited to the times of satellite image acquisition (~ 11am for the day and 11pm for the night) on the given date. In addition, the anthropogenic heat values estimated using the three different models is limited to 100 m spatial resolution.

Anthropogenic heat emissions were found to be higher at day compared to nighttime emissions. Likewise, summer emissions were higher than winter ones. In all models, the highest emissions were observed in grid cells with tall commercial, business and residential buildings. Although the intensity levels differed across models, the spatial distributions remained essentially the same. Finally, a significant correlation between anthropogenic heat and UHI was noted when the results of the models were correlated with urban-morphometric parameters and ASTER surface temperature measurements. The anthropogenic heat values estimated using remote sensing agree well with those derived from the GIS-based model. However, there are certain differences in terms of advantages and disadvantages. Overall, the results from all the three models are usable as inputs to climate models. This should be useful to urban planners and other agencies in studies related to UHI.

Keywords: Anthropogenic heat; LUCY; UHI; Energy balance; Inventory method.

PUBLICATIONS ARISING FROM THE THESIS

Journal

Lindberg, F., Grimmond, C.S.B., **Yogeswaran**, N., Kotthaus, S., Allen, L., (2013). Impact of city changes and weather on anthropogenic heat flux in Europe 1995–2015, *Urban Climate*, 1-15.

Conference

Yogeswaran, N., Nichol, J.E., (2013). Estimation of net radiation over complex urban environment – A case study of Hong Kong, *34^{th} Asian conference on remote sensing (ACRS 2013)*, Bali, Indonesia. 20^{th} -24^{th} October.

Yogeswaran, N., Nichol, J.E., (2014). Estimation of anthropogenic heat flux over complex urban environment using remote sensing data, *35^{th} Asian conference on remote sensing (ACRS 2014)*, Nay Pyi Taw, Myanmar. 27^{th} - 31^{st} October (Accepted for oral presentation).

ACKNOWLEDGEMENTS

Undertaking this Ph.D. has been truly life changing and challenging experience for me. It would not have been possible to get along without the funding and directions that i received from many people.

First, thanks to God for the wisdom and perseverance that he has been bestowed upon me during this research project, and indeed, throughout my life: "I can do everything through him who gives me strength”. Predominantly, none of this would have been possible without the love and patience of my family. I would like to thank my parents for their unconditional support, both financially and emotionally throughout the life. Especially the patience and understanding demonstrated by my mother is greatly valued. A special thanks to my dad who is always a great inspirer to me.

I am immensely thankful to my Supervisor - Professor Janet Elizabeth Nichol for her support and encouragement during my P.hD. I am grateful for her aspiring guidance, invaluable constructive criticisms and advices during the research period. I am sincerely thankful to her for sharing her truthful and illuminating views on a number of issues related to the research work. Under her guidance, I have improved my personality in personal and professional life.

In the Department of Land Surveying and Geo-Informatics (LSGI), I like to thank Head of the Department, Chair of the Departmental Research Committee and all the other faculty members of LSGI for their support. Especially to Dr. Charles Wong for his valuable guidance and suggestions throughout the study period. In addition, a special thanks to Professor Bruce King who introduced me to the professional societies, which helped to extend my professional network in Honk Kong. I sincerely thank Mr. W.K. Ho the technician who was kind and regularly available to assist me for setting up instruments during fieldworks. I am too grateful to Mr. Kenneth Yau, who is also a technician for his kind service to manage my PC throughout my research period. I am truly thankful for the General Office (GO) of LSGI, the Research Office (RO), the Finance Office (FO) and the Student Affair Office (SAO) for their continuous support during the academic period.

It would not have been possible to write this thesis without the assistance and direction of Professor Sue Grimmond, Reading University, UK. To whom, I am really grateful for conceptualizing and drawing up the outline of this thesis. She have constantly guided me throughout my research along with Dr. Fredrik Lindberg (Climate Research Group, Gothenburg University, Sweden). Together I am thanking Professor Sue Grimmond and Dr. Fredrik Lindberg for inviting me to Gothenburg University, Sweden and King's College London for research collaboration.

Also wish to thank other faculty members who assisted me and comforted me at Gothenburg University, Sweden. A special thanks to Dr. Emad Farahat a visiting Professor and a neighbour who guided me throughout my stay in Gothenburg. Special thanks to Sheho (Research Student at GU), who helped me a lot during my stay in Gothenburg.

I would like to thank local and overseas Government agencies provided data that were useful for my thesis, and special mention to ENVI for providing the Evaluation Version software for my research.

Many friends have helped me stay sane through these difficult years. Their support and care helped me to overcome setbacks and stay focused on my graduate study. I greatly respect their friendship, and deeply appreciate their belief in me. I would wish to thank friends from the Tamil Cultural association of Honk Kong who made me feel staying home. A special thanks to friends from my own country who stick with me always Veda, Shiva, Anand, Annaidasan, Rajesh, Diwakar, and Dinesh.

My sincere thanks to Dr. Gopala Krishnan for being my local guardian and the advisors. In addition, a special thanks to his wife and Swathi. At this time, I would also like to thank important people like Dr. Cand Vasudevan, Dr. Yogalakshmi (a sister to me who encouraged me to pursue higher studies), and Mr.Zafar Ali (a brother and a mentor who constantly suppourted).

I also like to give thanks to my friends in our research group Imran, Bilal, Majid, Nannette, Abbas, Thom and Irteza for their valuable suggestions and support.

I am very thankful to Research Grants Council (RGC), Honk Kong for awarding me Honk Kong Ph.D. Fellowship, which helped me during my studies and gave me such wonderful opportunities for cultural and personal engagement.

Finally yet importantly, I would love to thank my dear wife for her unconditional support and encouragement during last few months.

Yogeswaran Nithiyanandam

August 2014

TABLE OF CONTENTS

GLOSSARY

AADT	Annual average daily traffic
AERONET	Aerosol Robotic Network
AHF	Anthropogenic Heat Flux
AST_LIB	ASTER Level
ASTER	Advanced Spaceborne Thermal Emission and Reflection Radiometer
ASTER GDS	ASTER ground data System
ATC	Annual traffic census
A_x	Area per grid square
BA_{UMT}	Planar area of buildings associated with different UMT's in a pixel
BC_{UMT}	Built surface cover fraction of each UMT
BT	Brightness Temperature
CDD	Cooling degree-day
CTS	Comprehensive transport study
D	Distance travelled over an hour
DN	Digital Number
E_{AHF}	Anthropogenic heat estimated using the remote sensing model
EBBR	Energy Balance Bowen Ratio method
EC	Total energy consumption in kWh
E_{car}	Average emission factors of cars
ECF	Environmental Central Facility
ECOR	Eddy Correlation flux measurement system
EC_{UMT}	Typical energy consumption of buildings associated with the UMT
E_{EBR}	Sum of components on the right side of the energy balance equations used in the remote sensing approach
EF_{m}	Speed-dependent fuel consumption factor expressed in Wm^{-1}
E_{fri}	Average emission factors of freight vehicles
E_{GH}	Ground heat flux estimated using the remote sensing approach
E_{GIS}	Anthropogenic heat estimated using the GIS model,
E_{LH}	Latent heat flux estimated using the remote sensing approach
EMDS	Electrical and Maintenance Service Department
EMFAC	Emissions fraction
EM_{major}	Emission from a major road
EM_{minor}	Emission from the minor road
E_{mot}	Average emission factors of motorcycles
EMSD	Electrical and Mechanical Engineering Services Department
E_{NR}	Net radiation heat flux estimated using the remote sensing approach
ENVI	Environmental and Visualizing Image
Es	Surface Emissivity
E_{SH}	Sensible heat flux estimated using the remote sensing approach
ETM	Enhanced Thematic Mapper
GAWSIS	Global Atmosphere Watch
GFA	Gross floor area
GIS	Geographic Information System

HDD	Heating degree-day
H_E	The hourly energy use
H_{fra}	Hourly fraction of the daily number of vehicles
HK	Honk kong
HKO	Honk Kong Observatory
HVAC	Heating, ventilation and air-conditioning
ISAC	In-scene Atmospheric Correction
ITOS-1	Improved Television Infrared Observation Satellite Program
KW	Kowloon
Lrad	Spectral Radiance
LST	Land Surface Temperature
LUCY	Large Scale Urban Consumption of Energy
L_x	Road length in m
Met_{em}	The amount of energy released per person as a function of hour of the day
METI	Ministry of Economy Trade and Industry
MMD	Min-Max Difference
MODIS	Moderate Resolution Imaging Spectroratiometer
nBA_{UMT}	Normalized building area, which is equal to the building volume divided by its mean height.
NOAA-3-5	National Oceanographic and Atmospheric Administration
NT	New territories
OMIS	Optical Multi-Channel Imaging
PD	Population density
PD(t)	Time-dependent population Density
PD_{day}	Daytime population density
PD_{night}	Night time population density
PF	Population fraction
P_t	Total population
Q_{ahf}	Anthropogenic Heat determined using remote sensing approach
Q_{bui_L}	Building Heat Component in LUCY-HK
Qgh	Ground Heat
Qlh	Latent Heat
Q_{met_L}	Metabolic Heat Component in LUCY-HK
Qnet	Net Radiation
Qsh	Sensible Heat
Q_{veh_L}	Vehicle Heat Component in LUCY-HK
RCC	Radiometric Calibration Coefficient
Rf	Field measured net radiation
Rhf	Net radiation
SAR	Special Administrative Region
SLC	Scan Line Corrector
SWIR	Shortwave Infrared
Ta	Air Temperature
T_{air}	Air temperature
TBP	Temperature balance point
T_{cf}	Comfortable indoor temperature
TES	Temperature Emissivity Separation
TES	Temperature Emissivity Separation
TIR	Thermal Infrared

T_{od}	Outdoor air temperature
TPU	Tertiary planning unit
Ts	Surface temperature
T_{sf}	Mean monthly temperature estimated relative to the balance point
Tα	Air Temperature from TIR image
UCCx	Unit Conversion Coefficient of band x
UCL	Urban Canopy Layer
UHI	Urban Heat Island
ULB	Urban Boundary Layer
UMT	Urban morphology types
V_{car}	Number of cars per 1000 people
V_{fac}	Multiplying factor used to change the total number of vehicles
V_{fri}	Number of freight vehicles per 1000 people
VHRR	Very High Resolution Radiometer
V_{mot}	Number of motorcycles per 1000 people
VNIR	Visible and Near Infrared
z	Zone corresponding to the minor road
αswb	Shortwave broadband albedo
λ_F	Frontal area
λ_P	Plane area

LIST OF FIGURES

LIST OF TABLES

Chapter 1

INTRODUCTION

1.1 Background of the study

The world is undergoing an unprecedented rate of urbanisation. By the year 2030, the world's urban population is likely to rise to 5 billion (United Nations Population Fund, 2014) from 3.9 billion, with the maximum concentrations being in Asia and in Africa. About 70% of word energy is consumed in urban areas, which accounts for around 2% of the world's land surface. Energy consumption in urban areas correlates positively with changes in urban micro-climate which contributes to raised air temperature compared to rural areas (Voogt and Oke, 2003) (Figure 1.1), with the temperature differences generally being between 1 and 3 ^{o}C (United States Environmental Protection Agency, 2013), although difference of up to 12 ^{o}C have been reported (Roth *et al.,* 1989). The magnitude of difference depends on the changes in natural heat balance due to increased anthropogenic activities within urban areas.

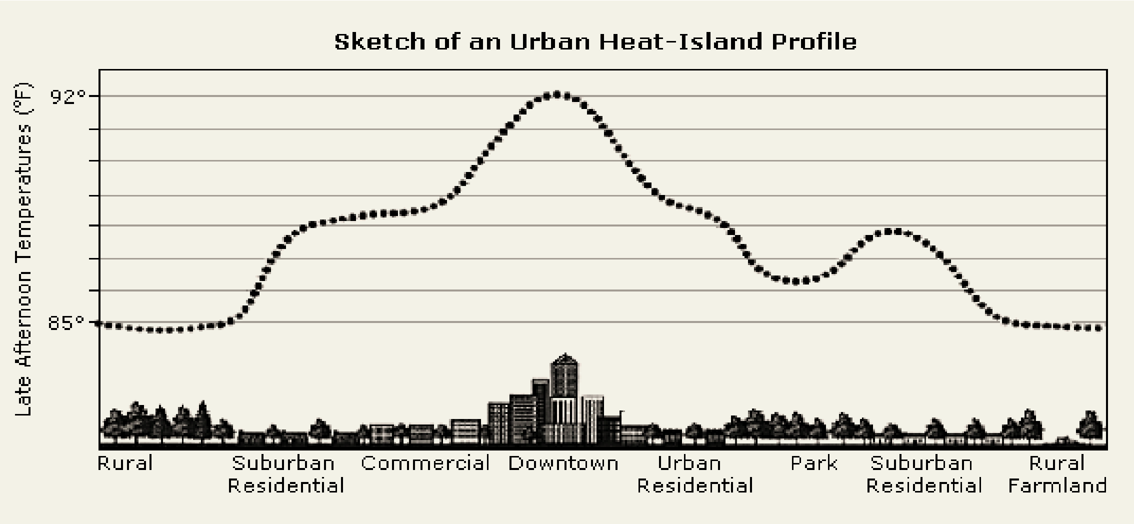

Figure 1.1 A typical urban heat island profile (courtesy: NASA)

Clearly, understanding the energy transfers within an urban system is a challenging task in view of its complexity (Figure. 1.2).

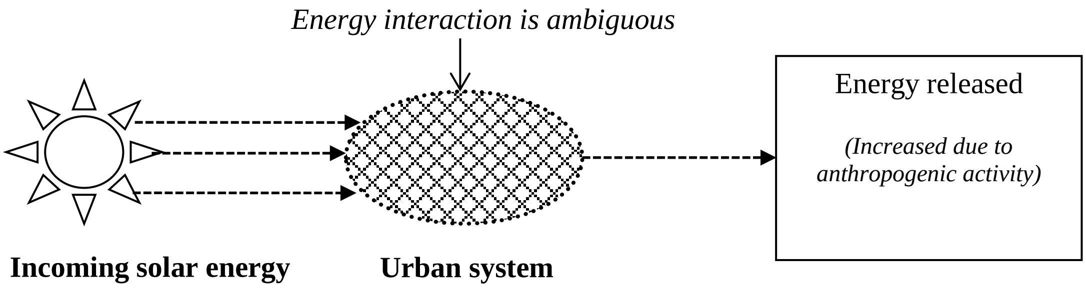

Figure 1.2 The energy process in a typical urban system.

The exchange of energy within any heat transfer system occurs through conduction, convection and radiation (Oke, 1987). In general atmospheric applications, wavelengths in the range of 0.1 to 100 μm are used; this represents a small part of the full electromagnetic spectrum.

All bodies emit radiation naturally and a body emitting the maximum possible amount of radiation at a given temperature over a unit surface area is called a black body. Emissivity is the relative ability of a surface material to emit energy by radiation. By definition, its emissivity is set equal to unity. Thus, emissivity of a given object is the ratio between the energy emitted by the surface in question and the energy emitted by a black body held at the same temperature. The magnitude of emissivity depends on intrinsic properties of the material.

Another relevant material-dependent property is albedo, which is defined as the ratio between reflected radiation from the surface and the radiation incident upon it. A perfect black body emits perfectly, so its albedo equals zero. Along with other properties, albedo and emissivity determine the net radiation over the surface, defined as the difference between the total incoming and outgoing radiations at the surface.

Thermal Conduction is the process by which heat is transmitted within a substance as a result of collision among pairs of rapidly moving molecules. This is usually an effective mode of heat transfer in solids, less so in liquids, and almost negligible in gases (Oke, 1987). In energy balance studies, conduction phenomena occur in the transportation of heat within the surface materials (emitted later as ground heat in terrestrial heat transfer).

Thermal convection on the earth (and such massive bodies) involves the vertical interchange of air masses and can only occur in liquids and gases (Oke, 1987). When an air parcel gets warmer, it becomes less dense and moves upwards. Conversely, it will descend when it is cooler.

Conduction and convection processes are the basis for sensible and latent heat fluxes. Sensible heat is the change in energy when the temperature changes. The heat required to transform from one state to another without a change in temperature is called the latent heat. The notion of an urban heat island is characterized by a large stretch of non-evaporating impervious materials covering urban areas, with a consequent rise in sensible heat flux at the expense of latent heat flux (Oke, 1987). The energy balance equation for an urban system is written by Oke (1987) as follows.

Net radiation + ***Anthropogenic heat*** = Sensible heat + Latent heat + Ground heat (1)

This equation is usually adopted in remote sensing approaches for calculating the anthropogenic heat (including that used in the present study). It can also be used to account for the common sources of anthropogenic heat: human, traffic, and building emissions. Heat emission due to human metabolism has simply been ignored in many previous studies in view of its lesser contribution (around 4%) to anthropogenic heat flux (Allen *et al.,* 2011, Sailor, 2011). However, in the present study the heat emitted from buildings, traffic and human metabolism are represented using two models (GIS and LUCY based model). The models developed in this thesis enable the mapping of anthropogenic heat distributions sensitive to space and time. The models are also capable of estimating anthropogenic heat at higher spatial and temporal resolutions than those of previous models.

1.2 Literature review

Urban development usually affects the climate layer, with effects in two layers above a city namely urban boundary layer (UBL) and urban canopy layer (UCL) (Roth *et al.,* 1989). The urban canopy layer lies below the mean roof level and consists of many microclimates produced by the heterogeneous nature of elements in the urban system. The urban canopy layer is normally coupled with the air temperature, which can be measured using fixed stations located in urban areas. The temperature differences between urban and surrounding rural locations are calculated to find the intensity of the urban heat island (UHI). Urban areas with highly dense buildings with deep street canyons and high energy consumption can result in a temperature difference, Δ (Urban - Rural), as high as 12°C (Roth *et al.,* 1989). The UHI is mainly caused by the combination of anthropogenic heat discharge due to energy consumption, increased impervious surface area, and decreased vegetation and water area (Kato and Yamaguchi, 2005). Quantifying anthropogenic heat discharge and studying its spatial pattern, is important to improve the understanding of human impacts on the urban environment, a vital issue in global climate change (Zhou *et al.,* 2012).

1.2.1 Remote sensing of urban heat island

Roth *et al.,* (1989) note that the first satellite-based UHI study was conducted in the Eastern United States of America using data from the Improved Television Infrared Observation Satellite Program (ITOS-1) with its sensor being used as a thermal scanning radiometer, with a resolution of 7.4 km. Subsequently, in their study of 50 cities in the US, Carlson and Boland (1978) used the National Oceanographic and Atmospheric Administration (NOAA-3-5) satellite carrying the Very High Resolution Radiometer (VHRR) sensor with a resolution of 1 km. Later, Landsat and ASTER (Advanced Spaceborne Thermal Emission and Reflection Radiometer) satellites were used in UHI studies (Nichol, 2005; Nichol, 2009). Landsat ETM+(Enhanced Thematic Mapper) has 7 spectral bands, with its spatial resolution ranging between 15 and 60 m and a 185 km image swath while ASTER has 14 spectral bands straddling the visible to the thermal infrared ranges with 15 to 90 m spatial resolution and a 60 km image swath. ETM+ has thermal bands at 60 m with better spatial resolution compared to ASTER's 90 m but, since 2003, the usage of ETM+ has been limited due to a scan line corrector (SLC) problem. Also, more bands in thermal infrared region enables ASTER's sensitivity to surface heat fluxes compared with Landsat.

1.2.2 Anthropogenic heat flux estimation using remote sensing

Remote sensing strategies were not common in the past for measuring anthropogenic heat flux (AHF) using the energy balance approach. Because of the complexity and challenges involved in obtaining input surface morphometric data. Kato and Yamaguchi (2007) used the energy balance approach for measuring anthropogenic heat on the assumption that AHF should be the active energy component. Xu *et al.* (2008) used a similar energy balance equation but considered that the anthropogenic heat flux is in the forms of increased sensible and latent heat values. This enabled them to sidestep anthropogenic heat as a component of energy balance. Recent studies (Zhang *et al.*, 2013; Zhou *et al.*, 2012) also considered anthropogenic heat as an individual component of energy balance. The surface morphometric parameters are roughly estimated to simplify the calculation as similar to Kato and Yamaguchi (2007).

Although the methods used to calculate net radiation are quite similar in these studies, those used in calculating albedo and emissivity differ significantly because these variables depend directly on the prevailing surface properties. The albedo values are determined from the regression equation identified by Liang (2001) in studies conducted by Kato & Yamaguchi (2007) and Kato *et al.* (2009). On the other hand, Xu *et al.* (2008) use OMIS-derived broadband albedos. The Liang (2001) method can be directly applied over ASTER images to get TOA albedo, extracting surface albedo requires atmospheric corrected radiance image as input. The need for atmospheric correction of spectral bands before calculating albedo values was not recognised adequately in previous studies. These studies depended mostly on predefined models available in radiative transfer codes. Since such an approach may not be suitable for all locations, there is a need to define aerosol and atmospheric conditions based on local measurements.

Emissivity is the other important factor in estimating net radiation. Kato & Yamaguchi (2007) follow the equation suggested by (Liang, 2001) to determine broadband emissivity values while Xu *et al.* (2008) adopt the Temperature Emissivity Separation (TES) method (Gillespie *et al.*, 1998) used in several previous studies. However, the spatial resolution of emissivity estimation using TES method was 90 m, which is considered too coarse for a complex urban environment. Therefore, there is a need for estimating emissivity at finer resolution than the 90 m to precisely map urban surface emissivity.

Brutsaert's (1992) formula to calculate sensible heat is widely used in remote sensing approaches. By contrast, the method for calculating aerodynamic resistance varies across different studies. Grimmond and Oke (1999) compare the roughness parameters calculated using different methods, discussed the merits of morphometric and wind-based aerodynamic parameters estimation. Also recommended choice of method to estimate displacement height and roughness lengths in urban areas and their magnitude. Xu *et al.* (2008) use GIS (Geographic Information System) datasets to calculate roughness parameters on the basis of mean building heights in different cells as calculated from the aforementioned SISM (Shangai Institute of Surveying & Mapping) map. The friction velocity for each cell (with stability corrections) is derived from measurements at the meteorological station, along with the LUMPS-derived estimate of sensible heat for each grid cell. In this process, the mean LUMPS-derived values of all shadow-free pixels within each cell are used to initialize iterative calculation of friction velocity (Grimmond & Cleugh, 1994). The stability corrections needed with respect to momentum and heat are captured by certain functions, ψ_m and ψ_h, respectively (Paulson, 1970) along with the equation proposed by Dyer (1974) and modified later by Högström (1988). The roughness lengths for momentum and heat transport (z_{0m} and z_{0h}, respectively) are calculated by applying the method suggested by Voogt & Grimmond (2000), whereas Kato & Yamaguchi (2005) use the same values across the entire study area. The stability correction function depends on the Monin-Obukhov length (Brutsaert, 1982). The functions include von Karman's constant, k, which is set equal to 0.4. Typical values are used for the roughness lengths, z_{0m} and z_{oh}, on the basis of the surface types

(Brutsaert, 1982). Finally, the roughness lengths associated with all the resulting pixels are averaged logarithmically to get average roughness of the study area.

In view of its very high building density, calculating aerodynamic resistance values from certain thumb rules and approximations is too simple an approach for a city like Hong Kong. Therefore, there is a need to develop a method capable of accounting for the surface and the morphometric properties of buildings at a finer spatial resolution. This problem is addressed in the present study by utilizing surface feature data gathered from GIS while estimating the aerodynamic resistance.

Estimations of latent heat and ground heat were combined as storage heat by Xu et al (2008) since it was considered difficult to split the two during computation. In general, it is difficult to determine ground heat from remote sensing data. However, it can be calculated from data on surface cover fractions. In contrast to previous studies, which extracted surface cover fractions from the respective land use maps, our study estimates surface cover from the visible bands as suggested by Clothier *et al.* (1996). This method allows mapping surface fractions at the image time, which is more appropriate to the calculation of ground heat.

1.2.3 Numerical modelling approaches for anthropogenic heat

Numerical modelling is commonly used for estimating AHF. Urban anthropogenic heat generation has been modelled for a number of cities around the world. Generally a horizontal grid is used although some have added the third (vertical) dimension. The resolution varies from 100 m^2 (Grimmond, 1992; Pigeon *et al.,* 2007), and 200 m^2 (Smith *et al.,* 2009), to 250 m^2 (Ichinose *et al.,* 1999). Klysik (1996) estimates emissions at local area level using different cell sizes based on land use polygons. Others focus on individual city blocks and take into account building geometries and the temperature changes at different heights above ground (Kondo and Kikegawa, 2003).

At the other extreme, lower resolution grids are used to examine larger areas. For example, Makar *et al.* (2006) use several global datasets centred on North America, at a scale of about 15 km^2 while Flanner (2009) creates a global model with 0.5° × 0.5° cells (3,091 km^2 at the equator). Flanner also estimates heat fluxes over land areas without discriminating between urban and rural land uses. However, the heat inputs from individual cities may have been greatly underestimated because of the size of the grid cells (Allen *et al.,* 2011), therefore local high anthropogenic heat fluxes arising from urban areas may not be represented by this model. In the present study, two models are created with a spatial resolution of 100 m^2. Further improvement in spatial resolution would be possible only after a dataset with finer resolution becomes available.

The majority of the models available are based upon the following simple partitioning (Metabolic heat + Building heat + Vehicle heat) of the sources of anthropogenic heat flux (Grimmond, 1992; Sailor and Lu, 2004).

The components are described below individually.

1.2.3.1 Metabolic heat emission

Humans release heat continuously as a result of metabolic processes (Sailor and Lu, 2004). The treatment of metabolic heat varies from non-inclusion when its contribution is small relative to the total anthropogenic heat (Pigeon *et al.,* 2007), to just documentation of the term, e.g., as in Lee *et al.* (2009), to not explicitly including it, e.g., as in Flanner (2009). Ichinose *et al.* (1999) could not incorporate a metabolic heat (QM) into their model of Tokyo because the city was too difficult to map, although it was later recognized that this omission, amongst other excluded elements, contributed to an underestimation of anthropogenic heat (QF) (Allen *et al.,* 2011; Sugawara and Narita, 2009).

Estimates of QM are commonly based on population statistics. For example, fine-scale census data were used for Vancouver (Grimmond, 1992) and Manchester (Smith *et al.,* 2009), although the UK census data used for Manchester were gathered in 1991, some 18 years earlier than the year of publication of the results. As for US cities, Sailor and Lu (2004) used census data but allowed the population density to change over space and time. Makar *et al.* (2006) used a global population density grid with a 2.5 × 2.5 arc-minute resolution. Metabolic heat emissions were determined from the population data by using the average human metabolic rate. Metabolic processes are known to vary with human activity, with the average person emitting around 70 W of heat while sleeping and up to 800 W while engaged in strenuous exercise (Smith *et al.*, 2009). Most models assume a constant rate of 100 W per person (e.g., Makar *et al.*, 2006), which does not take account of diurnal variability, or have a defined diurnal cycle (Grimmond, 1992; Sailor and Lu, 2004; Smith *et al.*, 2009). Sailor and Lu (2004) assumed a constant (between 23:00 and 05:00) metabolic rate of 75 W per person, and a daytime (between 07:00 and 21:00) rate of 175 W per person, with transitional values for the hours in between. Similar time periods were considered by Smith *et al.* (2009), although the night-time value was 70 W and the daytime value was 250 W. Grimmond (1992) divided each day into two parts with night-time as 23:00 to 07:00 and daytime as 07:00 to 23:00.

1.2.3.2 Vehicle heat

Fuel combustion is the main source of heat from motor vehicles (Pigeon *et al.*, 2007). There is a strong diurnal cycle with vehicular traffic. This has been well documented in traffic count data, with peaks in the morning and early evening. This observation has been included in several models (Sailor and Lu, 2004; Lee *et al.*, 2009; Smith *et al.*, 2009). As with *Q*M (metabolic heat), traffic patterns generally do not vary between seasons (Sailor and Lu, 2004). A much broader range of methods has been used to calculate *Q*V (vehicle heat) than for *Q*M, which includes both bottom-up, and top-down approaches. In some countries, information on the distances the vehicles are driven each day is collected, and the resulting statistics are utilized in models. Sailor *et al.* (2007) use the average distance travelled per person for US cities while calculating total vehicle distances from population data. The diurnal cycle is estimated from hourly traffic counts using the values associated with roads within the grid cells of various cities. Sailor and Lu (2004) also apply this bottom-up approach and recommend the use of a diurnal profile based on Hallenbeck *et al.* (1997) as a top-down approach whenever detailed traffic data are not available. This accounts for the different patterns observed on weekends and weekdays. Lee *et al.* (2009) use travelling distance statistics, but these are calculated per vehicle so the numbers of licensed vehicles in the area are also required. The most comprehensive bottom-up approach to modelling *Q*V is the one used for Manchester by Smith *et al.* (2009). Detailed traffic count data, which recorded the average traffic density on various types of roads (major, minor, motorway), the types of vehicles (motorcycles, cars, buses and large goods vehicles) and fuel type (petrol and diesel) are used. As soon as the numbers of vehicles and travel distances have been allocated spatially (for all models), the value of *Q*V is estimated with certain assumptions concerning fuel consumption, average speed, fuel economy, and fuel type. The values cited for the amount of energy released from fuel combustion in the UK include 45.85 kJ g^{-1} for petrol and 46 kJ g^{-1} for diesel in the UK (Smith *et al.* 2009); and 43.8 kJ g^{-1} for petrol and 42.5 kJ g^{-1} for diesel in France (Pigeon *et al.,* 2007). An average of 45 kJ g^{-1} over an entire fleet was found by Sailor and Lu (2004 and Sailor *et al.* (2007). Unlike with previous models, the model of Lee *et al.* (2009) estimates fuel emissions on the basis of volume (an average of 34.3 MJ l^{-1}) rather than the mass of fuel consumption.

Top-down approaches have used total annual energy consumption values for the transport sector, which are distributed across the year with diurnal and seasonal changes (Ichinose *et al.,* 1999) and then mapped to the roads within the grid assuming a uniform *Q*V for every road.

1.2.3.3 Building heat

Top-down and bottom-up approaches to *QB* have also been employed (Heiple & Sailor, 2008). Annual energy consumption statistics over a large area are frequently used in top-down approaches, which are then distributed over the year according to the time and season. By contrast, bottom-up methods generally use energy data at much finer scales (usually hourly) for single buildings, which are then scaled appropriately in terms of sector categories: industrial, commercial and residential; and residential and non-residential (Pigeon *et al.,* 2007; Hamilton *et al.,* 2009), and fuel types: electricity, and other sources of building heat (Sailor and Lu, 2004). Models adopting the highest resolutions use records of hourly energy consumption by buildings or annual energy consumption over very small areas. Top-down low-resolution approaches utilize annual energy consumption totals.

Bottom-up methods mainly utilize land-use grids or floor space statistics and convert them into heat emission estimates. For example, Smith *et al.* (2009) applied two different diurnal and seasonal cycles by considering whether the land use is domestic or non-domestic. By contrast, Sailor *et al.* (2007) use groups of buildings with similar characteristics and floor spaces with appropriate time-dependent diurnal and seasonal profiles for each building type.

Data from countries (Flanner, 2009), states (Sailor and Lu, 2004), and other statistical areas (Hamilton *et al.*,2009) have been used by creating grids of between 1 sq.km to city wide, to which daily and seasonal cycles are applied. For example, Flanner (2009) uses country-level annual totals of non-renewable energy consumption disseminated by population density (a technique also used by Makar *et al.*, 2006). The amplitude of the annual cycle, based on day of year and latitude, is found to increase with distance from the equator. Information for every location and the same diurnal cycle is obtained by emulating Sailor and Lu (2004). Ichinose *et al.* (1999) distributed annual energy data, using both diurnal and seasonal cycles as functions of building height and business type. The timeliness of data is important as changes in technology result in changes in energy use. Extensive computer use and advances in technology such as mobile phones and personal music players (which have to be charged directly from an electricity supply rather than use disposable batteries) have shown that energy consumption has increased substantially in recent times, especially in the richest countries.

A key assumption often made by *Q*F models is that no time lag occurs between energy consumption and heat emitted. This is because detailed information on the ventilation systems and fabric of buildings needed to estimate the time delay is not generally available (Smith *et al.*, 2009). Heiple and Sailor (2008) compare two approaches towards estimating *Q*B in Houston over grids with the similar scale. It is found that bottom-up calculations produce greater time lags and more severe peaks in heat emissions than those generally observed when top-down approaches are adopted. Although the differences between average values of QB for the two methods are smaller than 3% over entire cities, bottom-up methods show much greater spatial variation with peak values up to 20 times greater (Heiple and Sailor, 2008).

The temperature often considered to be the most comfortable for internal building air is 18 °C (Klysik, 1996). The outdoor temperature, which influences this indoor temperature in buildings, is known as the 'balance point' because the climate-dependent energy demand is lowest at that point (Amato *et al.,* 2005). As the outdoor temperature increases or decreases, heating or cooling energy is required, so energy consumption rises proportionately with temperature (Ruth and Lin, 2006). This balance point can vary between residential and commercial sectors. Amato *et al.* (2005) estimate a monthly outdoor temperature of 15.5 °C as the balance point for residential buildings, and approximately 12.75 °C for commercial buildings (Allen *et al.*, 2011).

Two models are developed in the present study: one based on a top-down approach downscaling the LUCY global anthropogenic heat model, and the other based on a bottom-up approach using GIS datasets. The spatial resolutions associated with the outputs from these models are limited to 100 m. The algorithms used will be summarized in later chapters.

1.2.4. Need for the present study

Anthropogenic heat discharge has a significant impact on the urban thermal environment (Zhang *et al.,* 2012). It contributes to UHI formation with the combination of decreased vegetation cover and increased use of artificial impervious surface materials such as concrete and asphalt (Kato and Yamaguchi, 2005). The UHI results in increased energy consumption, outbreaks of epidemics, heat strokes, and change in urban thermal environment. Since Hong Kong suffers badly from the UHI effect, it is essential to have an understanding of anthropogenic heat distribution. A precise mapping of anthropogenic heat is, therefore, required in order to mitigate the UHI.

1.2.5 Highlights of the study

Newcombe (1975) analysed the spatial distribution of energy consumption in Hong Kong at coarse resolution (by estimating total end-use energy consumption at each sector). Estimated artificial heat (anthropogenic heat) using a one-dimensional, time - dependent model called the Myrup model (Myrup, 1969), based on the energy balance equation. The present study estimates anthropogenic heat at higher spatial and temporal resolutions than before. The remote sensing results are evaluated using a high-resolution GIS-based model, which was not in the case of previous studies. The algorithm used in all three models (Remote sensing model, GIS model and LUCY model) are tailor made for the morphometric and climatic conditions of Hong Kong. The results of the study can be used as an input to the climate models and will be useful for city planners and in studies related to climate research.

1.3 Research objectives

The primary objective of this study is to develop and evaluate a remote sensing based method for estimating *anthropogenic heat flux over Hong Kong at high spatial and temporal resolutions*

The secondary objectives are:

- *Develop a new simplified method for estimating surface emissivity at a finer spatial resolution than existing methods using daytime ASTER satellite imagery.*
- *Identify suitable atmospheric correction technique for ASTER thermal images acquired over a humid and polluted atmosphere such as Hong Kong.*
- *Evaluate the robustness of the remote sensing model using spatial distribution characteristics of the GIS model.*
- *Develop a numerical model to map anthropogenic heat for any period of the day using simple datasets.*
- *Estimate the relative contribution of anthropogenic heat to the urban heat island effect spatially over Hong Kong and its relationship to urban morphology.*

1.4 Dissertation overview

- Chapter 2 discusses the study area and the data used including meteorological, geospatial and GIS datasets.
- Chapter 3 describes the spatial and temporal characteristics of anthropogenic heat estimated using ASTER Level 1B images acquired between 2007 and 2009 at different seasons and periods (day-time and night-time). It also describes the improvements made in the methods of calculation for estimating various components of the energy balance approach.
- Chapter 4 summarizes the methods used for high-resolution estimation of anthropogenic heat using the GIS model. In addition, the spatial and temporal characteristics of anthropogenic heat as estimated at the satellite overpass times are discussed.
- Chapter 5 discusses the methods used while customizing global anthropogenic heat models based on the LUCY model. It also discusses the improvements and modification made to suit local conditions in Hong Kong.
- Chapter 6 compares the results of anthropogenic heat estimation using different modelling techniques and identifies its relationship with the urban heat island effect and urban morphometric parameters.
- Chapter 7 presents the overall conclusions drawn from the thesis along with recommendations for future researchers.

Chapter 2

STUDY AREA AND DATA USED

2.1 Study area

Hong Kong is a Special Administrative Region (SAR) of the People's Republic of China. Geographically, it extends between 22^{o} 08' and 22^{o} 35'North Latitude and 113^{o} 49' and 114^{o} 31' East Longitude (Figure 2.1). Its landmass covers 1,104 sq. km, with about 24 % of built-up areas. In 2013, the population of Hong Kong reached 7.2 million with a density of 6,480 people per sq. km (Census and Statistics Department, 2011). The SAR consists of the Hong Kong Island, the Kowloon peninsula, the New Territories and includes 262 outlying Islands. Hong Kong is situated in a region where both tropical and mid-latitude weather phenomena are experienced (Ginn *et al.*, 2004). Just as with many tropical weather systems, cyclones and troughs of low pressure are common, whereas cold surges are frequent during winter as in many mid-latitude regions. The particularly high temperatures observed in urban areas as a result of the UHI effect have been studied by researchers for over a decade. As Hong Kong is among the tropical cities suffering a strong UHI effect. It provides an ideal for the study of anthropogenic heat, a main cause of the UHI.

2.2 Data used

This study models anthropogenic heat using three different approaches. The majority of data were obtained through primary (e.g., remote sensing, statistical and GIS data), and secondary data (e.g., satellite derived air temperatures, in situ surface temperatures, and measured net-radiation values). These are discussed under three headings: meteorological data, geospatial data, and other data.

2.2.1 Meteorological data

Surface meteorological data related to temperature, solar radiation, dew point, relative humidity, and visibility were obtained from the weather stations maintained by the Hong Kong Observatory (HKO) and the Environmental Central Facility (ECF) of Hong Kong University of Science and Technology.

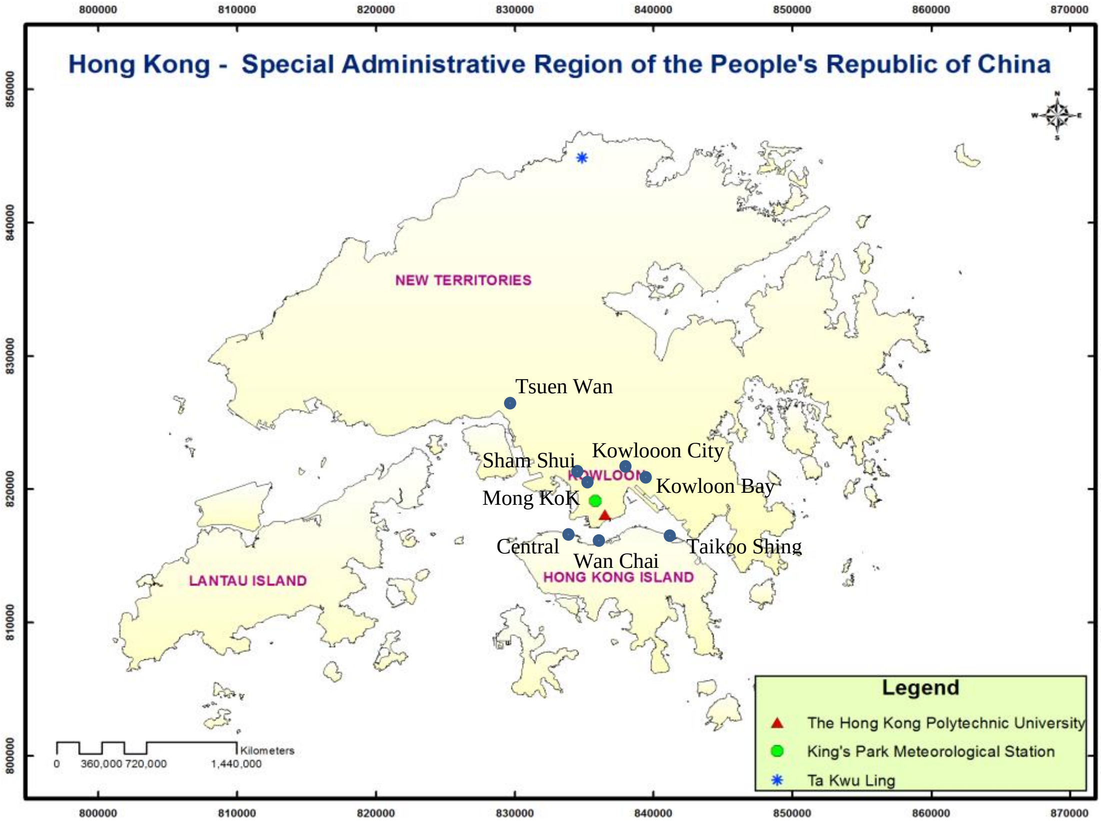

Figure 2.1 The study area and locations of AERONET stations (The Hong Kong Polytechnic University), Ozonesonde measurements (King's Park meteorological station) and net radiation measurements (Ta Kwu Ling).

Data on the upper atmosphere were based on the ozonesonde measurements carried out at King's Park (WMO Station 45004) (Figure 2.1) as downloaded from the Global Atmosphere Watch (GAWSIS) website. Aerosol details were based on measurements carried out by the NASA AERONET sunphotometer located at the Hong Kong Polytechnic University (Figure 2.1).

Other meteorological data like net-radiation, in situ surface temperatures, etc. were obtained from measurements carried out by a net radiometer and thermocouple, respectively. The CNR1 of Kipp & Zonen, the net radiometer utilized, measures incoming and outgoing shortwave and long infrared radiation using four sensors (two pointing up and two pointing down), with a ± 10 % accuracy and a directional error smaller than 25 W m^{-2}. In situ surface and air temperatures were measured using 2-channel, handheld thermometers with a ± 0.1 % + 0.7 ^{0}C accuracy. Net-radiation data were obtained from Fung *et al.*, (2011). In situ air temperature data were taken from Nichol and Wong (2008).

2.2.2 Geo-Spatial data

The geospatial data used in the study were categorized as remote sensing and GIS data.

2.2.2.1 Remote sensing data

Infrared images over Hong Kong were obtained by the ASTER (Advanced Spaceborne Thermal Emission and Reflection Radiometer) instrument of the Terra satellite launched into a sun-synchronous Earth orbit on December 18, 1999 (it actually started to function fully only in February 2000). ASTER is a cooperative effort between NASA and Japan's Ministry of Economy Trade and Industry (METI). It captures data with a high spatial resolution and is organized into 14 bands, starting from the visible to the thermal infrared wavelengths. It also provides a stereo viewing capability for digital elevation model creation. ASTER is used by Terra as its zoom lens by carrying space-borne instruments for validation and calibration. It has three subsystems: visible and near Infrared (VNIR), shortwave infrared (SWIR), and thermal infrared (TIR). Band specifications for ASTER are given in Table 2.1. ASTER's own instruments and others with similarly high spatial resolutions and earth-observing capabilities provide data useful to a wide range of scientific research studies and applications, e.g., land surface climatology, volcano monitoring, hazard monitoring, hydrology, geology and soils. Table 2.2 lists the main details related to the ASTER products used in the study. Figure 2.2 clarifies the atmospheric transmission of ASTER bands at each wavelength. Note that, in the SWIR and TIR wavelengths, ASTER images have spectral resolutions superior to those of Landsat.

Table 2.1. ASTER band specifications

Band region	Band no	Spectral range (μm)	Spatial resolution (m)	Quantization level
VNIR	1	0.52 - 0.60	15 m	8 bits
	2	0.63 - 0.69		
	3N	0.78 - 0.86		
	3B	0.78 - 0.86		
SWIR	4	1.60 - 1.70	30 m	8 bits
	5	2.145 - 2.185		
	6	2.185 - 2.225		
	7	2.235 - 2.285		
	8	2.295 - 2.365		
	9	2.360 - 2.430		
TIR	10	8.125 - 8.475	90 m	12 bits
	11	8.475 - 8.825		
	12	8.925 - 9.275		
	13	10.25 -10.95		
	14	10.95 -11.65		

Source: ASTER user handbook, ver.2.page no. 10.

Table 2.2. Details of ASTER products used in this study

Parameter	Description
Product-level	Level 1B – Registered radiance at the sensor
Sensor altitude	705 km
Sensor capability	Day (full mode) and night (TIR only)
Product deliverable format	EOS HDF
Projection used	UTM 49 N
Data Provider	ASTER GDS Japan

Source: Header file associated with ASTER Level 1B data.

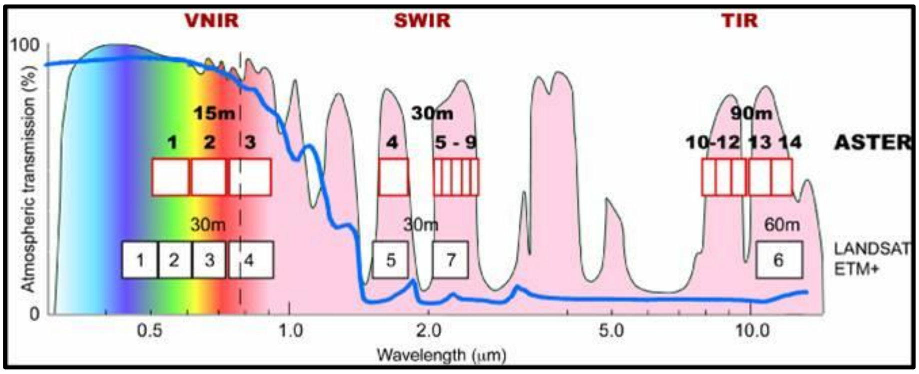

Figure 2.2 ASTER bands superimposed on model atmosphere (Courtesy NASA)

2.2.2.2 GIS data

The GIS data used in this study were obtained from government departments. Thus the land use and 3-D building datasets were obtained from the Hong Kong Planning Department. Data on road networks and information as collected by traffic measurements stations were obtained from the Transport Department of Hong Kong. Information on tertiary planning and district boundaries was obtained from the Census and Statistics Department of Hong Kong.

2.2.3 Other data

Other data collected included statistical data and data from global sources. Demographic data were taken from the records of the Census and Statics Department. The data concern the major population segments (population density, workers and students), energy consumption values for each month, and the numbers of workers by sector. The Energy end-use (final energy consumed by Residential, Commercial, Industrial and Transport) data were taken from the Electrical and Maintenance Services Department of Hong Kong (EMSD). Data on typical emissions from vehicles of each type along with the corresponding number of vehicles and fuel types were taken from the Environmental Protection Department of Hong Kong.

Some of the data used by the LUCY model were taken from global sources. Among such data were the list of public holidays, the boundary of the study area, and emission factors.

Chapter 3

ANTHROPOGENIC HEAT FLUX MODELLING OF HONG KONG USING A REMOTE SENSING APPROACH

3.1 Introduction

In this study, anthropogenic heat emissions are estimated by applying an energy balance enclosure approach to data provided by the Advanced Spaceborne Thermal Emission and Reflection Radiometer (ASTER) of the Terra satellite. Anthropogenic heat is calculated as a residual causing imbalance in the energy balance equation. In other words, there is excess heat when the net radiation (the balance between incoming and outgoing energies at the surface) is subtracted from the sum of sensible heat (fluid movement of heated air), latent heat (chemical energy due to phase change) and ground heat fluxes (thermal conductivity). In the absence of anthropogenic heat emission, net radiation should be equal to the sum of sensible, latent and ground heat fluxes.

Oke (1987) modified the natural energy balance equation by including anthropogenic heat (Q_{ahf}) in addition to net radiation (Q_{net}) as the sources of energy in the energy balance equation (Equation 3.1). The equation can then be rearranged to yield anthropogenic heat as a residual (Equation 3.2).

$$Q_{\mathrm{net}} + Q_{\mathrm{ahf}} = Q_{\mathrm{sh}} + Q_{\mathrm{lh}} + Q_{\mathrm{gh}} \tag{3.1}$$

$$Q_{\mathrm{ahf}} = Q_{\mathrm{sh}} + Q_{\mathrm{lh}} + Q_{\mathrm{gh}} - Q_{\mathrm{net}} \tag{3.2}$$

where Q_{sh}, Q_{lh}, and Q_{gh} are the sensible, latent and ground heat fluxes, respectively. This approach is widely used for estimating anthropogenic heat over a small area from micrometeorological data (sensible, latent and ground heats are measured using instruments). A limited number of studies have applied the method to remote sensing images, e.g., Kato and Yamaguchi, 2005; Kato *et al.*, 2008; Oke, 1988; Zhou *et al.*, 2012; and Zhang, 2013. These studies used thermal infrared (TIR) images of ASTER and Landsat with spatial resolutions 90 m and 60 m, respectively. Xu *et al.* (2008) used the OMIS (Optical Multi-Channel Imaging Sensor) hyperspectral imagery of 6 m resolution to demonstrate urban sensible heat flux over London and Shanghai. However, they did not estimate anthropogenic heat as a separate component. The method used in the present study is capable of measuring urban anthropogenic heat at a relatively fine spatial resolution (30 m) from daytime ASTER images. The study focuses on the Kowloon Peninsula, a highly urbanized area in Hong Kong which experiences a strong urban heat island effect. A Δt (u − r) of 7 to 8 ^{0}C has been observed on ASTER night time images (Wong and Nichol, 2011).

Anthropogenic heat emissions have been estimated in this study on the basis of six different images (Table 3.1) taken over Hong Kong by ASTER L1B. Three were captured during daytime (30th November 2007, 13th September 2008, and 22nd August 2009). The others were taken under night-time anthropogenic heat conditions over the Kowloon peninsula on 31st January 2007, 13th August 2008, and 17th September 2009. Images dated 31st January 2007, and 30th November 2007 represented winter conditions while the rest were timed to represent summer conditions.

Table 3.1 Details of ASTER L1B images used in this study

S.no	Date	Time (HK)	Diurnal period	Season
1	31st Jan 07	22.42	Night	Winter
2	30th Nov 07	11.03	Day	Winter
3	13th Aug 08	22.42	Night	Summer
4	13th Sep 08	11.04	Day	Summer
5	22nd Aug 09	11.09	Day	Summer
6	17th Sep 09	22.42	Night	Summer

Both the emissivity and albedo (reflection coefficient) are important parameters in calculating net radiation. They depend on the properties of surface materials at the time of acquisition. A new technique is used in this study to calculate emissivity values at a higher spatial resolution than the thermal image. This in turn enables mapping surface temperatures and net radiation values at a much finer spatial resolution (30 m). Temperatures so estimated are validated against surface temperatures measured in the ground by thermocouple data loggers recorded during satellite overpass time.

The albedo values are calculated using images corrected for atmospheric absorption and scattering. Without such atmospheric correction, temperature errors in the range of 4 to 7 ^{0}C may occur (Voogt and Oke, 1998; Weng *et al.*, 2008). The methods used for atmospheric correction are given in Section 3.2.1.2.

It is difficult to calculate sensible and latent flux values over a complex urban environment from satellite images due to the complexity in estimating roughness parameters. The studies (Kato and Yamaguchi, 2005; Kato *et al.*, 2008; Zhou *et al.*, 2012; Zhang 2013) have approximately calculated the roughness parameters needed to estimate the heat components in the energy balance equation. The present study estimates roughness parameters using the morphometric method (Brutsaert, 1982; Voogt and Grimmond, 2000), on a Geographic Information System (GIS) platform. The anthropogenic heat values are estimated using the remote sensing approach including all known emissions within a pixel, at satellite overpass time with spatial resolution of 30 m. However, the figures are resampled to 100 m in order to evaluate the results against those from other models.

The ASTER Level 1B (AST_L1B) data for the present study were obtained from ASTER GDS (ASTER ground data system) which includes a ground system to control ASTER's operations, data processing, data archive and data distribution. Meteorological data were obtained from the Hong Kong Observatory (HKO). Aerosol information for the atmospheric correction was retrieved from the AERONET station located at the Hong Kong Polytechnic University and downloaded from the website (http://aeronet.gsfc.nasa.gov/new_web/data.html).

The next section describes the methodology used to estimate the different parameters involved in the estimation of energy balance components.

3.2 Methodology

The main steps in anthropogenic heat measurement using satellite imagery are described below

3.2.1 Image Pre-processing

The satellite image pre-processing usually comprises a series of sequential operations: atmospheric correction, image registration, geometric correction, and masking. The ASTER Level 1B images used in this study are produced by applying radiometric calibration, and geometric corrections to the Level- 1A (unprocessed instrument data) image as described below. The individual channels of AST_L1B images are extracted using the HEG (HDF-EOS to Geo TIFF) conversion tool.

3.2.1.1 Application of digital number (DN) to spectral radiance

The at sensor radiance values at different wavelengths are stored as digital numbers (DN) for convenience during data storage and transfer (see ASTER's user handbook). The DN values are converted into spectral radiance values using the following equation

$$L_{\mathrm{rad},\,x} = UCC_x\,(DN_x - 1) \tag{3.3}$$

where L_{rad} is the spectral radiance of band x, and UCC_x is the unit conversion coefficient of band x (Table. 3.2).

Table 3.2 Unit Conversion Coefficients (UCC) to convert DN into spectral radiance

Band	Unit Conversion Coefficient (W m^{-2} sr^{-1} μm^{-1})			
	High gain	Normal gain	Low gain 1	Low gain 2
1	0.676	1.688	2.25	N/A
2	0.708	1.415	1.89	
3N	0.423	0.862	1.15	
3B	0.423	0.862	1.15	
4	0.1087	0.2174	0.290	0.290
5	0.0348	0.0696	0.0925	0.409
6	0.0313	0.0625	0.0830	0.390
7	0.0299	0.0597	0.0795	0.332
8	0.0209	0.0417	0.0556	0.245
9	0.0159	0.0318	0.0424	0.265
10	N/A	0.006822	N/A	
11		0.006780		
12		0.006590		
13		0.005693		
14		0.005225		

Source: ASTER user handbook Ver.2, 2014

The *UCC* value for each band represents the gain setting used during image acquisition, which can be known from the header file associated with AST_L1B.

3.2.1.2 Atmospheric corrections

In this study, the atmospheric component of the AST_L1B product (from TIR images) is removed using an In-Scene Atmospheric Compensation algorithm (ISAC) implemented using the ENVI (Environment for Visualizing Images) image processing software (Johnson and Young, 1998; Hernandez, 2000).

The VNIR and SWIR bands of the AST_L1B product are subjected to atmospheric correction using the 6S (Second simulation of the satellite signal) radiative transfer code. Which was used to calculate the lookup table needed by the MODIS (moderate resolution imaging Spectroradiometer) atmospheric correction algorithm (Vermote, 1997; Kotchenova, 2006). The present study uses the most recent 6S vector model (6SV1.1) which requires inputs on geometric and atmospheric conditions, aerosol detail, and sensor details of the ASTER images.

The atmosphere and aerosol submodels available as RT codes are defined for particular regions of the world. For example, models for tropical atmospheres in RT models represent the atmospheric conditions prevailing over tropical regions, and the urban aerosol model represents aerosol types over urban areas. However, in reality, atmospheric conditions of all tropical regions are not similar, i.e., the actual atmosphere may not conform to the expected water vapour and temperature profiles for a specific time and place (Carr, 2005). Likewise, aerosol types are not similar over all cities, i.e., the aerosol models do not necessarily exhibit similar optical properties over a given urban area at a specific time and date. Therefore, the atmosphere and aerosol conditions need to be determined from local measurements carried out at the time image time, such as from an AERONET station.

The images used in this study were atmospherically corrected using two aerosol models: a) a predefined urban aerosol model, and b) a user-defined aerosol model based on local AERONET measurements. The atmospheric conditions are captured using two models): a predefined model (refer to Section 3.2.1.2.1) and a user-defined model based on Ozonesonde measurement. The correspondence between the predefined model and local measurements (user defined) is evaluated by comparing results from the models. Predefined models are simpler to use than user-defined ones that require several input parameters to define aerosol and atmospheric conditions, but may be less accurate.

Not all predefined models available in 6S V.1 were used for testing the agreement of the predefined models with the user-defined models. Instead, as advised by Carr (2005), the atmospheric and aerosol models particularly applicable to the specific time and date were selected. The atmospheric and aerosol models used in this study are discussed below.

3.2.1.2.1 Atmospheric model

Hong Kong's weather is both tropical and mid-latitude (Ginn *et al.*, 2004). As in any tropical weather system, cyclones and troughs of low pressure are common in summer. Likewise, winters cold surges are frequent, as in mid - latitude regions.

Therefore, predefined atmospheric models were selected in this study according to season. The atmospheric models suitable for the summer and winter seasons of Hong Kong were identified as tropical and mid-latitude winter respectively. The Ozonesonde data measured at Kings Park, by the Hong Kong Observatory was used as input for the user-defined atmospheric model. In Hong Kong, Ozonesonde measurements are not carried out daily, so the closest observation was utilized in case no measurement was available on the image date. It is assumed that the atmosphere during image acquisition was similar to the corresponding Ozonesonde measurement. Weather condition on the two occasions were compared using daily weather extracts obtained from the Hong Kong Observatory website, and the closest Ozonesonde measurements for weather conditions similar to those prevailing on the image dates used.

The inputs used in defining the atmospheric conditions in a user-defined model include altitude (km), pressure (mb), temperature (K), water vapour density (gm^{-3}), and ozone density (gm^{-3}). The water vapour density and ozone density calculated from ozone partial pressure and relative humidity respectively, while, altitude, pressure and temperature were directly retrieved.

The ozone density (ρ_{oz}) is calculated using the following formula.

$$\rho_{oz} = (\text{ozone partial pressure / pressure}) \times 577.3 \times (\text{pressure / temperature}) \quad (3.4)$$

Data on ozone partial pressures (mPa), pressures (hPa) and temperatures (^{o}C) as measured at different altitudes are inserted into Equation (3.4). The estimated values are then divided by 10^{-6} to convert from $\mu g\ m^{-3}$ to $g\ m^{-3}$.

Water vapour densities at different altitudes are calculated by:

Step 1: Calculate the absolute humidity from relative humidity and temperature.

Step 2: Estimate the dew point temperature from the absolute humidity.

Step 3: Find the water vapour pressure from the dew point temperature.

Well known, standard formulas (NASA Technical Reports Server, 2014) were used in the above steps.

3.2.1.2.2 Aerosol model

In this study, two aerosol models are used. One is a predefined model while the other is a user-defined one. Based on the conditions typically used with respect to the aerosol model reported by MODTRAN, one of the existing Aerosol models, i.e., the Urban model in 6S is identified as being suitable for Hong Kong.

The user defined aerosol conditions are determined from a local AERONET (Aerosol Robotic Network) sun-photometer. The input parameters so extracted are aerosol radius (radians), REFR (nm) and REFI (nm) which are the real and imaginary parts of the refractive indices, and dV(*r*)/dln(*r*) which is the volumetric ratio at the given wavelength. Further details concerning data entry in 6SV1.1 are available in 6S User Guide Version 3 (Vermote *et al.*, 2006).

Other necessary input parameters such as the geometric and spectral conditions, the target altitude, surface details, and sensor details may be taken from the header file attached to the AST_L1B product. Figure 3.1 shows the steps used during the atmospheric correction of AST_L1B images.

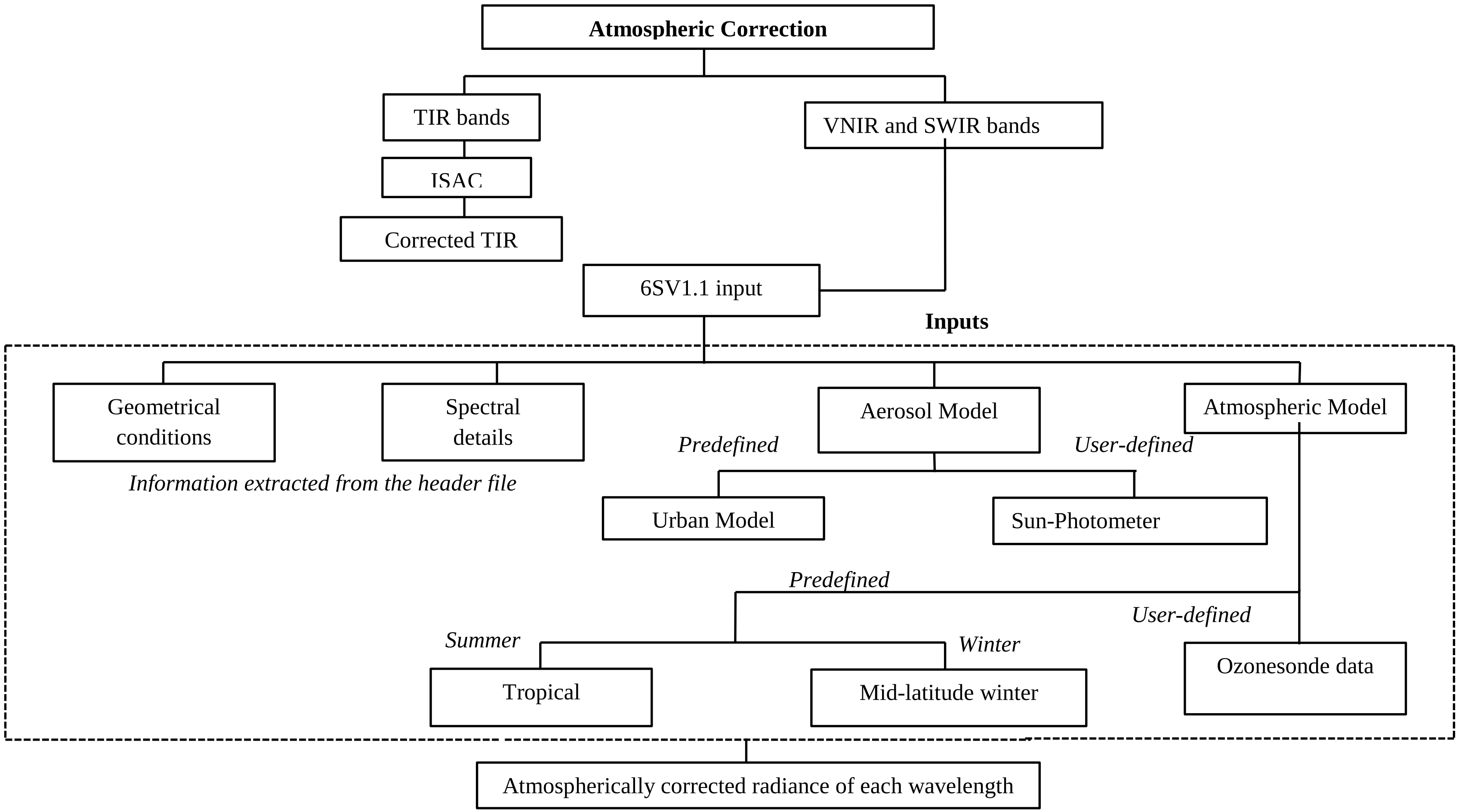

Figure 3.1 Steps used during the atmospheric correction of ASTER Level 1B images.

Note: The essence of the procedure is discussed in section 3.2.1.2.

3.2.1.3 Recalibrating ASTER Thermal Infrared Images

ASTER thermal infrared radiance (TIR) products include information on radiometric calibration errors caused by delays while updating the radiometric calibration coefficients (RCC) (Tonooka, 2003). As in Sakumas (2005), images processed after 8th February 2006 were calibrated using version 3.x. The RCC values (Tonooka, 2003) were inserted into Equation 3.5 to calculate RCC corrected radiance values.

New radiance ($\boldsymbol{L_\lambda}$) = A × Original radiance + B (W/m^2/Sr/μm) (3.5)

where *A* and *B* are the RCC values that depend on the day since launch. As an example, Table 3.3 shows the value of *A* and *B* for 1st January 2013 (day since launch: 4,763); RCC version 3.12.

Table 3.3 RCC values of TIR bands for images acquired on 1st January 2013.

Band	**A**	**B**	**Estimated Changes (Upper: Radiance, Lower: Temperature)**			
			@270K	**@300K**	**@320K**	**@340K**
10	1.001130	-	-0.000	+0.005	+0.010	+0.015
		0.0056	-0.00K	+0.030	+0.040	+0.050
11	1.002528	-	+0.000	+0.011	+0.021	+0.034
		0.0132	+0.00K	+0.060	+0.100	+0.120
12	1.001798	-	+0.000	+0.008	+0.015	+0.023
		0.0099	+0.00K	+0.040	+0.070	+0.090
13	1.001432	-	+0.000	+0.006	+0.010	+0.016
		0.0084	+0.00K	+0.040	+0.060	+0.080
14	1.000889	-	+0.000	+0.003	+0.006	+0.009
		0.0052	+0.00K	+0.020	+0.040	+0.050

Source: ASTER user manual Ver. 2

3.2.2 Land surface temperature (LST) estimation

The process of estimating land surface temperature (LST) using TIR images involves two steps: a) converting spectral radiance to at-sensor Brightness Temperature (BT) and b) correcting for surface emissivity. Band 13 (10.25 to 10.95 μm) among the five TIR bands (Band 10 to 14) is used to compute LST because the spectral width of band 13 is close to the peak radiation of the blackbody spectrum emitted by urban surfaces (Lu and Weng, 2006; Weng *et al.,* 2008).

The steps for deriving LST are:

a) The thermal band (Band-13) is converted from at-sensor spectral radiance to at-sensor BT, assuming that the Earth's surface is a black body (i.e., spectral emissivity equals 1) and atmospheric effects (absorption and emission along the path) have been taken into account (Chander *et al.*, 2009). The conversion formula for estimating at-sensor BT from at-sensor spectral radiance is:

$$\boldsymbol{B^T} = \frac{\boldsymbol{K_{A2}}}{\mathbf{ln}(\frac{\boldsymbol{K_{A1}}}{\boldsymbol{L_\lambda}} + \mathbf{1})} \tag{3.6}$$

where B^T is at-sensor Brightness Temperature (K), L_λ is RCC corrected at-sensor radiance, and K_{A1} (866, W/ m^2 sr µm) and K_{A2} (1350.069147, K) are the prelaunch calibration constants of ASTER TIR bands.

b) Since the measured LST values are referenced to a black body, it is necessary to correct for spectral emissivity with respect to the thermal properties of the urban surface material in question. The emissivity corrected LST (T_{ec}) are calculated using the following equation (Artis and Carnahan, 1982; Weng *et.al.*, 2008)

$$\boldsymbol{T}_{\mathbf{ec}} = \frac{\boldsymbol{B^T}}{\mathbf{1}+(\ \boldsymbol{\lambda} * \boldsymbol{B^T}/\boldsymbol{\rho})\mathbf{ln}\boldsymbol{\varepsilon_s}} \tag{3.7}$$

where, λ is the peak response wavelength of emitted radiance (The peak response wavelength of ASTER Band 13 (10.657 µm) may be taken from the ASTER user handbook), *BT* is the at-sensor brightness temperature calculated using Equation 3.6, and the flux density (ρ) = [h × (C /σ)] = 1.438× 10^{-2} m K, where, h is Planck's constant (6.626 ×10^{-34} J s), *C* is the velocity of light (2.998 ×10^{8} m s^{-1}), σ is Boltzmann constant (1.38 × 10^{-23} J K^{-1}), and ε_s is the surface emissivity estimated from the method described in Section 3.2.3

3.2.3 Surface emissivity estimation

In this study, surface emissivity values are derived directly from the AST_ L1B images. This differs from previous studies in Hong Kong most of which used a simplified method for adopting typical emissivity values of urban materials (Nichol, 2009). The standard product of ASTER's land surface emissivity (AST_05) is derived using the Temperature Emissivity Separation (TES) method (Gillespie *et al.*, 1998). The TES algorithm estimates emissivity at 90 m spatial resolution, which may not be suitable for the typical morphometric conditions of Hong Kong. Therefore, a new simplified method (reflectance method) for emissivity correction was developed in this study while estimating emissivity values at a spatial resolution of 30 m from the radiance values of the SWIR image. The next subsection compares the emissivity values estimated from the three methods and identify the most suitable. Among the three methods, TES algorithm is commonly used in recent studies and reference channel is the oldest technique. The reflectance method developed in the study, works better than the other two methods while estimating temperatures. The reflectance method estimates temperature at higher spatial resolution of 30 m when compared to the 90 m spatial resolution of TES and reference channel methods.

3.2.3.1 TES algorithm

The TES algorithm of Gillespie *et al.* (1998) normalizes the emissivity spectrum which devised for sensors with thermal band such as ASTER using the average emissivity for each pixel. The min-max difference (MMD) of the normalized spectrum is first calculated and used for estimating the minimum emissivity by means of a regression analysis relating the MMD and the minimum emissivity (ASTER higher-level product guide). The normalized emissivity values are scaled using the minimum emissivity value and compensated for reflected skylight by applying the procedure described in the algorithm along with the theoretical documents available at http://eospso.gsfc.nasa.gov/atbd/astertables.html.

3.2.3.2 Reference Channel method

This method (Kahle *et al.*, 1980) is used to calculate the emissivity and temperature values from thermal infrared radiance data. The reference channel emissivity technique assumes that all emissivity values are the same for all the pixels in one channel (band) of the thermal infrared data. Using this constant value, a temperature image is calculated. The results are used to calculate the emissivity values in all other bands using the Planck function.

3.2.3.3 Emissivity retrieval using reflectance (Reflectance method)

In this method, surface emissivity values are derived from the reflectance values of the ASTER SWIR band. Band - 5 (2.145 to 2.185 µm) is selected among other SWIR bands, due to the smaller atmospheric interference at the SWIR region (ASTER higher-level product guide). Hence, the radiance measured at this wavelength is taken as the representative value of surface radiance provided one does not attempt to minimize the impacts from the atmosphere. According to Kirchhoff's law of thermal radiation, $R = 1 - \varepsilon$, the emissivity of an object is equal to its observance at the same temperature (Nicodomus, 1995). Since the emissivity values of objects on the earth cannot exceed one (the maximum emissivity for a blackbody), the reflectance, R, is calculated by subtracting the dimensionless emissive power from 1, i.e., $\varepsilon = 1 - R$.

3.2.4 Albedo

In the study, the albedo values of surface materials over the study area were estimated from Equation 3.8 (Liang, 2001). Spectral radiance estimates of VNIR and SWIR bands were used, and the atmospheric effects removed using the 6S atmospheric correction algorithm.

$$\boldsymbol{\alpha_\lambda = \frac{\pi L_\lambda d^2}{E_{sun,\lambda}\cos\theta}} \tag{3.8}$$

where, α_λ is the planetary albedo, L_λ is the spectral radiance measured at the sensor, d is the distance between the earth and the sun in astronomical units on the day of the image as calculated using landsathandbook.gsfc.nasa.gov/excel_docs/d.xls. The solar zenith angle, θ, equals 90^o minus the solar elevation angle (the angle can be found in the ASTER header file). λ is the wavelength corresponding to the band used and

E_{sun}. The mean solar exoatmospheric radiance of each band are obtained from the ASTER user manual. The ERDAS Model maker does not allow entering of degree values directly. Therefore, the solar elevation angles need to be converted to radians by multiplying by $\pi/180$.

The narrow band albedo values so estimated for each band are converted into broadband albedos using Equation 3.9 as suggested by Liang, 2001. The equation has been used extensively during radio transfer simulations for calculating total shortwave albedo, total-, direct-, diffuse-visible, and near-infrared broadband albedos for several narrowband sensors including ASTER, AVHRR, ETM+/TM, GOES, MODIS, MISR, POLDER, and VEGETATION.

In this study, six bands of AST_L1B data used to retrieve shortwave broadband albedos from the narrow band albedos using the following regression equation:

$$\alpha_{sw} = 0.48\alpha_1 + 0.335\alpha_3 - 0.324\alpha_5 + 0.551\alpha_6 + 0.305\alpha_8 - 0.367\alpha_9 - 0.0015 \quad (3.9)$$

where, α_{sw} is the shortwave albedo; $\alpha_{1}, \alpha_{3}, \alpha_{5}, \alpha_{6}, \alpha_8$ and α_9 are the albedo of respective ASTER bands (band number subscripted).

3.2.5 Net radiation

The total net heat flux is the balance between incoming solar radiation and outgoing reflected solar radiation. The relationship is applicable on a clear sky day. The total net heat flux (R_{HF}) is calculated based on the equation 3.10 given by Xu *et al.*(2008).

$$R_{HF} = K_w\downarrow - K_w\uparrow + L_w\downarrow - L_w\uparrow = K_w^* + L_w\downarrow - L_w\uparrow \quad (3.10)$$

where $\downarrow$ and $\uparrow$ symbolizes downward and up components of radiation and K_w* refers to the portion of total short-wave radiation, given by:

$$K_w^* = (\alpha_{swb} - 1)\, K_w\downarrow \quad (3.11)$$

where α_{swb} is the shortwave broadband albedo (Liang, 2001), and $K_w\downarrow$ is extracted from the HKO's daily meteorology data. The incoming longwave radiation ($L_w\downarrow$) is calculated from the Stefan-Boltzmann law, as

$$L_w\downarrow = \varepsilon_{air}\,\sigma\,(T_a)^4 \quad (3.12)$$

where σ is Stephen-Boltzmann constant [5.67×10^{-8}, ($W \cdot m^{-2} \cdot K^{-4}$)], T_{air} is the air temperature measured from ASTER TIR images using (Nichol and Wong, 2008), and ε_{air} is the atmospheric emissivity calculated from

$$\varepsilon_{air} = 1.24 * (e_{a.} / T_a)^{1/7} \quad (3.13)$$

where, e_a is the atmospheric water vapour pressure calculated using the method given in Prata (1995), and T_a is the air temperature measured by the Hong Kong observatory. Here, a single value for air temperature is used by assuming similar atmospheric water vapour pressures over the study area.

The outgoing longwave radiation ($L_w\uparrow$) is calculated using

$$L_w\uparrow = \varepsilon_s \sigma\,(T_s)^4 \quad (3.14)$$

where ε_s is the surface emissivity estimated, σ is the Stephen-Boltzmann constant, and T_s is the surface temperature measured.

The processes involved in the estimation of net radiation are given in Figure 3.2.

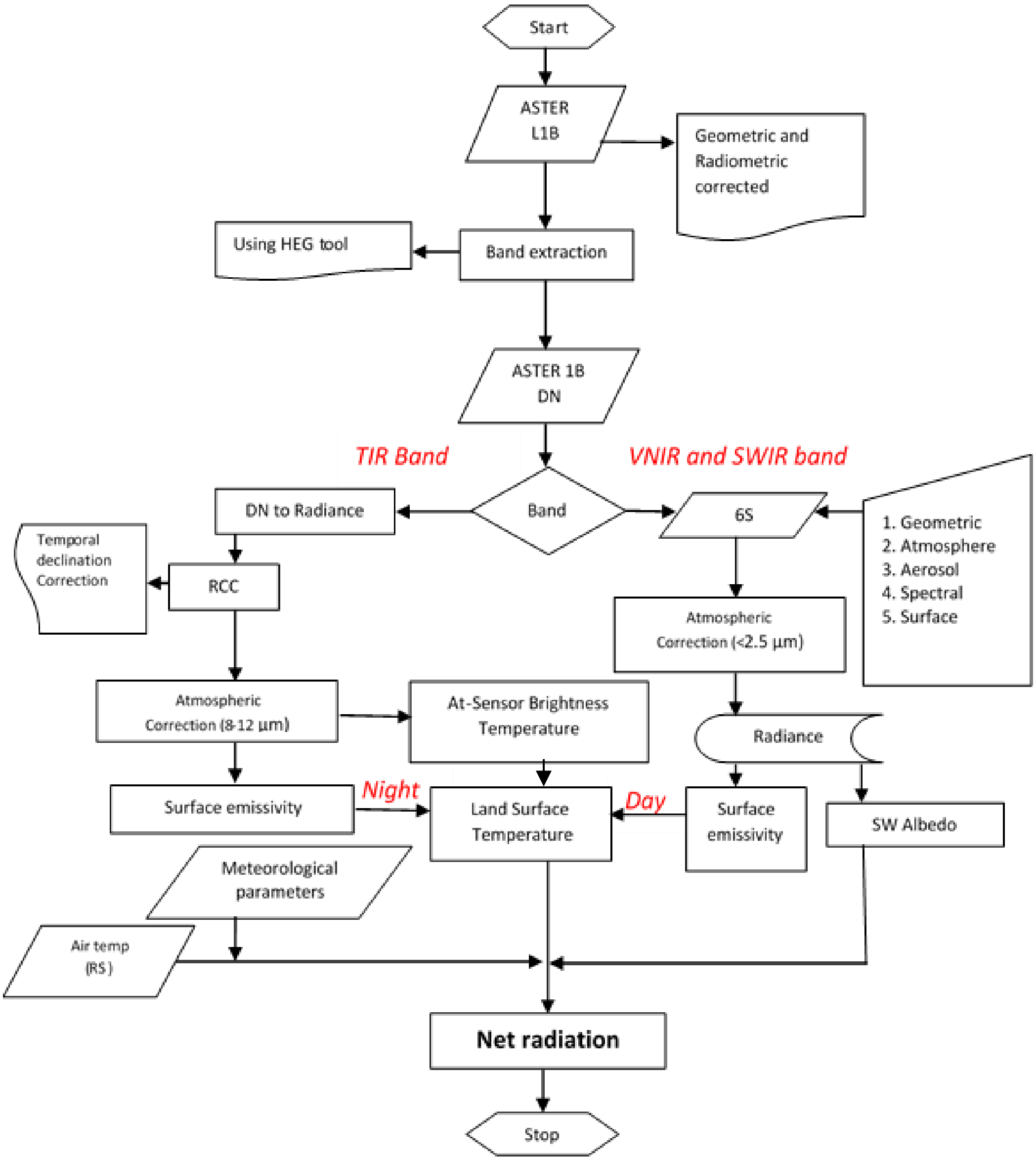

Figure 3.2 Estimation of net radiation using remote sensing (ASTER L1B)

Note: Surface emissivity calculation method depends on the time of image acquisition.

3.2.6 Sensible heat flux

In this study, the sensible heat flux, *H*, is estimated using the aerodynamic resistance method (Allen *et al.,* 1998; Brutsaert, 1982; Voogt and Grimmond, 2000; and Xu *et al.* 2008) given by the following simple relationship:

$$H = \rho\, C_{\mathrm{p}} \frac{T_{\mathrm{s}} - T_{\mathrm{a}}}{r_{\mathrm{a}}} \quad (3.15)$$

where T_s and T_a are the surface and air temperatures estimated from AST_L1B respectively, ρ is the density of air (kg m^{-3}), C_p the specific heat of air at constant pressure, and r_a Is the aerodynamic resistance (s m^{-1}). Air density (ρ) is calculated based on: (atmospheric pressure ×100) / (R_{sp}×T_a); where R_{sp} is the specific gas constant for dry air (287.058 J/(kg·K)). Aerodynamic resistance (r_a) is calculated using Verma (1998)

$$r_a = \frac{1}{ku*} [\ln\left(\frac{Z - Z_d}{Z_{om}}\right) + \ln\left(\frac{Z_{om}}{Z_{oh}}\right) - \Psi_h \left(\frac{Z - Z_d}{L}\right)] \quad (3.16)$$

Moreover, the friction velocity, u^*, is given by the stability corrected log-law

$$u^* = U\mathrm{k}\left[\ln\left(\frac{Z - Z_{\mathrm{d}}}{Z_{0\mathrm{m}}}\right) + \Psi_{\mathrm{m}}\left(\frac{Z - Z_{\mathrm{d}}}{L}\right) - \Psi_m\left(\frac{Z_{0\mathrm{m}}}{L}\right)\right] \quad (3.17)$$

where, *U* is the wind speed measured at height, *z* (m), z_d is the zero plane displacement height (m), $z_{0\mathrm{m}}$ is the roughness length (m) for momentum, and z_{0h} is the roughness length (m) for heat. Ψ_{h} and Ψ_{m} are stability correction functions for heat and momentum, which depend on the respective Monin-Obukhov lengths (Brutsaert, 1982), and k is von Karman's constant (0.4).

The excess resistance can be expressed as kB^{-1} (Stewart *et al.,* 1994):

$$kB^{-1} = \ln\left(\frac{Z_{\mathrm{om}}}{Z_{\mathrm{oh}}}\right) \quad (3.18)$$

The study area is divided into grid cells of 100 m, for which roughness parameters are calculated using the procedure given by Macdonald *et al.* (1998) as outlined in

Grimmond and Oke (1999). The height of buildings in a grid cell is taken as the mean building height within the cell. The roughness length is calculated using the method of Macdonald *et al.* (1998) presented as a derivation that starts from fundamental principles and certain simple assumptions:

$$\frac{z_{0\mathrm{m}}}{z_{\mathrm{h}}} = \left(1 - \frac{z_{\mathrm{d}}}{z_{\mathrm{h}}}\right) \exp\left(-\left(\lambda_{\mathrm{FA}}(1 - \frac{z_{\mathrm{d}}}{z_{\mathrm{h}}})0.5\beta\,\frac{C_D}{\mathrm{k}^2}\right)^{-0.5}\right) \qquad (3.19)$$

where $z_{0\mathrm{m}}$ is roughness length, z_{h} and λ_{FA} are the values of mean height of buildings and frontal area density of buildings in a grid cell respectively, and z_{d} is the displacement height. The constants used are: k, the von Karman constant (0.4); C_{D}, the drag coefficient (1.2); and β, an empirical coefficient (β = 1).

The displacement height is calculated as:

$$\frac{z_{\mathrm{d}}}{z_h} = 1 + \alpha^{-\lambda_{\mathrm{PA}}}(\lambda_{\mathrm{pa}} - 1) \qquad (3.20)$$

where the plane area density of obstacles (λ_{pa}) is calculated for grids of 100 m resolution and the empirical coefficient, α, is taken equal to 4.43.

The Monin-Obukhov length (L) and the stability functions, Ψ_m and Ψ_h, for momentum and heat, respectively, *for* the study area are calculated as suggested by Brutsaert (1982) as -50, 1 and 0.19, respectively, .

The roughness length of heat ($z_{0\mathrm{h}}$) is calculated for each grid cell using the method of Brustead (1982)

$$z_{0\mathrm{h}}=z_{0\mathrm{m}}\,[7.4 \exp (-1.29\, Re^{*\,0.25}] \qquad (3.21)$$

where $z_{0\mathrm{m}}$ is the roughness length of momentum (equation 19), and $Re^{*} = z_{0\mathrm{m}}\, u^{*}/v$ is the roughness Reynolds' number with a kinematic molecular viscosity, v, equal to 1.461×10^{-5} m s^{-1}.

3.2.7 Latent heat flux

Latent heat flux, Q_{lh}, is calculated using the following equation (Kato and Yamaguchi, 2005).

$$Q_{\text{lh}} = \left[\left(\frac{\rho\, C_p}{\gamma}\right)\left(\frac{e_{\text{s}}^{*} - e_{\text{a}}}{r_{\text{a}}+r_{\text{s}}}\right)\right] \tag{3.22}$$

where e_{s}^{*}, the saturation vapour pressure in hPa at the surface temperature is estimated using the TIR image, γ is the psychometric constant in hPa K^{-1} at the appropriate temperature and r_{s} is the stomatal resistance in s/m.

The magnitudes of the psychometric constants, γ, are estimated from the temperature dependent thermodynamic properties given in Oke (1991).

3.2.8 Ground heat flux

The surface temperature at a given location is dependent on surface energy balance. The ground heat flux is estimated as a fraction of the net radiation (Clothier *et al.* 1986). Based on this theory, several investigators have attempted to define the ground heat flux as a function of net radiation and reflectivity in the red and NIR bands (Reginato *et al.*, 1985; Clothier *et al.*, 1986; Jackson *et al.*, 1987; Kustas and Daughtry, 1990; Quattrocchi, 2004). Because of the strong relationship between soil heat flux, net radiation and vegetation cover, the basis of reflectivity in the near-infrared wavebands are determined from the regression relationship given in Malek *et al.* (1997).

$$G_{\text{sf}} = [0.774 - 0.324\ (\rho\ \text{NIR}/\rho_{\text{Red}}))]\ R_{\text{HF}} \tag{3.23}$$

where ρ is the reflectance of ASTER NIR band (Band 3) and red band (Band 2).

Several studies have calculated ground heat as a fraction of net radiation, in which surface cover fractions are equivalent to the land-use class. This study followed a simple method where the vegetational cover fractions are calculated for the visible and near infrared bands of the images. For night time images, the closest surface cover fraction estimated from the previous daytime images are used assuming that the cover does not change during the intermediate period.

3.3 Results and Discussion

3.3.1 Surface emissivity

Temperature determined for the daytime image of 30th November 2007 using different emissivity techniques was compared with the temperatures measured on the field using thermocouple data loggers. Figure 3.3 shows the difference between satellite measured surface temperature and those measured using thermocouple data loggers. It is observed that the estimates from the reflectance method are much closer to the field measurements than the TES and reference channel methods. The temperature difference values range from 0.2 to 2.3 ^{o}C, 0.15 to 5.6 ^{o}C, and 2.6 to 8.6 ^{o}C for the reflectance method, normalization method and reference channel method, respectively. The new reflectance emissivity techniques i.e. reflectance method exhibits the least deviation from the field measured temperature values. While considering the accuracy of data logger (1 ^{o}C) the reflectance method enables one to map surface temperature better than other two methods. In the present study, the temperatures measured at 10 locations are used as reference values in a manner including homogenous (at least 90 m × 90 m) concrete and grassy surfaces. The measurement period was ± 15 minutes to the satellite overpass time. The details of measurement location is given in Table 3.4. The new reflectance emissivity method works well over concrete and grassy surfaces.

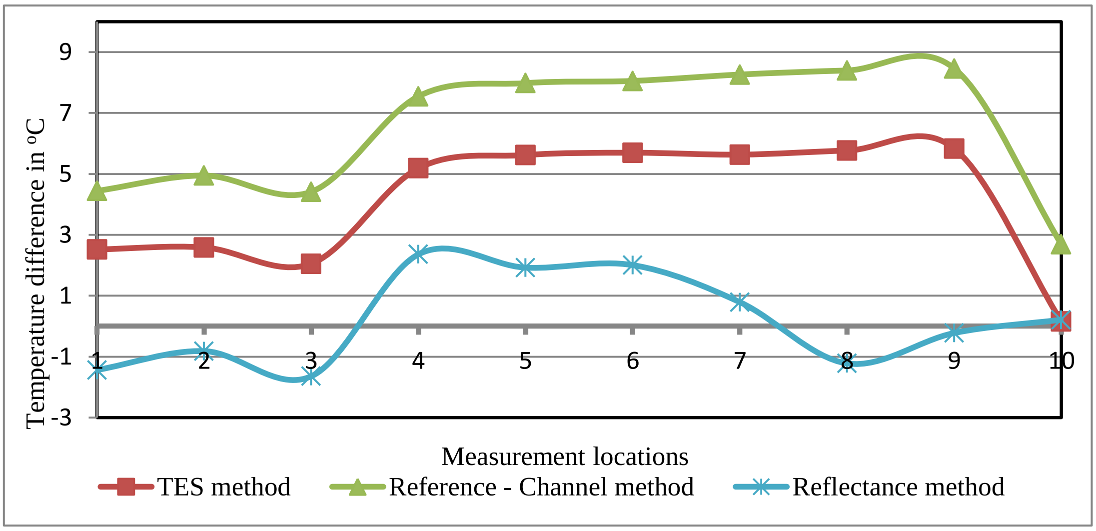

Figure 3.3 Temperatures measured using three different emissivity techniques. The measurement was carried out at different surfaces during the image overpass time.

Table 3.4 Difference between Satellite measured (Applied different emissivity technique) and field measured temperature and the detail of measurement locations.

Time	**Latitude**	**Longitude**	**Land cover**	**Deviation of satellite measured surface temperature from the ground measurement (° C)**		
				Reflectance method	**TES method**	**Reference channel method**
10:45	22.3274	114.1740	concrete - basketball	1.4	2.5	4.4
10:48	22.3274	114.1742	concrete - basketball	0.8	2.6	4.9
10:52	22.3273	114.1743	concrete - basketball	1.6	2.1	4.4
11:00	22.3279	114.1743	concrete - football	2.3	5.2	7.5
11:02	22.3278	114.1744	concrete - football	1.9	5.6	7.9
11:04	22.3279	114.1745	concrete - football	2.0	5.7	8.0
11:10	22.3284	114.1745	concrete - football	0.8	5.6	8.2
11:13	22.3284	114.1747	concrete - football	1.2	5.8	8.3
11:16	22.3283	114.1748	Grass	0.2	5.8	8.4
10:49	22.0314	114.2063	Grass	0.2	0.2	2.6

3.3.2 Albedo

Surface albedo values are difficult to validate. However, the study used the net radiation value measured by Fung *et al.* (2009) as a reference to validate albedos measured over a rural concrete surface at Ta Kwu Ling, located at 22° 31′ 43″ N Latitude and 114° 09′ 24″ E Longitude. This is the site of one of the oldest weather station in Hong Kong. It is 24 km north of Kowloon and 15 m above mean sea level. Since it is on flat land surrounded by hills, urban and maritime influences are negligible (Fung *et al.*, 2009). The net radiometer is mounted 1.8 m above the ground so that the circumference of the coverage is 18 m over the concrete surface of an area of 20 m × 20 m (Fung *et al.*, 2009). The net radiometer (CNR 1 from Kipp & Zonen) has two Pyranometers operating from 0.3 to 3 m wavelengths of solar radiation and two Pyrgeometers (5 to 42 m wavelengths of infrared radiation), with one pointing up and one down.

Three separate shortwave broadband albedo (α_{swb}) values (Table 3.5) were calculated using the method suggested by Liang *et al.* (2000). They are: a) TOA albedo (for albedo calculation radiance value without atmospheric correction were used), b) Albedo using the 6S user defined model (for albedo calculation AST ER bands were atmospherically corrected using 6S user defined model), and c) Albedo using the 6S predefined model (for albedo calculation ASTER bands were atmospherically corrected using 6S predefined model). The corresponding albedo values (α_{swb} in Table 3.5) are 0.187 (TOA), 0.146 (6S-user defined), and 0.42(6S-Predefined). The albedo value estimated using remote sensing methods at the location are compared with the albedo value of 0.16 measured using the net radiometer at the same time. The albedo estimated from the user-defined model is much closer to the field measured value (Table 3.5). The percentages of deviation are 2.8, 1.3 and 26 for albedo estimated using TOA, 6S user defined, and 6S predefined models respectively.

The results suggest that the atmospheric and aerosol conditions described using local measurements in the atmospheric correction (Ozonesonde and Sun-Photometer) represent the surface characteristics better than bands used without atmospheric correction and bands corrected using predefined models. The result are given in Table 3.5.

Table 3.5 Net radiation values estimated using different albedo and emissivity values

Trial*	ε_s	α_{swb}	T_s (^{0}C)	T_a (^{0}C)	R_{HF} (W m^{-2})	$R_{HF} - R_F$ (W m^{-2})	$R_{HF} - R_F$ (%)	$\alpha_{swb} - \alpha_F$ (%)
1	0.866	0.187	29.305	23.514	504.811	87.811	17	2.8
2	0.866	0.146	29.305	23.514	488.207	71.207	15	1.3
3	0.866	0.420	29.305	23.514	259.056	-157.944	61	26
4	0.960	0.187	24.280	23.514	499.850	82.850	17	2.8
5	0.960	0.146	24.280	23.514	483.240	66.240	14	1.3
6	0.960	0.420	24.280	23.514	254.980	-162.020	64	26
7	0.993	0.187	22.390	23.514	498.099	81.099	16	2.8
8	0.993	0.146	22.392	23.514	481.490	64.490	13	1.3
9	0.993	0.420	22.392	23.514	252.344	-164.656	65	26

*Refer table 3.6 for combinations of emissivity and albedo used in each trial.

Where, surface emissivity (ε_s) (estimated using reflectance, TES, and Reference channel methods), shortwave broadband albedo (α_{swb}) (estimated using TOA, 6S-user defined and 6S-predefined models), surface temperature (T_s) (estimated using three different emissivity techniques), Air temperature (T_a) and net radiation (R_{HF}) were measured from the satellite image. R_F is the field measured net radiation (417 W m^{-2}), and α_F is the albedo measured using net radiometer at 11 a.m. that is close to the satellite overpass time (11.04 a.m.) on 30th November 2007. The net radiation estimated using remote sensing depends greatly on the albedo of the surface material. Therefore, the closest satellite measured net radiation to the field measured net radiation can be used to identify a better method of estimating shortwave broadband albedo.

For trial 2, 5, and 8, the net radiations exhibit minimum deviations (71.20, 66.24, and 64.49 W m^{-2}, respectively) from the corresponding field measured values. The net radiation deviation ranges between 13 and 15 percent for albedo values computed from user-defined models, which are much smaller than those obtained from other methods.

The combinations of emissivity and albedo used in net radiation estimation are given below

Table 3.6 Combinations of surface emissivity and shortwave broadband albedo used in Table 3.5

Trial	**Emissivity (ε_s)**	**Albedo (α_{swb})**
1	Reflectance method	TOA Shortwave broadband
2	Reflectance method	Shortwave broadband (6S - User defined model)
3	Reflectance method	Shortwave broadband (6S - Predefined model)
4	TES method	TOA Shortwave broadband
5	TES method	Shortwave broadband (6S - User defined model)
6	TES method	Shortwave broadband (6S - Predefined model)
7	Reference-Channel method	TOA Shortwave broadband
8	Reference-Channel method	Shortwave broadband (6S - User defined model)
9	Reference-Channel method	Shortwave broadband (6S - Predefined model)

3.3.3 Anthropogenic heat and its components over Hong Kong

In this study, the net radiation, sensible heat, ground heat, and latent heat flux values were calculated for 13th September 2008 and used to represent the spatial distribution and intensity during daytime. The cloud free ASTER images of 13th August 2008 and 13th September 2008 are used to represent night and daytime anthropogenic emissions. See Chapter 6 for detailed seasonal analysis.

The net radiation values (Figure 3.4) range between 228 and 551 W m^{-2} with the maximum values found over water surfaces and the minimum ones over open ground and vegetation. This is probably due to the emissivity of water which emits most of the insolation, while building materials absorb part of the incoming radiation, which is released later as sensible heat flux (Figure 3.5).

Larger differences between the surface and air temperatures along with a complex surface morphology over urban regions result in higher sensible heat values being estimated by the aerodynamic resistance method. Since the aerodynamic resistance parameters are calculated using 3D building files, the study focussed on sensible heat over the urban areas. The negative values shown in Figure 3.5 are at pixels for which aerodynamic parameters are not calculated. The intensity of sensible heat is higher over the dense commercial and residential areas (e.g., Sham Shui Po and Mong Kok), while the maximum emission is about 475 W m^{-2}.

The latent heat (Figure 3.6) is calculated based on the aerodynamic properties of urban surfaces. Therefore, this study has focused on urban areas alone. The spatial distribution is almost similar to that of the sensible heat flux, and the maximum latent heat was observed to be 7 W m^{-2}. The increase in sensible and latent heat values over urban areas is probably associated mainly with emissions from air conditioning and traffic.

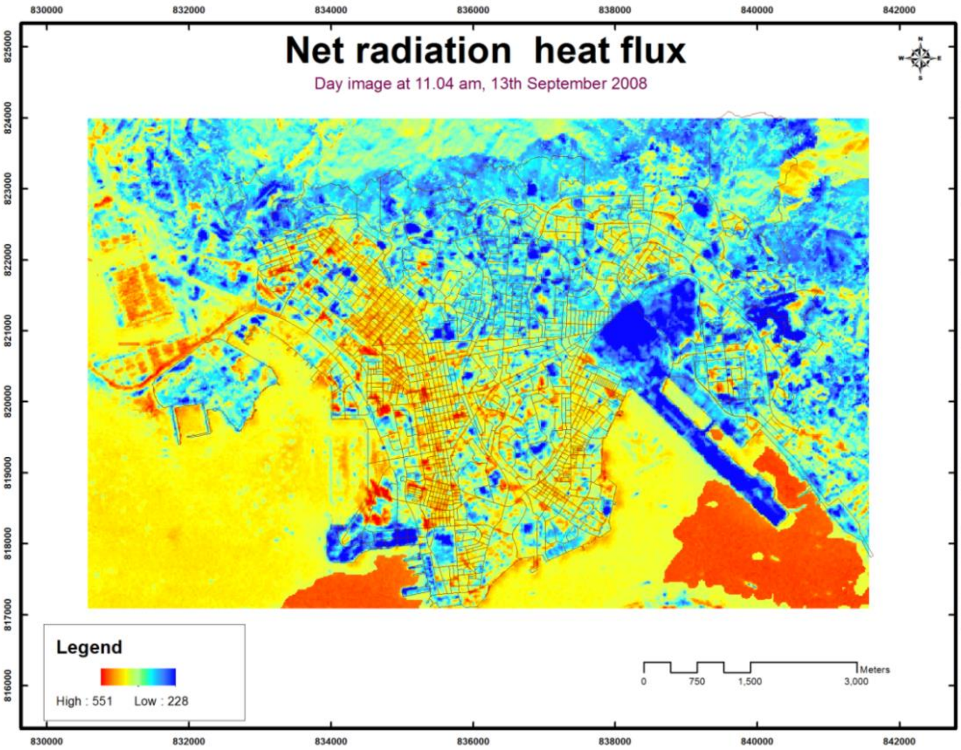

Figure 3.4 Net radiation heat flux for the daytime image of 13th September 2008 at 11.04 am

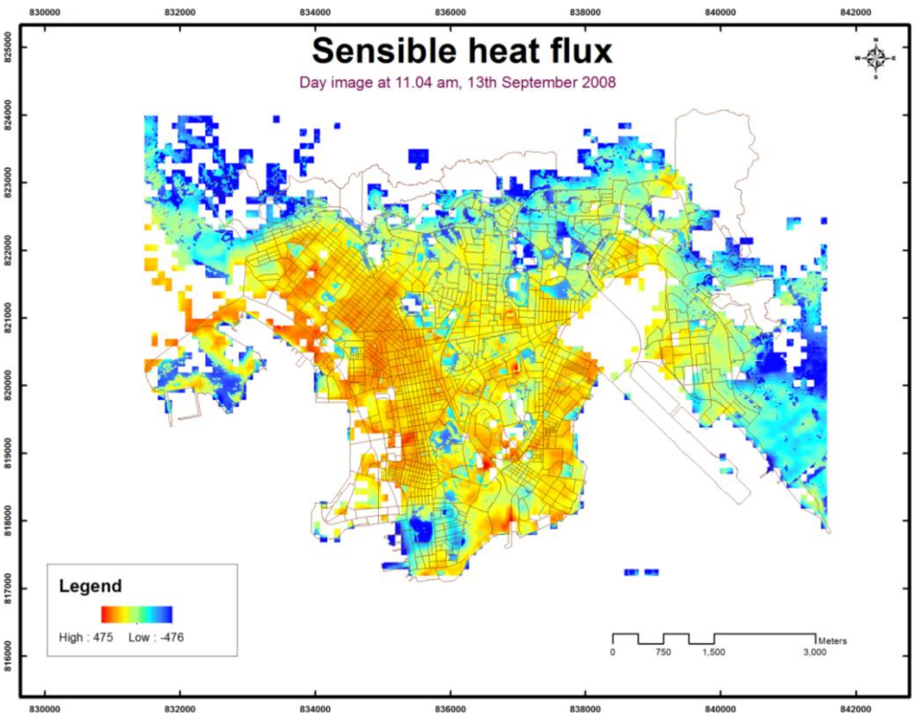

Figure 3.5 Sensible heat flux for the daytime image of 13th September 2008 at 11.04 am.

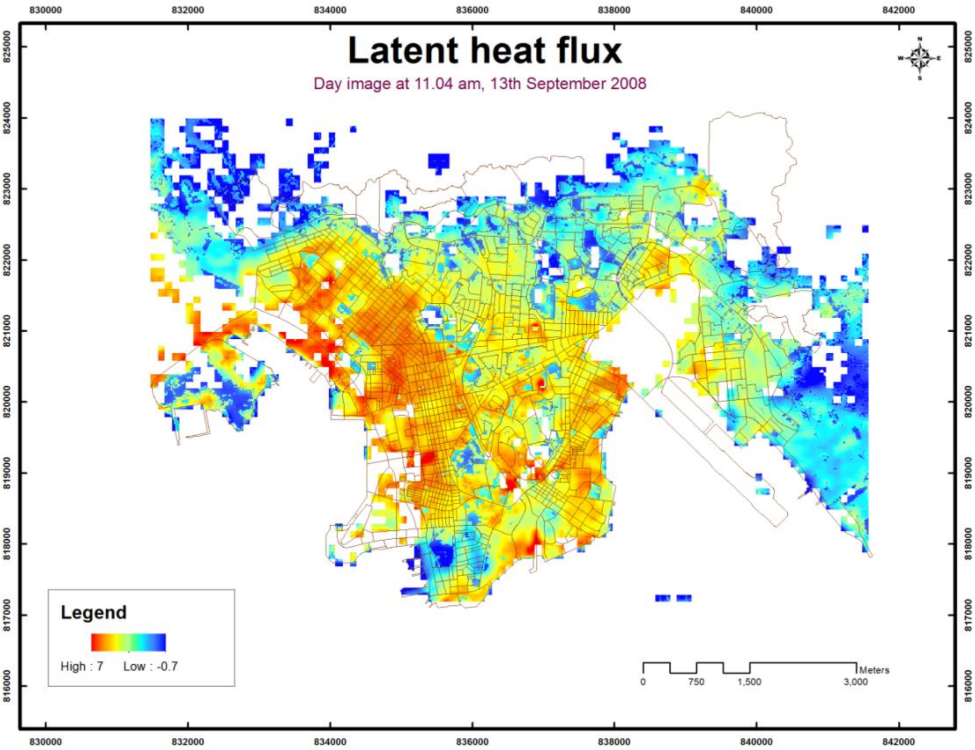

Figure 3.6 Latent heat flux for the daytime image of 13th September 2008 at 11.04 am.

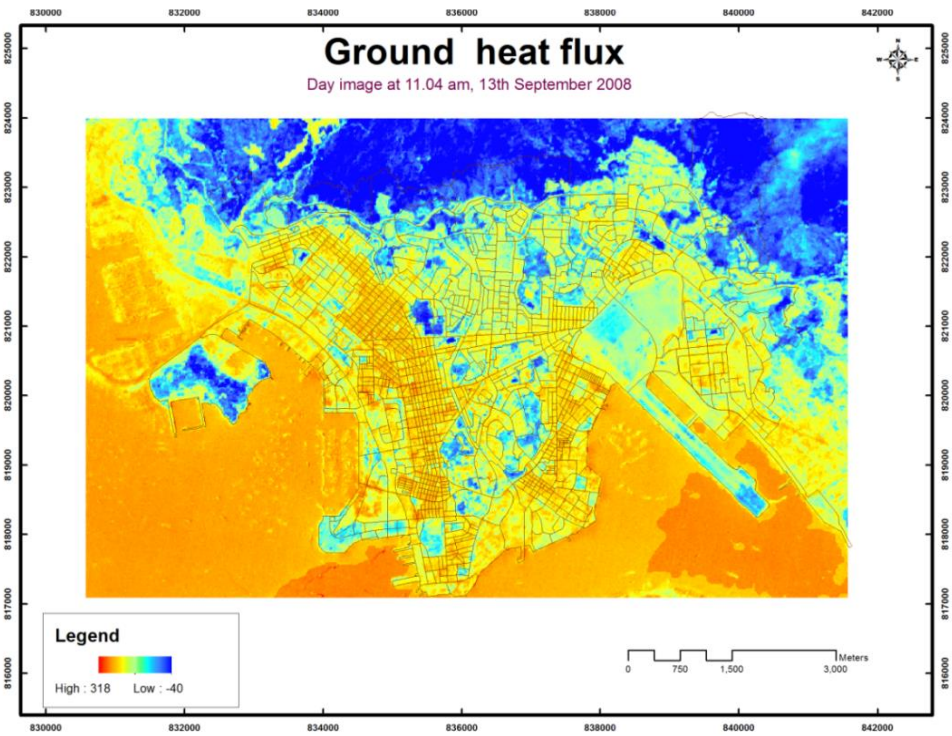

Figure 3.7 Ground heat flux for the daytime image of 13th September 2008 at 11.04 am.

In this study, ground heat (Figure 3.7) value is calculated as a fraction of net radiation values. The maximum ground heat, 318 W m^{-2}, was observed over the water surfaces on the late summer time image when the see is relatively warm. However, only pixels over land areas are considered for anthropogenic heat flux computation.

Anthropogenic heat values estimated over the urban area of Kowloon are shown in Figure 3.8. As expected higher emissions are observed over pixels containing high-rise buildings and roads with higher traffic density. No anthropogenic heat emission is observed over vegetation surfaces.

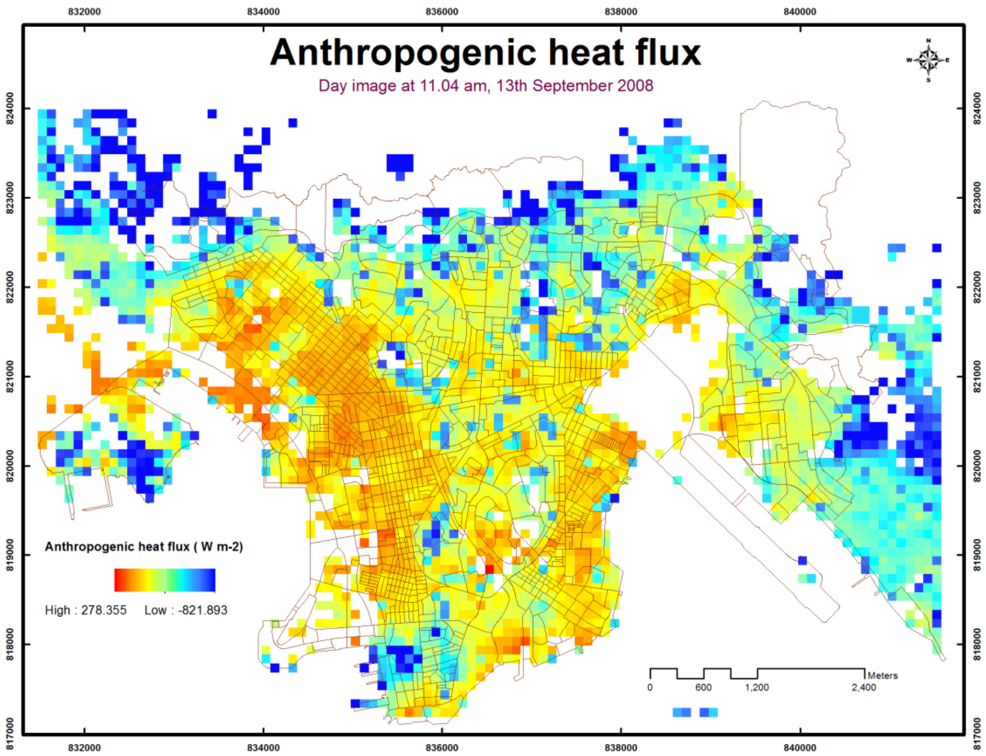

Figure 3.8 Anthropogenic heat flux for the daytime image of 13th September 2008 at 11.04 am.

3.3.4 Diurnal variation of anthropogenic heat emissions

During the day, anthropogenic heat emissions are higher over commercial areas, whereas at night (Figure 3.9) they are higher over residential areas. Which is expected due to commuting patterns. The intensity of anthropogenic emissions is much higher during the day with the maximum equalling 278 W m^{-2}, whereas night-time exhibits lower intensity of 64 Wm^{-2}. Similarly, the mean of anthropogenic heat is higher during daytime at 63 $Wm^{-2,}$ and lower during night-times, at 10.7 W m^{-2}. The mean values are calculated from pixels with emissions, but neglecting pixels with negative values for which morphometric parameters are not calculated. The extremely high use of air conditioners in Hong Kong's commercial areas and huge traffic flows contribute heavily during the day, while night time emissions originate only from buildings and mostly in residential areas.

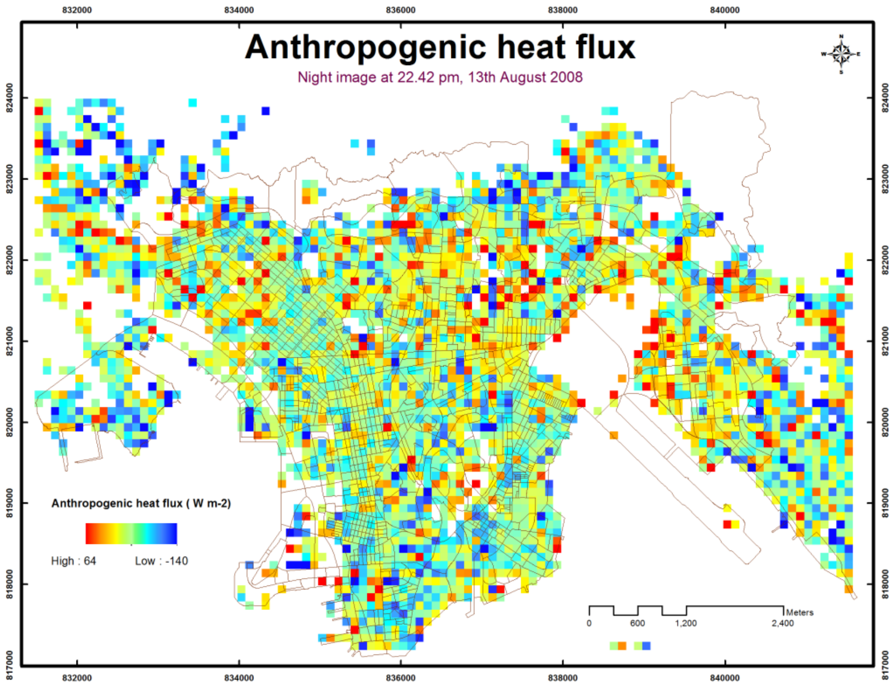

Figure 3.9 Anthropogenic heat flux for the night time image of 13th August 2008 at 10.42 pm.

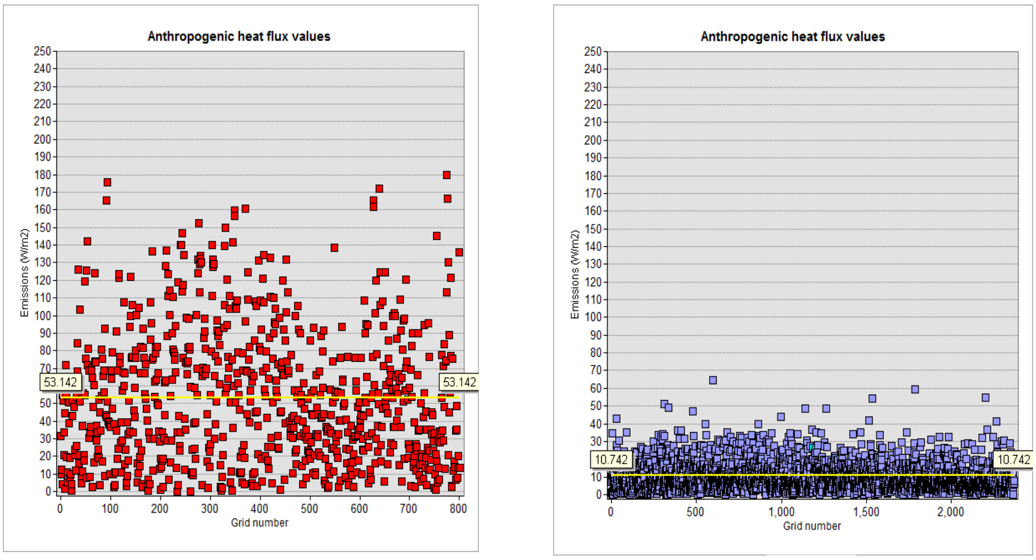

(a) (b)

Figure 3.10 Scatter plots of anthropogenic heat flux values for each pixel as estimated during the daytime (a) and the night-time (b).

Figure 3.10 shows the anthropogenic heat emissions during day as well as night-time. The smaller numbers of pixels (100 m × 100 m) exhibiting positive values of anthropogenic heat emissions during the day than those during night may be due to a lag in sensible heat stored in buildings. However, the intensities are much lower than those during daytime due to reduced anthropogenic activity.

The anthropogenic heat values estimated using remote sensing, for daytime and night-time, as well as for summer and winter seasons, will be compared with and evaluated against anthropogenic heat values estimated using other models in Chapter 6.

Chapter 4

ANTHROPOGENIC HEAT FLUX MODELLING OF HONG KONG USING LUCY

4.1 Introduction

Anthropogenic heat generated in urban areas has been modelled for a number of cities around the world, for example, Tokyo, London, and Manchester. Estimates have been provided over a horizontal grid, sometimes with a vertical third dimension (Allen *et al.,* 2011). The spatial resolution has ranged from 100 m^2 cells (Grimmond, 1992; Pigeon *et al.,* 2007) to 200 m^2 (Smith *et al.,* 2009), to 250 m^2 (Ichinose *et al.,* 1999). Klysik (1996) and Sailor & Lu (2004) estimated emissions of different cell sizes at a local area level, based on land use polygons. Others have focused on individual city blocks, taking into account the building geometries and temperature changes at different altitudes above the ground surface (Kondo and Kikegawa, 2003). Flanner (2009), Makar *et al.* (2006), and Allen *et al.* (2011) estimated anthropogenic emissions worldwide, based on global datasets.

In this study, **L**arge scale **U**rban **C**onsumption of Energ**Y** (LUCY), a global anthropogenic heat model is customized for Hong Kong. The results of LUCY (original version) have been compared with other anthropogenic heat models of London, New York, Tokyo, San Francisco, Vancouver, Manchester, Beijing and Houston (Allen *et al.,* 2011). LUCY considers diurnal and seasonal variations of global anthropogenic heat emissions at a high spatial resolution (Allen *et al.,* 2011). It is possible to improve the spatial accuracy of LUCY if an input population dataset of higher resolution is available. Developments such as spatial averaging and improvement's in the temperature scheme of LUCY (Lindberg *et al.*, 2013) are enabling to use it for finer resolution. LUCY has gone through several versions since its beginning, with significant changes being made in each version, with LUCY v2013a being the most recent. The version of LUCY customized for Hong Kong is named LUCY-HK.

4.2 Methodology

The majority of anthropogenic heat models are based on a simple partition of anthropogenic heat emission sources: metabolic, building and vehicular (Sailor & Lu, 2004; Grimmond, 1992). Some have omitted metabolic heat emission as it is usually small ─ less than 3% of measured anthropogenic heat (Sailor and Lu, 2004). At the other extreme, some studies have focused on building heat emission, which accounts for most of the anthropogenic heat (Hamilton *et al.*, 2009).

LUCY-HK is based on a partition of anthropogenic heat similar to that used by Grimmond (1992) and given in equation 4.1. The algorithm of LUCY-HK is in line with LUCY v2013a, but with a few changes included. The changes are discussed here with reference to the anthropogenic heat components:

$$\boldsymbol{Q_{ahf} = Q_{met} + Q_{veh} + Q_{bui}} \tag{4.1}$$

where, Q_{ahf} is the anthropogenic heat flux, Q_{met}, Q_{veh}, and Q_{bui} are the metabolic, vehicle and building heat components of anthropogenic heat emission, respectively. Humans release metabolic heat, Q_{met}, throughout the day with the amount of emission depending on the metabolic activity of the body. As vehicles travel along roadways, they release heat and moisture resulting from the combustion of fuels, called vehicle heat (Q_{veh}) (Sailor, 2011). Building heat (Q_{bui}) is the waste heat released from buildings as a result of the energy consumed for lighting, heating, ventilation and air conditioning.

In LUCY-HK, Q_{veh} and Q_{bui} are not measured directly from the emission sources; they are appraised based on the population density at each pixel (Allen *et al.*, 2011). The detailed methodology of all the Q_{ahf} components is explained below and the workflow is presented as a flowchart in Figure 4.1.

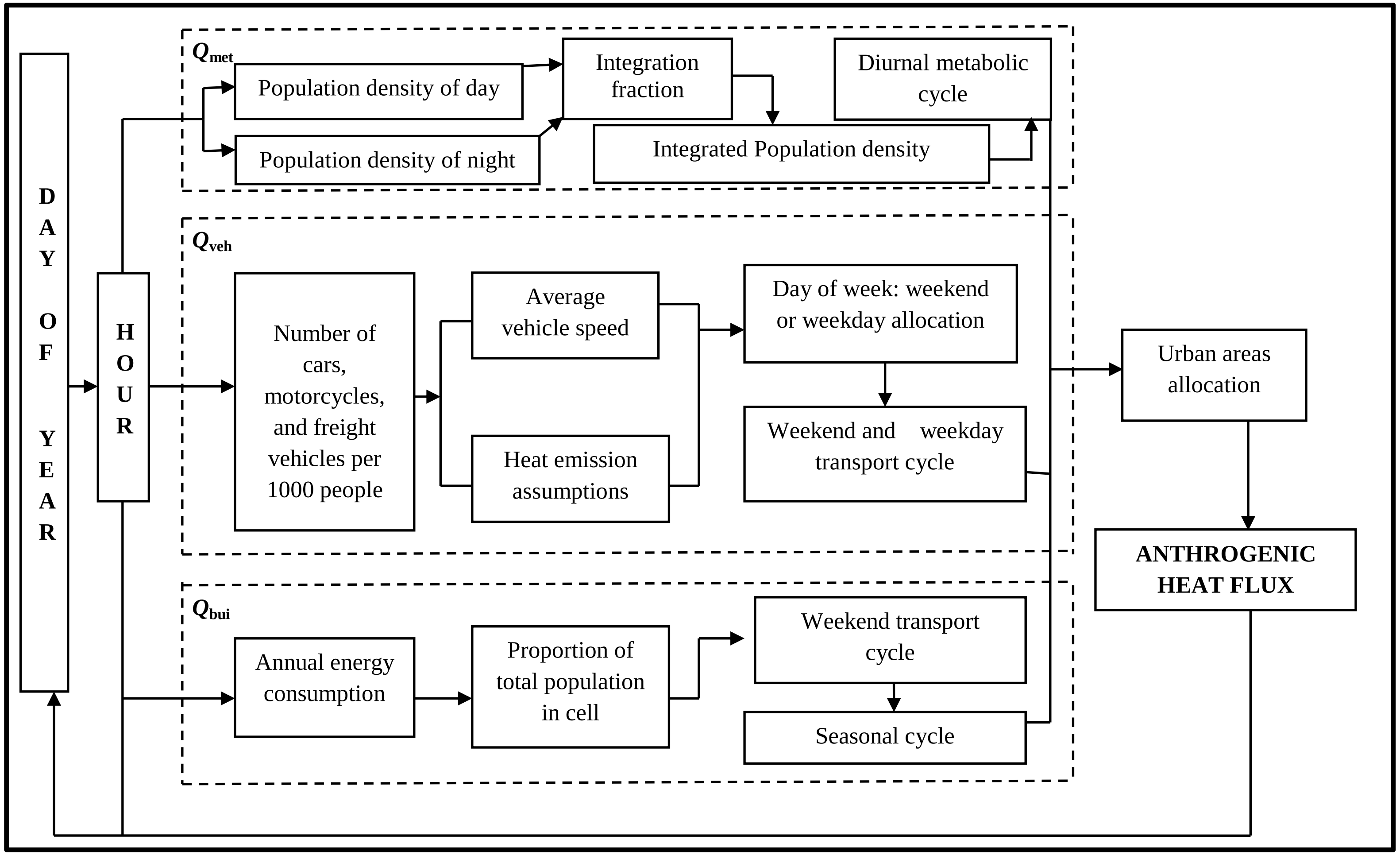

Figure 4.1 Flowchart of LUCY-HK's anthropogenic heat model using a top-down approach.

4.2.1 Metabolic heat

Metabolic heat emission (Q_{met}, Wm^{-2}) is calculated using the following equation

$$Q_{met} = PD(t) * Met_{em}(t) \qquad (4.2)$$

where *PD* is the population density per grid cell (km^2) as a function of hour of the day and Met_{em} is the amount of energy released per person as a function of hour of the day (W). In order to convert Wkm^{-2} into Wm^{-2}, the cell is multiplied by 10^6. In Sailor and Lu (2004), the diurnal pattern of metabolic emission, Met_{em}, is adopted with 75 W (minimum) during sleep, 175 W (maximum) during periods of higher physical activity, and 125 W during periods of moderate physical activity. In this model, the metabolic periods used are 8 am to 10 pm (175 W), 7 am and 11 pm (125 W) and, 12 am to 6 am (75 W). Hong Kong's typical working hours are used to set the active metabolic period (extracted from World Travel Guide, 2013). Figure 4.2, shows the function of metabolic heat emission with respect to time.

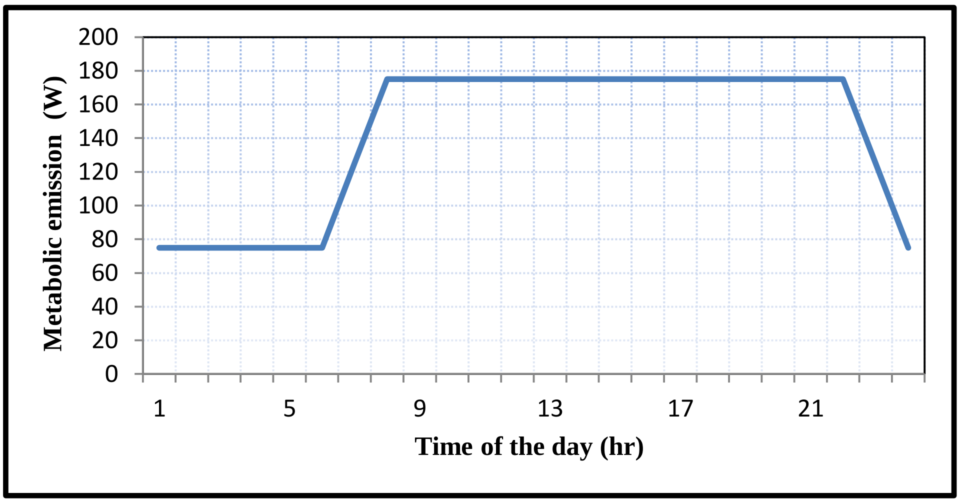

Figure 4.2 Hourly metabolic heat emission (Met_{em}) per person used in LUCY-HK.

In LUCY v2013a, the input population density, *PD*, is a constant (inter cell movement is not incorporated) during the entire diurnal cycle; whereas, LUCY-HK uses integrated population density values (densities of day and night) for the diurnal cycle. Since data on daytime populations are not collected as a part of the census in

Hong Kong, this study calculates them from the geographic characteristics of working population as provided in Census data (Census and Statistics Department of Hong Kong, 2014). The population of Cases (1- 4) (see below) is available at the TPU (Tertiary Planning Unit) level. But, it is not sufficient to estimate daytime populations. Hence, in this study, the land use data obtained from the Land Department of Hong Kong is used to redistribute worker and student populations during the daytime.

Case 1: People working/studying within the same TPU;

Case 2: People working/studying in other TPU but inside the same district;

Case 3: People working/studying in other larger census divisions, namely Hong Kong (HK), Kowloon (KW) and New Territories (NT);

Case 4: Not working.

Population from cases (1) and (2) are summed up to calculate PD_1 (population density of people remains in a same TPU during daytime). People living on vessels and people who do not have permanent places of work are included in Case (1). Persons staying outside Hong Kong for seven days before the Census are considered as workers outside the country, and excluded from the calculation. The workers and students of Case (2) are distributed to other TPU's within the district, and the density is calculated as PD_2. In Case (3), the area of census division is significant, and the exact location of migrated population is not available, therefore it is distributed based on the type of land use.

The number of people working within each larger census division is first aggregated and later transformed, based on the percentage of people working in different land use types (Table 4.1).

Table 4.1 Percentage of people working in different land use classes, extracted from the occupation of people in Hong Kong: Census and Statistics Department of Hong Kong (2013).

Land use type	Percentage of Workers
Residential	22
Commercial/Business	39
Industry	4
Governmet, Institution or Community	35

The area of land use polygons within larger census divisions and the population distributed on it are used to calculate population density (PD_{3a}) of each land use polygon. The student population of the larger census division is distributed among the lands of educational institutions, and then the area of the educational institutions and population distributed are used to calculate PD_{3b}. Finally, PD_{day} is calculated by adding all the daytime densities

$$PD_{day} = PD_1 + PD_2 + PD_{3(a+b)} \tag{4.3}$$

Equation 4.3 is not applicable on public holidays, and weekends, when most people are expected to stay at home or to travel to places that are occasional. The estimated daytime population is vital for LUCY-HK because it depends mostly on the population data. Its sensitivity to population density is shown in Figure 4.9. The time-dependent population density $PD(t)$ is calculated using Equation 4.4

$$PD(t) = PD_{day} * PF + PD_{night} * (1 - PF) \tag{4.4}$$

Where, PD_{day} is the daytime population density, and PD_{night} is the night time population density (density based on unchanged census population). The population fraction (PF) (Table 4.2) is used to integrate population density of day and night. Figure 4.3 represents the integration of two population densities with respect to the time of the day.

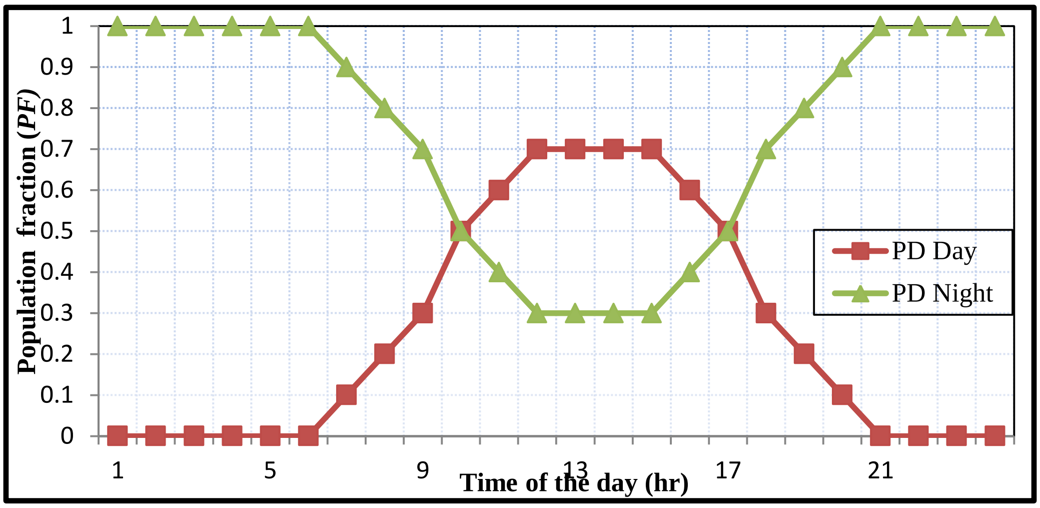

Figure 4.3 Population density *PD*(*t*), used in LUCY-HK as a function of hour of the day.

Table 4.2 Hourly population fraction (*PF*) integrates two population densities of day and night in LUCY-HK.

Hour	Fraction	Hour	Fraction
1	0	13	0.7
2	0	14	0.7
3	0	15	0.7
4	0	16	0.6
5	0	17	0.5
6	0	18	0.3
7	0.1	19	0.2
8	0.2	20	0.1
9	0.3	21	0
10	0.5	22	0
11	0.6	23	0
12	0.7	24	0

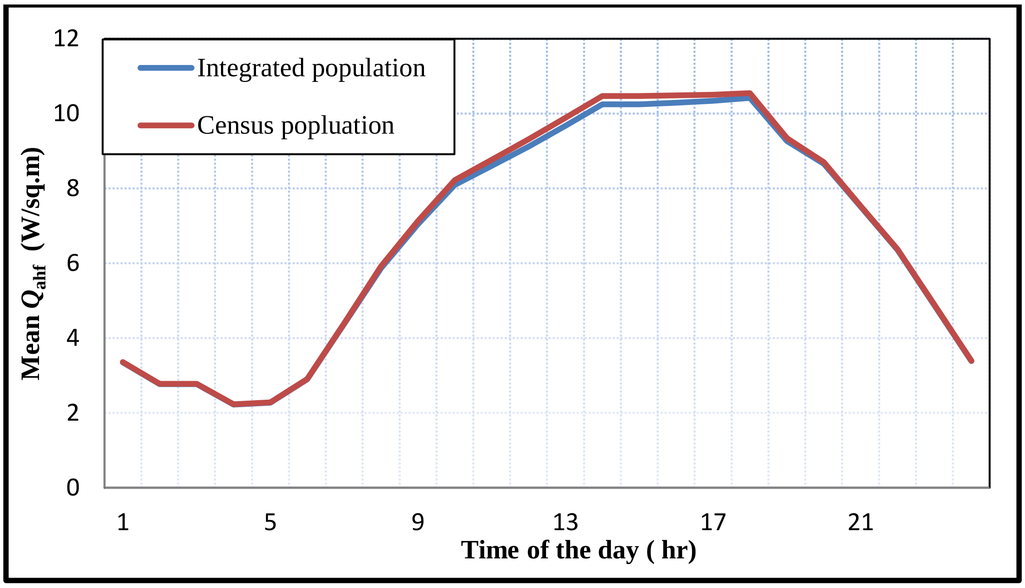

Figure 4.4 Mean Q_{ahf} determined in LUCY- HK (11-October-2012), using integrated population density (calculated in this study) and census population density (used unchanged Census population).

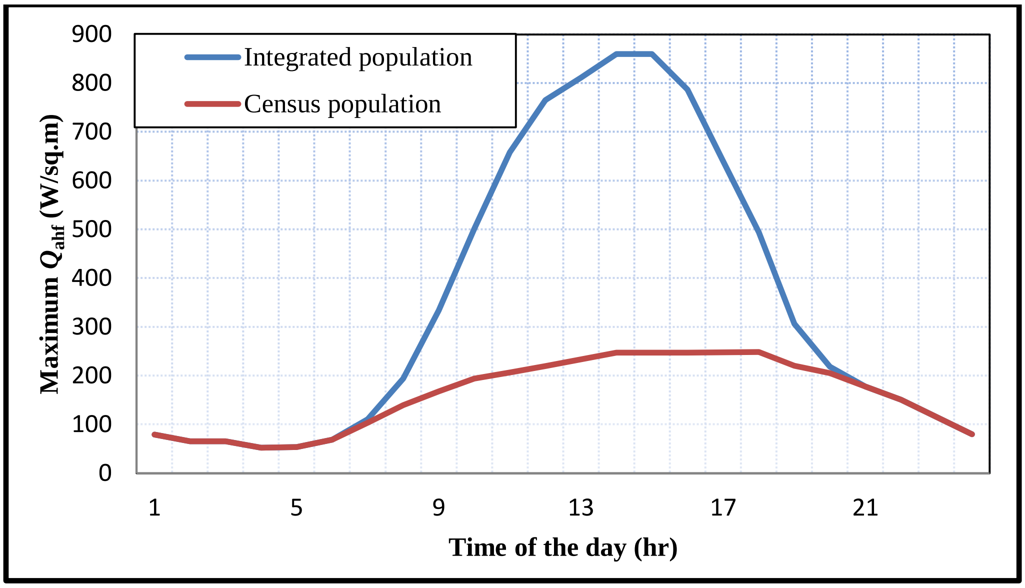

Figure 4.5 Maximum Q_{ahf} determined in LUCY- HK (11-October-2012), using integrated population density (calculated in this study) and census population density (used unchanged Census population).

Figures 4.4 & 4.5 show the mean and maximum values of $Q_{ahf,}$ using the integrated and original population datasets, respectively. The mean value of Q_{ahf} is identical because the mean of population density used remains the same in both datasets and is not affected by the redistribution of daytime population. However, due to augmented population density at the place of work during daytime, the intensity of Q_{ahf} as measured using the combined population density values is higher when compared to density estimated using the census data.

4.2.2 Vehicle heat

Vehicle emission is calculated based on the average number of cars, motorcycles, and freight vehicles (including buses) per 1000 people, from the data collected by the EPD (2014). In LUCY v2013a, the vehicle population of all countries is taken from the IRF World Road Statistics (Worldmapper, 2011).

The vehicle emission (Q_{veh}, Wm^{-2}) is calculated using the following equation:

$$Q_{veh} = \frac{[V_{car} \quad E_{car+} V_{mot} \quad E_{mot+} V_{fri} \quad E_{fri} \;] V_{fac} \; * 24 * PD \; * D * H_{fra}}{3.6 * 10^{12}} \tag{4.5}$$

where V_{car} is the number of cars per 1000 people, V_{mot} is the number of motorcycles per 1000 people; V_{fri} is the number of freight vehicles per 1000 people. E_{car}, $E_{mot,}$ and E_{fri} are the average emission factors of cars, motorcycles and freight vehicles in Wm^{-1}, respectively. V_{fac} is a multiplying factor used to change the total number of vehicles, D is the distance travelled over an hour (m), and H_{fra} is the hourly fraction of the daily number of vehicles. The daily maximum vehicle total can be obtained by multiplying the hourly number of vehicles by 24. A conversion to W m^{-2} is needed, therefore the population is divided by 10^{3}, and the hourly total is divided by 3600 (s) to get the average hourly vehicle emission. The emission factor for each vehicle is calculated based on the speed of the vehicle. In LUCY-HK, the vehicle speed is taken to be uniform over the study area, and limited to 16, 24, 32, 40, 48, 56 and 64 km/hr. The sensitivity of speed in LUCY-HK suggests that the intensity of Q_{ahf} to speed is not significant.

Vehicle emissions for speeds 24 and 48 km/hr on 11-October-2012 are shown in Figure 4.6. The increase in speed (24 to 48) raises the mean Q_{veh} by 0.1-0.2 W/m^{-2}; maximum difference is observed during peak hours (9 am to 6 pm). The difference in speed shows nominal impact on the mean Q_{veh}. Therefore, using a uniform speed in LUCY-HK is acceptable.

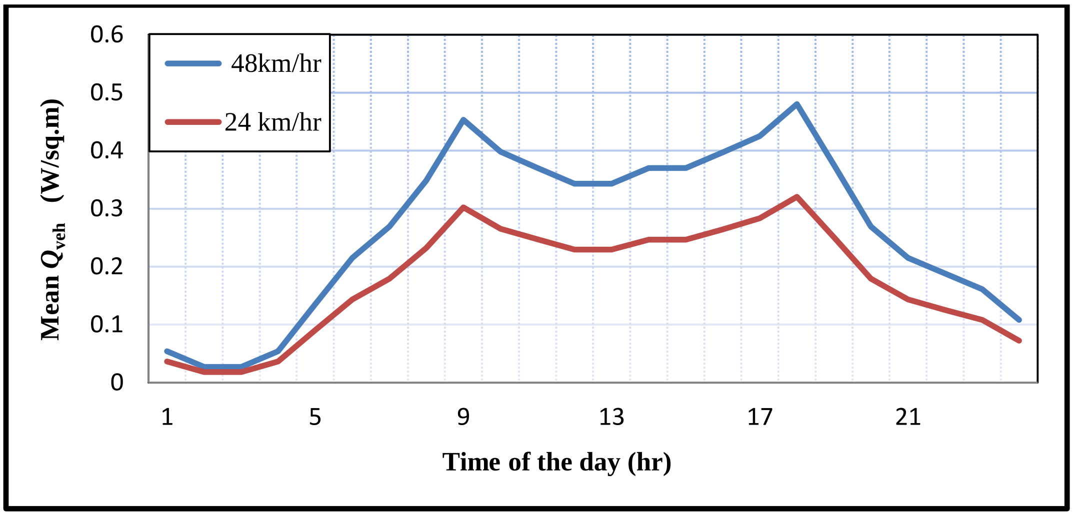

Figure 4.6 Hourly mean vehicle emission (Q_{veh}) determined in LUCY-HK, on 11-October-2012 at the speed of 24 and 48 km/hr.

The emission factors of the vehicles used in LUCY-HK are obtained from EPD (2014). The emission factors of LUCY v2013a are extracted from Smith *et al.* (2009).

V_{fac} is fixed at 0.7 (assumes 70% of the vehicles is on the road), and the diurnal profile depends on the period (time) and the day (weekday, weekend or public holiday). Information concerning public holidays is extracted from Worldmapper (2011). The diurnal pattern used in LUCY-HK is similar to that used in Allen *et al.* (2011). The variable H_{frac} depends on the type of the day (weekend/ weekday). The morning and evening peaks are estimated at 7.1% and 7.5 % of daily total traffic. Weekend total traffic volumes are assumed to be 20% less than weekdays (Allen *et al.*, 2010).

4.2.3 Building heat

Building heat is calculated based on the annual total end-use energy of buildings, available in Census and Statistics Department (2014). This energy data was originally collected by the Electrical and Maintenance Service Department. Heat emission of the building ($Q_{B,}$ Wm^{-2}) is determined using the following equation:

$$Q_{bui} = \frac{EC \quad PD \quad H_E \; T_{sf}}{P_t \quad 8.76*10^6} \qquad (4.6)$$

where, EC is the total energy consumption in kWh, H_E is the hourly energy use, and T_{sf} is the mean monthly temperature estimated relative to the balance point (Ruth and Lin, 2006); (Allen *et al.*, 2011). Further, P_t is the total population of Hong Kong during iteration, and PD is the population density estimated in this study.

In LUCY-HK, end-use energy is preferred over primary energy consumption drawn from International Energy Statistics for each country (EIA, 2013) which was originally used in LUCY v2013a. The EIA data of Hong Kong originated from the Census and Statistics Department of Hong Kong. Comparisons between the two datasets and the purpose of using end-use energy in LUCY-HK are clarified below.

Case 1: The primary energy consumption in any country in the EIA database is based on the energy (petroleum, dry natural gas, coal and electricity) import into the country. The imported products are converted directly into primary energy using standard combustion rates without considering any losses (EIA, 2009).

Case 2: End-use energy data of Hong Kong are measured at buildings in various sectors (residential, commercial, and industrial) (Electrical and Maintance Services Department 2014). The electricity and gas consumption at each building of Hong Kong is gathered as monthly and annual end-use energy of Hong Kong.

Using primary energy (Case 1) consumption to estimate Q_{bui} in LUCY-HK overestimates building heat emission significantly because, conversion and transmission losses in Hong Kong accounts for 39% of total energy use, compared with 15.8% in the United States (Newcombe, 1975). The rate of conversion and transmission might decrease over time; however, the loss of energy during production may continue to remain significant. Moreover, in Hong Kong, imported fuels are not consumed entirely; after consumption, some are stored for future demand while others are exported to China (Electrical and Maintenance Services Department, 2014). Hence, application of end-use energy values to estimate Q_{bui} in LUCY-HK may be appropriate when it is assumed that the electricity and gas consumed by buildings are equal to the energy released at the building. The annual energy is fragmented into hourly energy consumption (neglecting the time delay of storage heat mission). Results from using primary energy and end-use energy on Q_{bui} of LUCY-HK are presented in Figure 4.7.

The end-use energy data are converted from terajoules to kilowatts per hour, and multiplied by 1000 to arrive at watts per hour, and then divide the result by the number of hours in the year (8,760).

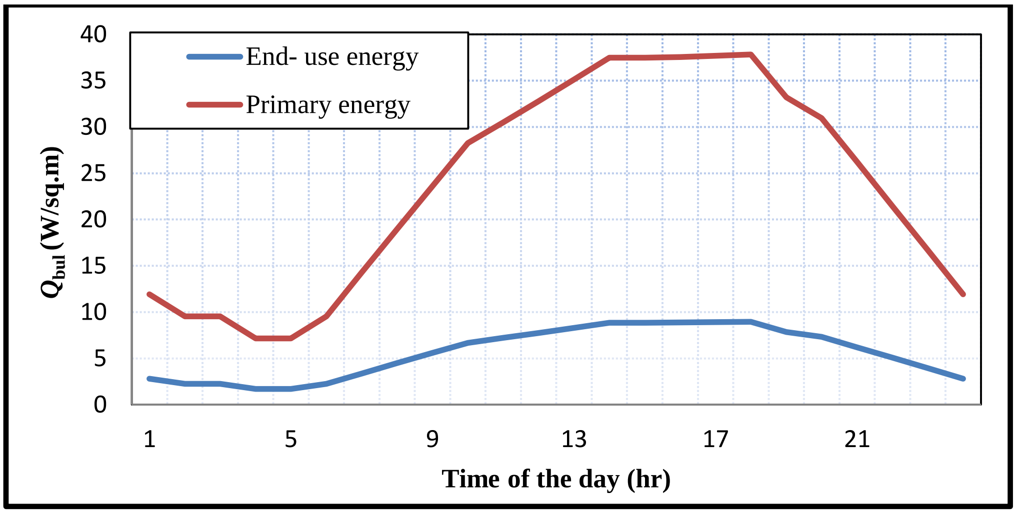

Figure 4.7 Building heat emission (Q_{bui}) on 11th-October-2012 of LUCY-HK using (a) End-use energy (Electrical and Maintanance Services Department, 2014) and (b) Primary energy (EIA, 2013).

Air temperature is a significant factor in estimating energy use within buildings. It causes increased use of heating in winter or air conditioning during the summer. This building energy use, which is a significant portion of the total energy used (Eiker, 2009), results in heat release externally into the urban environment (Lindberg *et al.,* 2013). The internal temperature of the building is considered thermally comfortable at a threshold termed the temperature balance point (TBP); deviation from the balance point results in an increase in energy requirement either for heating or cooling (Lindberg *et al.*, 2013). Nicol and Humphreys (2002) found this temperature balance point to be equivalent to a monthly average air temperature of 12^{o}C, the value found to be valid in different regional climates (Lindberg *et al.,* 2013); Different climatic regions and different building types can have different balance point temperature (Amato *et al.,* 2005). Hence, the identification of suitable balance point for Hong Kong is necessary.

Two climatic indices, namely cooling degree-day (CDD) and heating degree-day (HDD) (Lee *et al.,* 2010), are used here to define the balance point temperature or the base temperature (a temperature used to define CDD and HDD). CDD has been used to assess the climate impact on cooling energy consumption in subtropical climate regions (Lam, 1995). HDD has commonly been utilized to evaluate the heating requirement in temperate and cold climatic regions (Eto, 1988; Day and Karayiannis, 1999; valour *et al.,* 2001; Lee *et al.,* 2010).

CDD and HDD specify the condition of cooling or heating respectively, during a given period. These two parameters are used to identify the number of hot and cold days of a place. Monthly CDD (HDD) is the monthly mean of the differences between the daily average air temperatures and the balance point temperatures. The larger the magnitude of CDD (HDD), the more cooling (heating) is required (Lee *et al.,* 2010).

In LUCY v2013a, Lindberg *et al.* (2013) define HDD (CDD) in relation to national income which varies with time (*t*, years). For each year, HDD and CDD are calculated relative to 12^{o}C using the Wilmot *et al.* (2009) 0.5×0.5 degree terrestrially gridded monthly temperature dataset (available for 1901–2008). The combined total annual HDD and CDD (HDD + CDD) are determined for each country for each year (Lindberg *et al.*, 2013).

In the case of LUCY-HK, the gridded temperature dataset of Wilmot *et al.* (2009) is swapped with the monthly mean air temperature measured at Hong Kong observatory. A uniform temperature grid of 100m by 100m (similar to the grid in the population dataset) is created, and it is assumed that the heating and cooling demands are uniform throughout the study area.

Nicol & Humphreys (2002) identified the comfortable temperature of a ventilated building as 18^{o}C, when the outside air temperature is 12^{o}C. The comfortable indoor temperature (T_{cf}) can be expressed in terms of the mean outdoor air temperature (T_{od}) as

$$T_{cf} = 13.5 + 0.54\ T_{od} \tag{4.7}$$

Equation 4.7 can be used to determine the balance point temperature of Hong Kong, but free-running ventilated buildings in Hong Kong are very few, and measuring the balance point locally from the air temperature is beyond the scope of this study. Hence, the balance point commonly used in previous studies in Hong Kong is used while executing LUCY-HK. Lam (1995) conducted a study based on 33 years of measured weather data to identify CDD and HDD for Hong Kong and suggested the balance points of 18^{o}C and 24^{o}C, respectively, for residential and commercial buildings in Hong Kong. However, the study was limited to commercial and residential buildings alone; which may not be suitable for other types of buildings in Hong Kong. Meanwhile, Minstry of Housing and Urban-Rural Development of the People's Republic of China (2005) suggest separate balance points for CDD (26^{o}C) and HDD (18^{o}C). It is widely adopted in several studies of Hong Kong observatory; hence, it is also used in LUCY- HK.

The balance point has a substantial impact in building heat (Q_{bui}) estimation. The sensitivity of LUCY-HK to the balance point can be described as a sensitivity graph. Figure 4.8 shows the response of building emission (Q_{bui}) to different balance point

(Table 4.3) used in a day, where 12°C is used in LUCY v2013a, 18°C is proposed by Nicol & Humphreys (2002), 21°C — the mean value of the recommended balance point of Lam (1995) (commercial buildings: 18°C and residential buildings: 24°C), and 26°C & 18°C as suggested by Minstry of Housing and Urban-Rural Development of the People's republic of China (2005).

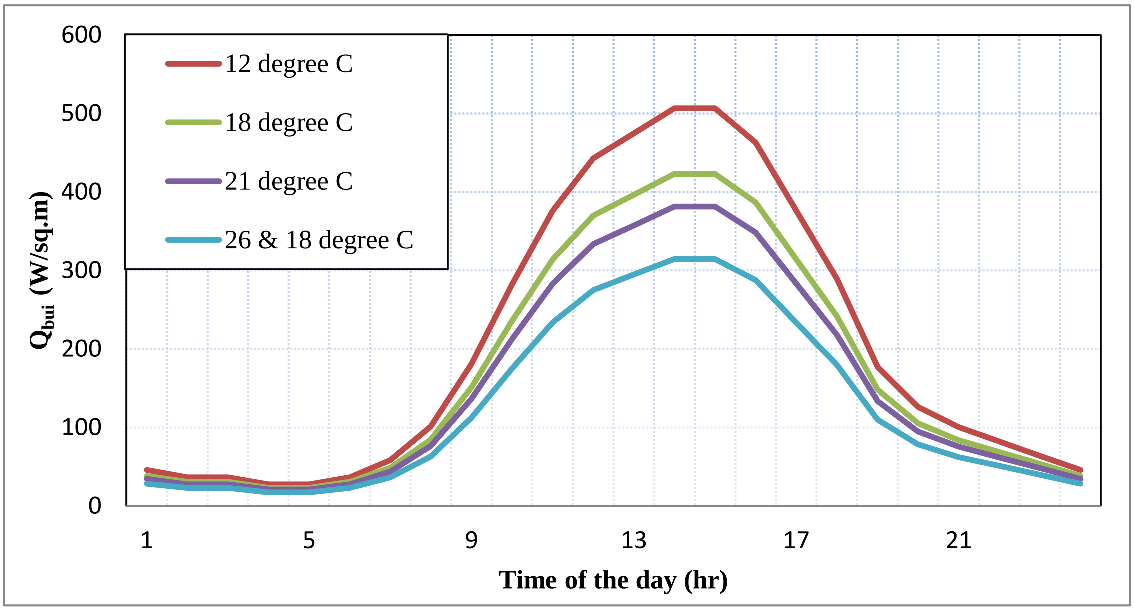

Figure 4.8 Hourly building heat emission Q_{bui} response to different balance points in LUCY-HK for 11th –October-2012.

Table 4.3 Different balance points used in LUCY-HK and its sources

Balance point °C	**Source**
12	LUCY v2013a
18	Nicol & Humphreys (2002)
21	Lam (1995)
26 CDD &18 HDD	Ministry of Housing and Urban-Rural Development of the People Republic of China (2005)

4.2.4 Spatial averaging

The magnitude of the anthropogenic heat flux is highly dependent on the spatial scale at which it is estimated (Lindberg *et al.*, 2013). In cities, pixels with higher values of Q_{ahf} are associated with large buildings and busy roads. The increase in spatial resolution increases Q_{ahf} over urban areas and Q_{ahf} is reduced when spatial resolution is minimized. Lindberg *et al.* (2013) examined LUCY v2013a at different spatial resolutions in London. It is useful to resample input datasets of different spatial resolutions into a standard spatial resolution and enable the derivation of the output at any spatial resolution irrespective of the input resolution. The importance of choosing an appropriate spatial resolution and the intensity of Q_{ahf} at various spatial resolutions is discussed in Lindberg *et al.* (2013).

In this study, the output spatial resolution of LUCY-HK is limited to 100m ─ similar to the input dataset resolution of 100m by 100m. However, in principle, LUCY-HK is capable of working at any spatial resolution.

4.3 Results and Discussion

The output from LUCY-HK is generated as hourly grids in ESRI ASCII format. A video file to display spatial variations during the diurnal cycle is recorded in .avi format. Descriptive statistics such as mean, median, minimum, maximum, standard deviation and IQ are calculated for all the elements of Q_{ahf} for each hour and stored in a text file.

4.3.1 Sensitivity of LUCY-HK to various input parameters

The sensitivity of LUCY-HK to changes in the variables is examined by changing a single variable over a day (17$^{\mathrm{th}}$ September 2009) in Figure 4.9. It is tested with 10% increase and decrease in the input variable. Anthropogenic heat ($Q_{\mathrm{ahf)}}$ increases for each variable increase, and decreases when each variable is reduced.

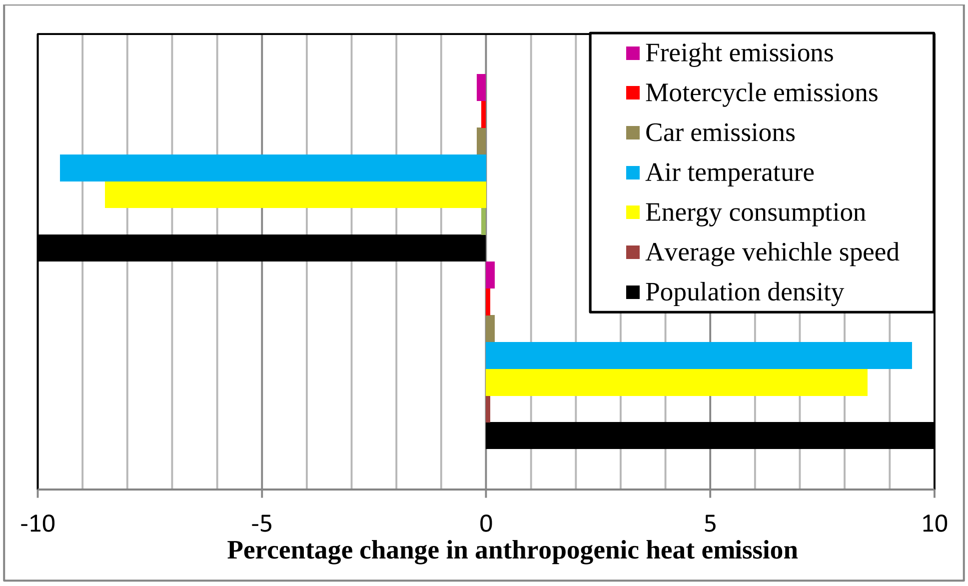

Figure 4.9 Sensitivity analysis of a +10% and -10% changes to variable in LUCY- HK

Population density has the greatest impact on the results of LUCY-HK, with 10% increase in Q_{ahf} following a 10% change in the input population density. Air temperature changes the Q_{ahf} by 9% for a 10% change in input value. Energy consumption increases the Q_{ahf} by 8.5% from a 10% change in the input value. Emission standards and vehicle speed have less than 1% impact on the overall Q_{ahf} for a 10% change in the respective input variables.

The sensitivity of balance point has been made separately using the values given by Ministry of Housing and Urban-Rural Development the People's Republic of China (2005). For a hot summer day (13th September 2009), a 10% increase in CDD resulted in a 15% decrease in Q_{ahf}. i.e. CDD value increased by 10% reduces the cooling requirement by 15%.

4.3.2 Diurnal variation of anthropogenic heat flux

The diurnal variations in anthropogenic heat over a day (30th November 2007) are plotted in Figures 4.10 and 4.11. Note the higher anthropogenic heat releases during daytime with a maximum emission of around 680 W/m^2 at 02 pm for a 100m spatial resolution. Building heat dominates other emissions of Q_{ahf}. Transition periods are associated with moderate emission, while the rest of the diurnal cycle experience relatively lowers anthropogenic heat flux.

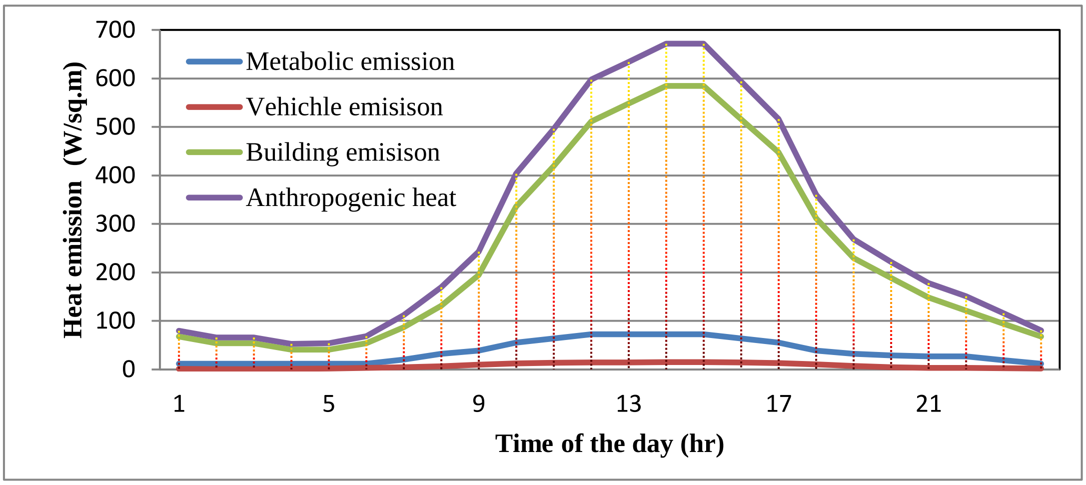

Figure 4.10 Hourly maximum emissions of Q_{ahf} and all its components in LUCY-HK as of 30th November 2007.

Figure 4.12 shows the percentage contribution of each component of Q_{ahf} for every hour. Note that with a mean of 82%, building emission dominates during the entire diurnal cycle while metabolic emission *t* contributes 15% and vehicle emission contributes 3% to total Q_{ahf}.

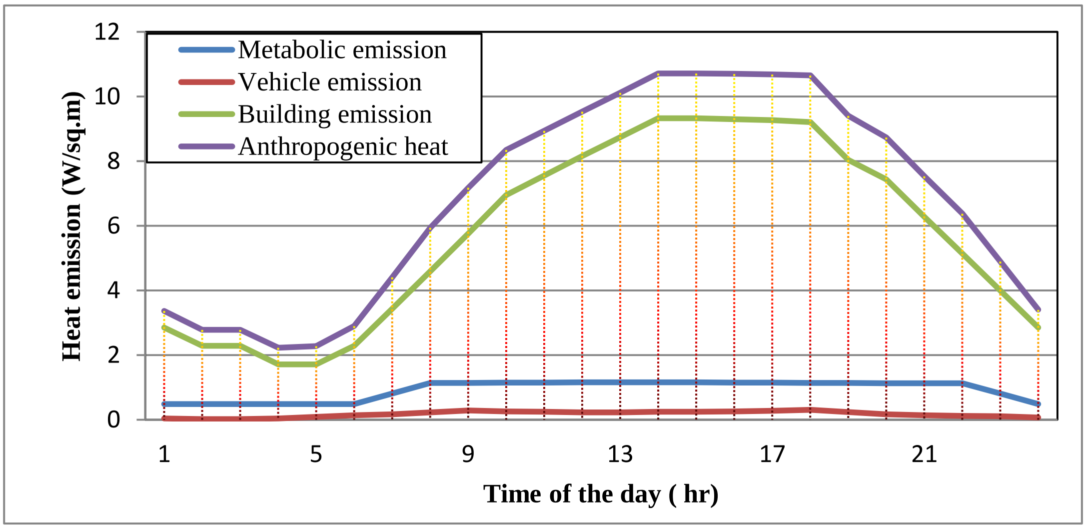

Figure 4.11 Hourly mean emissions of Q_{ahf} and all its components in LUCY-HK as of 30th November 2007.

Figures 4.10 and 4.11 show similar diurnal patterns for the dates specified. The intensity of mean anthropogenic heat emission is lower than the maximum emission values. The higher Q_{ahf} emission values are observed over the urban areas other places exhibit relatively lower values. Higher emission values are seen during the afternoon (higher anthropogenic activity) and lower emissions over the remaining periods.

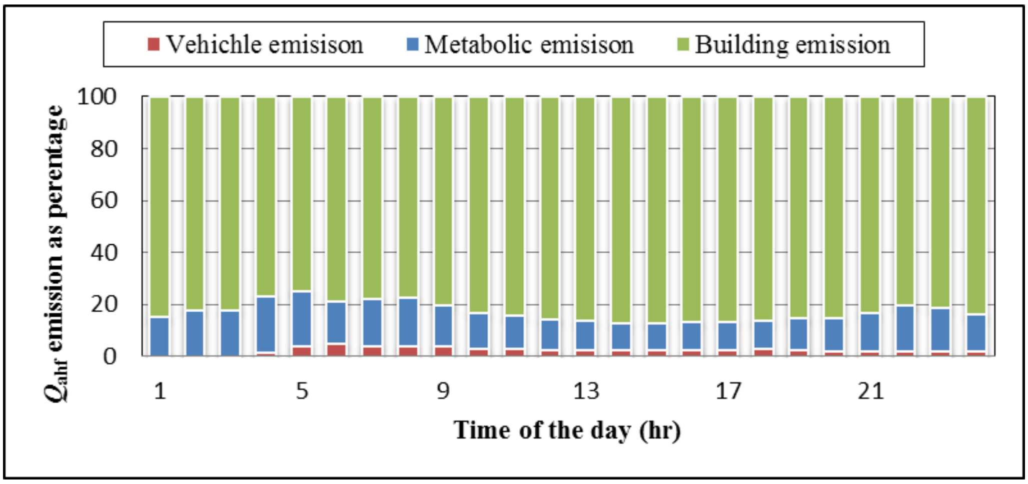

Figure 4.12 LUCY-HK - Hourly contribution to anthropogenic heat (Q_{ahf}) by its components in percentage.

4.3.3 Spatial variation of anthropogenic heat during different time of the diurnal cycle

Figures 4.13, 4.14, 4.15 and 4.16 are maps of anthropogenic heat as estimated for 31-November-07 at 10 am, 02 pm, 06 pm and 11 pm respectively. The intensity of Q_{ahf} is quite high over commercial and residential areas but is lower or negligible at rural locations. During the day, Central and Wan Chai on Hong Kong Island, and a part of the Kowloon peninsula experience the greatest Q_{ahf} because of higher population densities in these places during working hours. During the night, suburban towns have greater Q_{ahf}.

Figures 4.13 and 4.14 represent anthropogenic activity in the city during the day. Figure 4.16 shows the intensity of anthropogenic activity during the night over Hong Kong. Detailed spatial analyses of LUCY-HK for different times of day and different seasons will be disused in chapter 6.

The movement of population is accounted for in the spatial variability of Q_{ahf} intensity over time as estimated by LUCY-HK. Extracting pixels from urban areas alone will increase the mean value considerably. Otherwise, the value is considerably reduced due to the majority of pixels being associated with rural areas. A detailed LUCY-HK over urban areas and comparison with other models (remote sensing and GIS based models) will be discussed in later chapters. Since urban areas are the primary focus of this study, the study area is reduced to part of Kowloon and Hong Kong Island for comparing model outputs.

The Hong Kong international airport is excluded from LUCY-HK because the exact population density and the number of aircraft and the resulting emissions are not known.

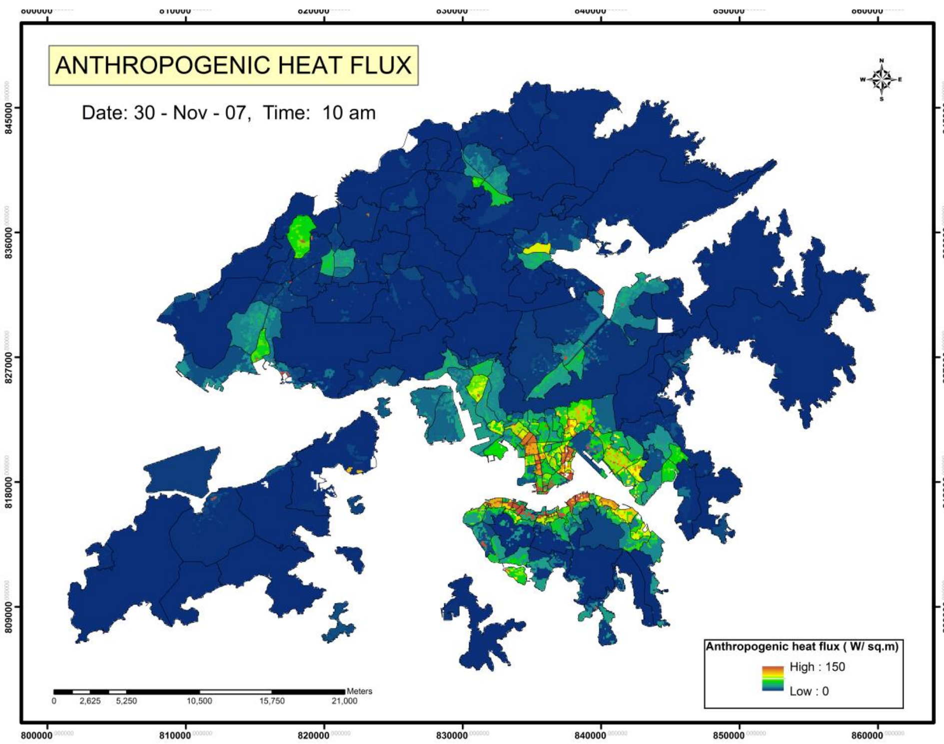

Figure 4.13 Anthropogenic emission (Q_{ahf}) of LUCY-HK at 10 am on 30th November 2007.

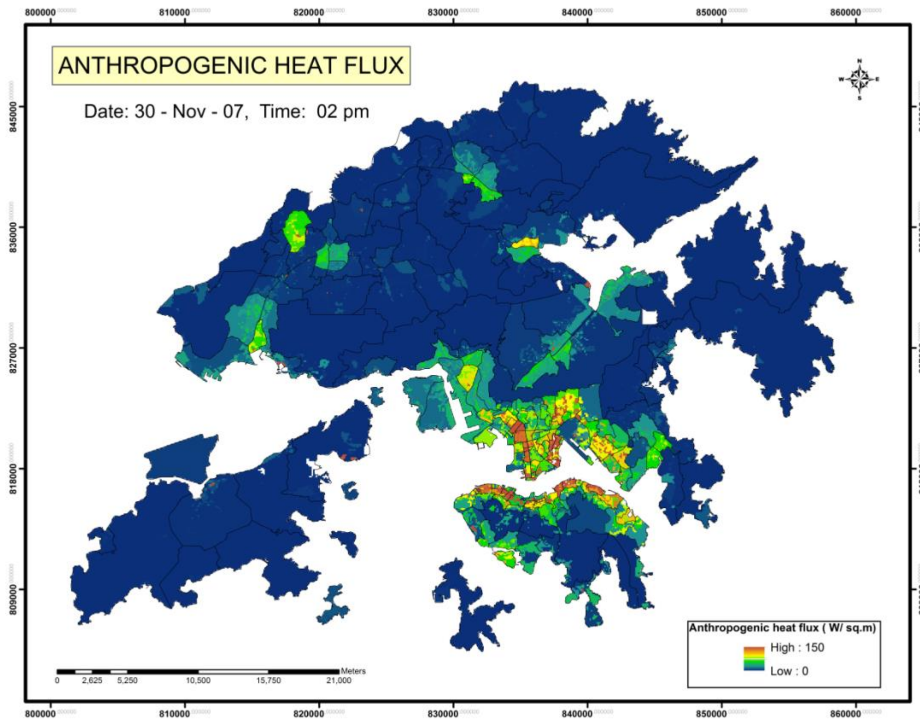

Figure 4.14 Anthropogenic emission (Q_{ahf}) of LUCY-HK at 02 pm on 30th November 2007.

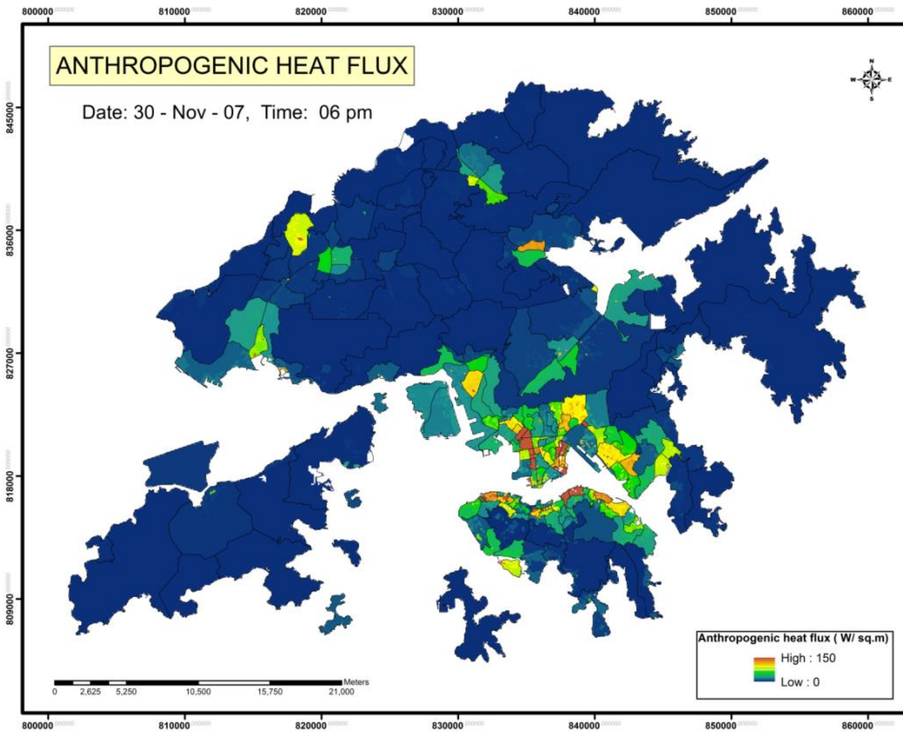

Figure 4.15 Anthropogenic emission (Q_{ahf}) of LUCY-HK at 06 pm on 30th November 2007.

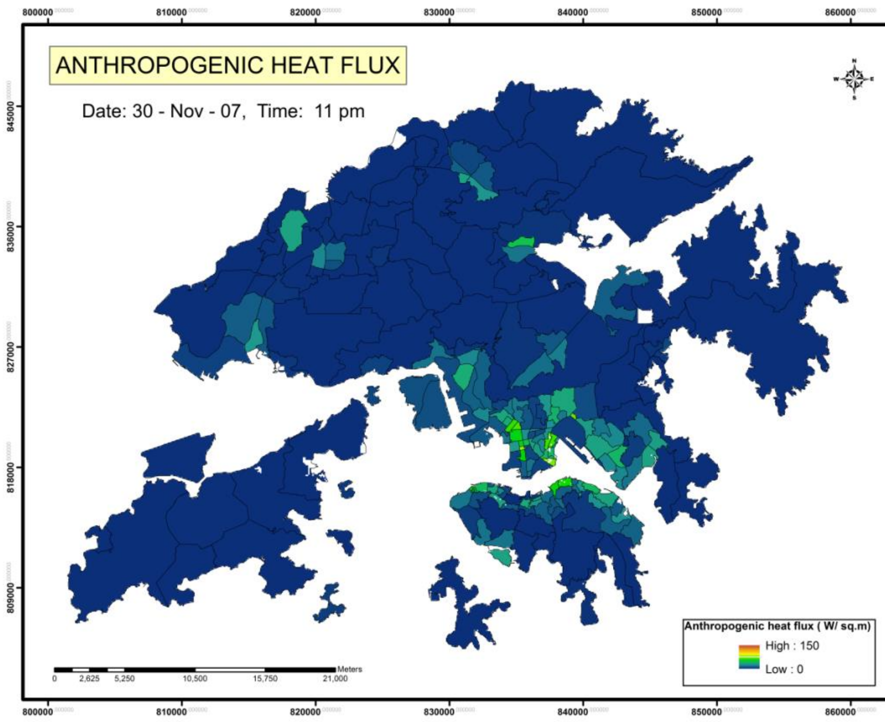

Figure 4.16 Anthropogenic emission (Q_{ahf}) of LUCY-HK at 11 pm on 30th November 2007.

4.3.4 LUCY-HK: Limitation and suggestions for improvement

As discussed earlier, the accuracy of LUCY-HK model output depends on the scale of input variables. Couple of improvement are possible in LUCY-HK which are left for the future works. a) For a highly dense city such as Hong Kong a 100 m resolution may not be sufficient to arrive at a detailed Q_{ahf} distribution. It can be improved by using a population dataset at scale less than 100 m, b) The monthly energy consumption data should be used instead of annual energy consumption and c) Temperature scheme should be modified to enable the model to be more sensitive to seasonal variations in Q_{ahf}. It can be obtained by using replacing uniform air temperature grid over the study area with air temperature measured across the city using automated weather stations. In such a case, the intensity of Urban Heat Island will be well accounted for.

Chapter 5

ANTHROPOGENIC HEAT FLUX MODELLING OF HONG KONG USING A GIS BASED MODEL

5.1 Introduction

In the early decades of computer-based regional-scale atmospheric modelling, urban surfaces were poorly represented in models (Sailor, 2011). As interest grew, the scales and representations of the models have improved. Several studies were carried out quite early to understand urban thermal environments. Some used a simple modelling framework (e.g., Myrup, 1969; Richiardone and Brusasca, 1989; Anthes, 1990; Sailor, 1995; Taha, 1996) that represented an urban area as a flat surface (soil) whose thermal properties are estimated as weighted averages of the construction materials used in the city (Sailor, 2011). Later studies (e.g., Masson, 2000; Lemonsu and Masson, 2002; Martilli *et al.*, 2002; Otte *et al.*, 2004; Dupont and Mestayer, 2006) incorporated more sophisticated parameterisation schemes that sought to capture the impacts of urban morphology on energy and momentum exchanges (Sailor, 2011).

Heat and moisture emissions associated with energy consumption were simply ignored in many urban climate studies (Sailor, 2011). The emissions included those from vehicles, humans and buildings in urban areas. Several studies estimated these at city scales using an inventory-based approach based on GIS (Geographic Information System) datasets (e.g., Grimmond, 1992; Ichinose *et al.*, 1999; Smith, 2009). The present study also uses a GIS-based inventory approach that is broadly in line with Smith *et al.* (2009) who had extended the work of Grimmond (1995). In the present study, Q_{ahf-L} and its components are calculated at a resolution of 100×100 m. Smith *et al.* (2009) limited the size of the output grid squares to 200×200 m, Grimmond (1992) and Pigeon *et al.* (2007) used 100×100 m, while Ichinose *et al.*

(1999) chose 250×250 m. The scale of an output grid cell impacts the selection of the input data sources and the output morphology of the urban surface. In view of the higher population density and complex urban environment, it is important to map anthropogenic heat emission at a finer scale in the case of Hong Kong.

With a view to enabling the comparison of the results of the GIS model with those from a remote sensing-based model based on a 90 m pixel size and the LUCY-HK model, the output grid resolution of our model is 100×100 m. The emissions measured over the building and roads are aggregated for each 100 m grid square.

5.2 Methodology

The sources of anthropogenic heat (Q_{ahf-L}, Wm^{-2}) are separated into three parts:

$$Q_{ahf-L} = Q_{met-L} + Q_{bui-L} + Q_{veh-L} \quad (5.1)$$

where, Q_{met-L}, Q_{bui-L}, and Q_{veh-L} are the metabolic, building and vehicular emissions, respectively. Although metabolic emissions are often assumed to be negligible relative to vehicle and building heat production, they are incorporated into our model for completeness (Smith *et al.*, 2009). Similar to some previous studies (Ichinose *et al.*, 1999; Kondo and Kikegawa, 2003; Betts and Best, 2004; Smith *et al.*, 2009), the model considers anthropogenic heat emission to be equal to the energy consumed by the emission sources. The lag between consumption and emission of energy has implications for the diurnal anthropogenic heating profile (Smith *et al.*, 2009). To compensate for the delay in emission, only a fraction is used. Details of the fractions used in our model will be discussed in the respective sections in this chapter dealing with metabolic, vehicular and building heat emission calculations.

In LUCY-HK, emissions are not calculated by the hour. Instead, the calculations are limited to the overpass times of the ASTER satellite, which are used to calculate the anthropogenic heat figures used in the remote sensing model. The night and day overpass times of ASTER in Hong Kong are close to 11 pm and 11 am, respectively.

Therefore, the model emission calculations are constrained to 11am on 30th November 2007, 13th September 2008, and 22nd August 2009, and 11pm on 31st January 2007, 13th August 2008, and 17th September 2009.

In this chapter, the anthropogenic heat values estimated for 22nd August 2009 at 11am and for 17th September 2009 at 11pm will be discussed as daytime and night-time examples, respectively. The spatial characteristics and the intensities of anthropogenic heat emissions and its components will be explained later in this chapter. Figure 5.1 shows the methodology used for calculating anthropogenic heat and its components.

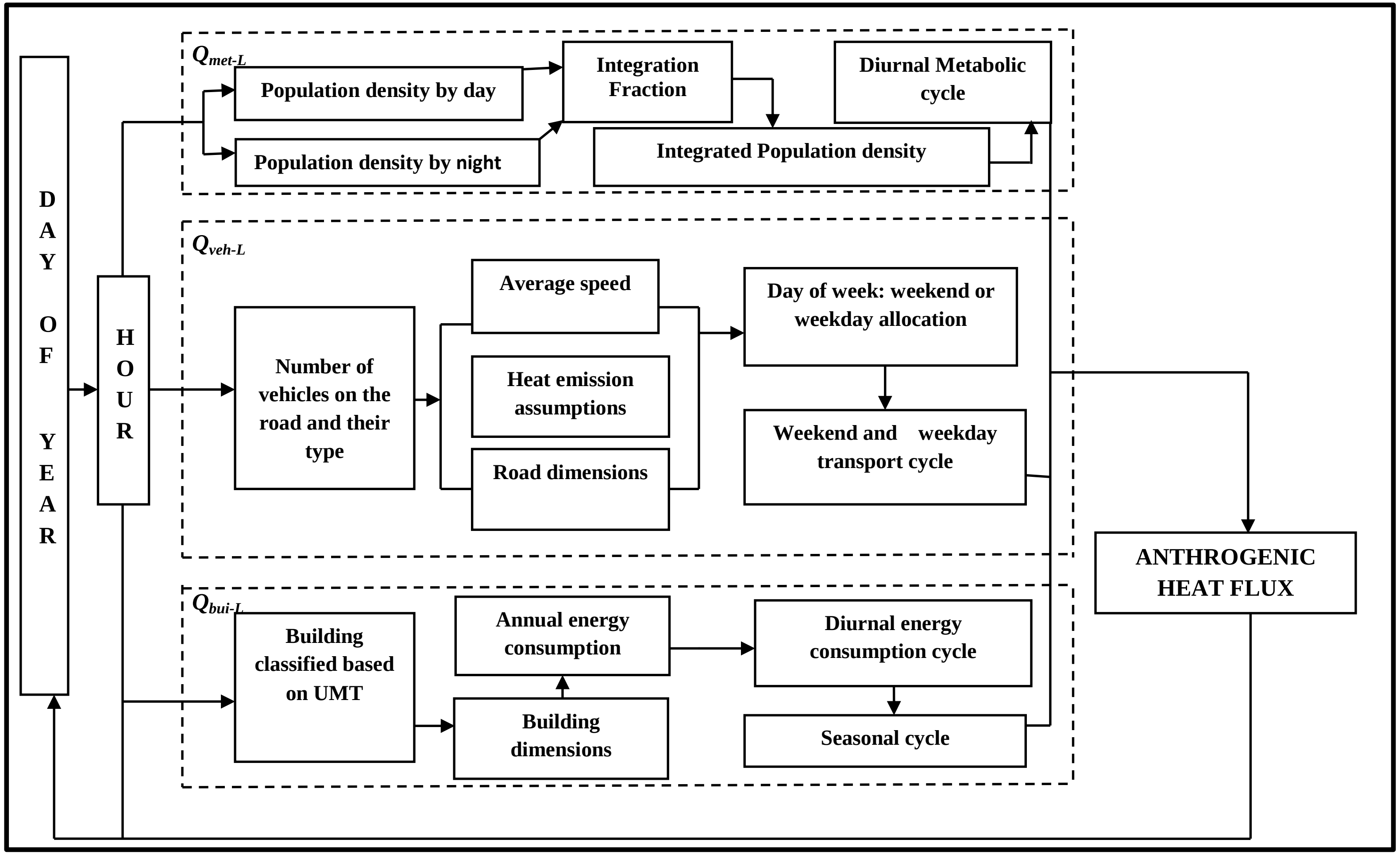

Figure 5.1 Flowchart of GIS based anthropogenic heat model using a bottom-up approach.

5.2.1 Metabolic heat emissions (Q_{met-L})

Emissions due to the metabolic activities of people are calculated based on the population density values of the respective grid cells. The rate of metabolism varies according to the activity level of people in a diurnal cycle, ranging from 70 W while sleeping to over 800 W for vigorous activity (Smith *et al.*, 2009). As for Hong Kong, the population density of each tertiary planning unit (TPU) is extracted from the population census of the Census and Statistics Department of Hong Kong (2013). Daytime population values are used along with the Census population figures to create integrated population density figures. The integrated population density is utilized to estimate the metabolic heat emission of each grid cell. The methods used are similar to those used in LUCY-HK (see Chapter 4).

5.2.2 Building heat emissions (Q_{bui-L})

The emissions sourced from HVAC (heating, ventilation and air-conditioning) including cooking and other utilities within the building are quantified using a bottom-up approach. Due to difficulties in apportioning aggregated energy consumption statistics to a fine spatial resolution (Harrison *et al.*, 1984), the present study has modified, the novel method utilized in Smith *et al.* (2009). The method allows buildings to be categorized according to their locations in the respective land use zones. Smith *et al.* (2009) used a random sampling method to quantify surface cover fractions (the proportional cover figures for different land surface types) of the Urban Morphology Types (UMT), and calculated the built footprint area by adding the total area of built surface cover in each UMT within a grid cell. Instead of estimating approximate proportional covers using randomly sampled grids, we derived the proportional surface cover fraction for each grid cell using the digital land use file obtained from the Planning Department of Hong Kong. The land use consists of 27 UMTs (listed in Table 5.1). For this study the map is divided into a uniform grid (a reference grid) of 100 m squares over the study area. The resulting UMT grid cell holds a unique number (referred to as the aggregate surface cover fraction of a UMT within the grid) when two or more polygons of the same UMT fall within the grid. The UMT layer intersected with a uniform grid is overlaid into the three-dimensional building polygon at 1:5000 scale to calculate the built cover fraction inside each UMT. The built cover fractions associated with each UMT are exported as separate layers, and multiplied with the typical energy consumption of buildings in the UMT.

The method used by Smith *et al.* (2009) for building heat (Q_{bui-L}, Wm^{-2}) estimation is as follows:

$$\boldsymbol{Q_{bui-L}} = \frac{\sum(\boldsymbol{A}_{\mathbf{UMT}}\,\boldsymbol{BC}_{\mathbf{UMT}}\,\boldsymbol{EC}_{\mathbf{UMT}}(\boldsymbol{t}))}{\mathbf{A_x}} \tag{5.2}$$

where, BC_{UMT} is the built surface cover fraction of each UMT, EC_{UMT} is the typical energy consumption of buildings associated with the UMT, and A_x is the area per grid square (100,00 m^2).

In this study, the above process is simplified by replacing the built cover fraction with the area of building in each UMT within the pixel:

$$\boldsymbol{Q_{bui-L}} = \frac{\sum(\boldsymbol{BA}_{\mathbf{UMT}}\,\boldsymbol{EC}_{\mathbf{UMT}}(\boldsymbol{t}))}{\boldsymbol{A_x}} \tag{5.3}$$

where, Q_{bui-L} is the building heat emission (Wm^{-2}), BA_{UMT} is the planar area of buildings associated with different UMTs in a pixel, *EC* is the typical energy consumption of buildings associated with the UMT, A_x is the area per grid square (100,00 m^2).

The method is further improved by considering the volume of the building instead of the building area. However, since the formula limits the use of volume, the volumes of buildings are normalized with the mean height of buildings in a pixel:

$$\boldsymbol{Q_{bui-L}} = \frac{\sum(\boldsymbol{nBA}_{\mathbf{UMT}}\,\boldsymbol{EC}_{\mathbf{UMT}}(\boldsymbol{t}))}{\boldsymbol{A}_{\mathbf{x}}} \tag{5.4}$$

where, nBA_{UMT} is the normalized building area which is equal to the building volume divided by its mean height.

Table 5.1 Proportional built surfaces of each UMT and typical energy consumption as extracted from the Electrical and Maintenance Services Department for buildings of each UMT category. The UMT are categorized according to the recorded land utilization in Hong Kong (Planning Department, 2013).

UMT Category	Built surface cover fraction (BC_{UMT})	Typical energy consumption (EC_{UMT}, Wm^{-2})
Residential		
Private residential	0.2175	13
Public residential	0.2256	17
Rural settlements	0.1110	12
Commercial		
Commercial/Business and offices	0.3209	73
Industrial		
Industrial land	0.3070	16
Industrial estates	0.2392	16
Warehouse and open storage	0.0357	41
Institutional/Open Space		
Government, institutional and community facilities	0.1750	34
Open space	0.0185	34
Transportation		
Roads	N/A	N/A
Railways	0.4723	73
Airport	0.0492	73
Other Urban or Built-up Land		
Cemeteries and crematoriums	0.0051	34
Utilities	0.0876	34
Vacant development land	0.0093	13
Others	0.0683	34
Agriculture		
Agricultural land	0.0079	4
Fishponds/ Gei ways	0.0005	4
Woodland/ Shrub land/ Grassland/ Wetland		
Woodland	0.0003	12
Scrubland	0.0004	12
Grassland	0.0013	12
Mangroves and swamps	0.0002	12
Barren Land		
Bad land	0.0000	12
Quarries	0.0021	16
Rocky shore	0.0001	16
Water Bodies		
Reservoirs	0.0001	16
Streams and nullahs	0.0007	16

For urban parts of Hong Kong, considering the planar footprint area of the building will underestimate building heat emissions. Due to the presence of high rise buildings and very high building density, the use of equation 5.4 is more appropriate than equation 5.1.

Energy consumption in a building is estimated based on indicators for residential, commercial and transport sector data collected by the Electrical and Mechanical Engineering Services Department (EMSD) of Hong Kong. EMSD derives the energy consumption indicators of different sectors from the studies on a limited size of samples within the populations of the respective energy-consuming groups (Electrical and Mechanical Services Department, 2013). Each sector contains several principal groups and subgroups. For example, the commercial sector contains nine principal groups: restaurants and retailers, accommodations, hospitals and clinics, educational services, warehouses, office flatted factories, central services for shopping arcades, private offices, and government offices. The nine principal groups are further classified into 32 sub-groups. For example, Educational Services, a principal group, is classified into seven sub-groups: universities, postsecondary colleges, adult education / tutorial / vocational courses, secondary schools, primary schools, kindergartens and special education schools. The building energy consumption of the UMTs are estimated by relating them to the energy consumption indicator values of the subgroups.

Some UMT types consist of several subgroups. In such cases, the sub-groups are weighted to calculate the value for each UMT. For example, the UMT category labelled GIC Educational (representing the surface cover of educational institutions in the UMT type Government, Institutional and Community facilities) doesn’t have a direct energy consumption indicator. Therefore, the values of the sub-groups (universities, postsecondary colleges, adult education / tutorial / vocational courses, secondary schools, primary schools, and kindergartens and special education schools in the case of Educational Services) are weighted while calculating the energy indicator value.

The energy indicator values for UMTs with lower built surface cover (<1%; cemeteries and crematoriums, vacant development land, agricultural land, fish ponds, woodlands, shrub lands, grasslands, mangroves and swamps, bad lands, quarries, rocky shores, reservoirs, and streams and nullahs) are assumed to be equal to the energies indicated for the respective UMTs. For example, for agriculture, buildings have not been considered in the energy consumption indicator of EMSD. However, in this study, the energy consumption indicator for agriculture is estimated by making two assumptions, 1) all agricultural land is located in the rural areas, and 2) all buildings on agricultural land are rural settlements although, in reality, they may include buildings of motor rooms, agro-based industries, and the like. Since the primary focus of this study is on urban areas, minor variations in building energy estimation caused by the two assumptions are assumed to be negligible.

In EMSD, the energy consumption indicator of a building is given as the annual energy consumption per area (MJ/m^2/annum). The area is expressed in terms of the Gross Floor Area (GFA) defined as the area contained within the external walls of the building measured at each level, including the basement, but excluding any plant rooms, car parks and loading bays (Electrical and Maintenance Services Department, 2013). The annual energy consumption is broken down into monthly energy consumption (expressed as a fraction) which represents the ratio of energy consumed during each month to the total energy consumed during the particular year. The monthly energy consumption figures are extracted from the Hong Kong Monthly Digest of Statistics, Census and Statistics Department (2014). Figure 5.2 shows the percentage of monthly energy consumption with respect to the annual consumption value for the year 2011. Figure 5.3 lists the sector wise monthly energy consumption figures expressed as proportions of the annual consumption magnitudes.

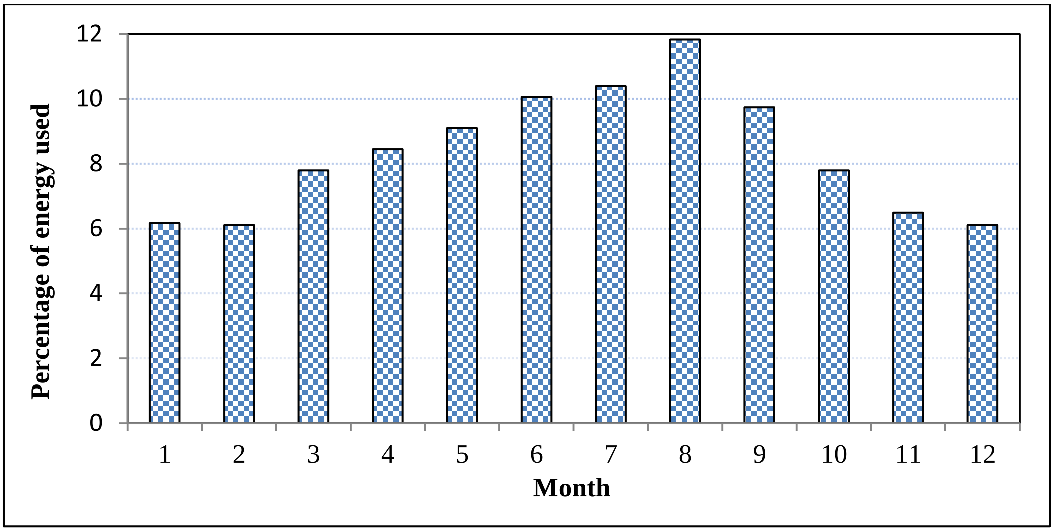

Figure 5.2 Percentage of energy consumed each month compared with the total energy consumption of all sectors in Hong Kong during 2009. Source: the Hong Kong Monthly Digest of Statistics, Census and Statistics Department.

The estimated monthly energy consumption is broken down further into daily and hourly figures by dividing it with number of days in a month and hours in a day, respectively. The estimated hourly energy consumption is multiplied by an hourly fraction to account for changes in energy consumption during the diurnal cycle. The diurnal fraction is applied only to UMTs whose energy consumption is known to be fluctuating during the diurnal cycle (see Figure 5.4). The diurnal fraction for residential, commercial and industrial sectors is based on the typical working hours (World Travel Guide, 2009) because it is assumed that the movement of the population during the diurnal cycle correlates with the energy consumption values of various UMTs. However, UMTs consume similar energy magnitudes throughout the day (without being affected by the movement of population). Therefore, they are excluded while estimating diurnal fractions. For example, a warehouse may consume energy throughout the day for heating or cooling purposes, so a fraction is not invoked while calculating the hourly energy consumption of this UMT (the warehouse).

Next, the hourly energy consumption figures are multiplied by 0.7 implying that only 70% of the estimated energy is consumed in a day, in view of the non- similarities in energy consumption of buildings.

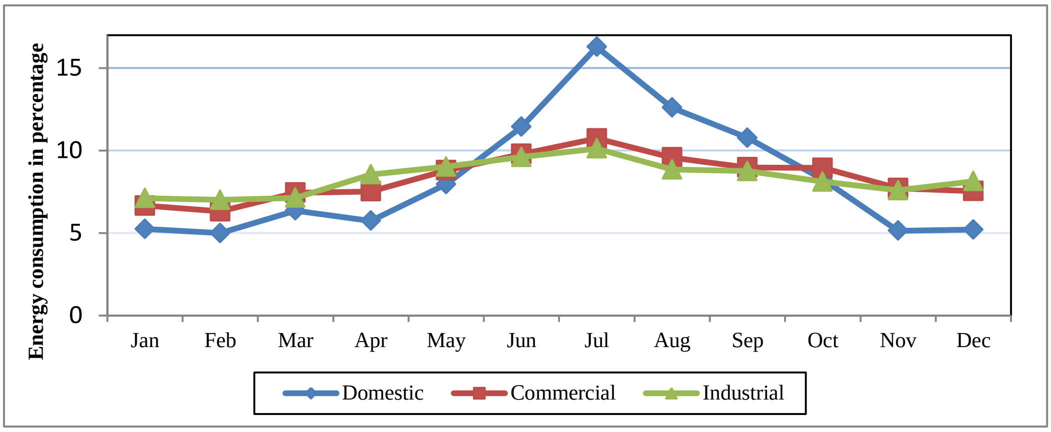

Figure 5.3 Ratios of energy consumed by different sectors in a month to the total energy consumption in 2009.

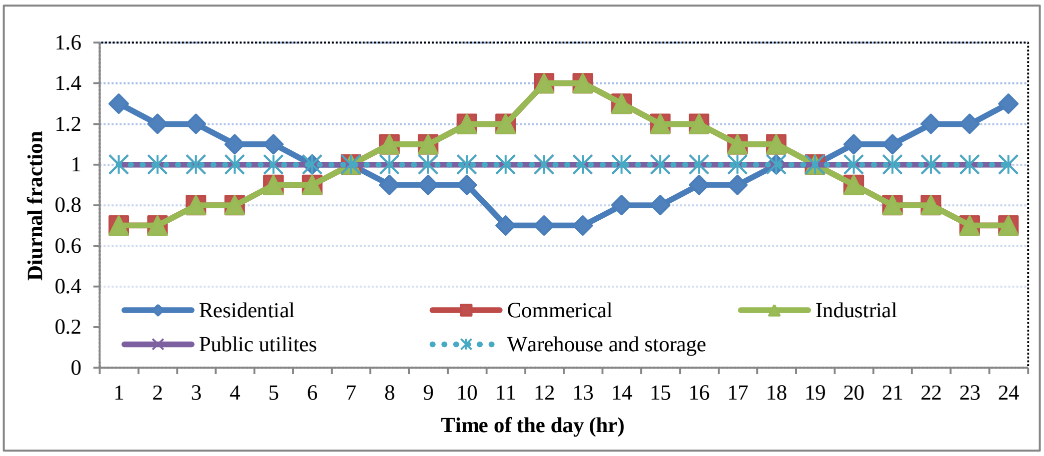

Figure 5.4 Diurnal fractions of different sectors as used while estimating hourly energy consumption magnitudes.

Figure 5.3 shows that domestic energy consumption is more sensitive to seasonal changes than commercial and industrial energy consumption. Figure 5.4 shows that the diurnal fractions of residential, commercial and industrial sectors are linked to the population flows during the diurnal cycle. The figures for public utilities and warehouses remain constant since it is assumed that their heating and cooling requirements stay the same throughout the day.

5.2.3 Vehicular heat emissions

In this study, vehicular emissions are estimated using a bottom-up approach that is in line with Smith *et al.* (2009) who had adapted earlier work by Grimmond (1992). Smith *et al.* (2009) used grids of 200 m squares to map vehicle heat emissions across Manchester by considering parameters such as road type, vehicle type and speed dependent vehicle emissions. The parameters used in the present study are similar to those used in Smith *et al.* (2009) with the exception of road types which are ignored because the speed of a vehicle on a road is a function of the road type. The road type can however be taken into account indirectly by including the vehicle speed associated with each road. This also simplifies calculations.

The vehicle emissions estimated in the present study are limited to grid cell containing roads with the other pixels being marked as ‘no-data’. The formula used to calculate vehicle emissions is

$$\boldsymbol{Q_{veh-L}} = \frac{\sum \left(\boldsymbol{n_{mx}}\,(\boldsymbol{t})\,\boldsymbol{L_x}\right)\boldsymbol{EF_m}}{\boldsymbol{A_x}} \qquad (5.5)$$

where, $Q_{veh\text{-}L}$ is the vehicle emission in Wm^{-2}, n_{mx} is the number of vehicles by type m, t is the time of the day in hours, L_x is the road length in m, EF_m is a speed-dependent fuel consumption factor expressed in Wm^{-1}, and A_x is the grid area in m^2.

The number of vehicles on each road is extracted from the annual average daily traffic (AADT) data collected in the annual traffic census (ATC) of the Transportation Department of Hong Kong (2014). AADT is based on measurements carried out at the core and at the coverage stations. The census defines core stations as “randomly selected counting stations located on a road link of any class providing hourly, daily and monthly factor to generalize the traffic characteristics for its own group links”, and a coverage station as “a counting station located on a road link of any class providing daily flow that will be factored by the corresponding scaling factor of the group to which it belongs, to give the AADT." Data collected at the core stations are also used for constructing scaling factors and for estimating AADT. For illustrative purposes, Table 5.2 shows the figures for the core station, Hong

Kong Island Urban 1. The figures were estimated by using 11 different scaling factors for different regions in Hong Kong: 4 region for Hong Kong Island, 3 region for Kowloon, and 4 region for New Territories.

Table 5.2 Group Scaling Factors for Hong Kong Island Urban region1 for the year 2010.

Month\Day	Sun.	Mon.	Tue.	Wed.	Thu.	Fri.	Sat.
January	1.176	0.981	0.952	0.956	0.944	0.917	0.980
February	1.197	0.978	0.946	0.947	0.941	0.926	0.983
March	1.189	0.976	0.950	0.944	0.936	0.928	0.986
April	1.190	0.974	0.957	0.942	0.951	0.922	0.984
May	1.187	0.981	0.949	0.954	0.936	0.934	0.987
June	1.185	0.987	0.968	0.975	0.956	0.940	0.998
July	1.221	1.007	0.982	0.981	0.971	0.951	1.003
August	1.202	1.005	0.993	0.972	0.972	0.961	1.012
September	1.200	1.000	0.975	0.966	0.961	0.939	1.018
October	1.197	0.991	0.974	0.962	0.949	0.944	0.997
November	1.173	0.977	0.961	0.956	0.949	0.940	0.989
December	1.166	0.981	0.959	0.947	0.939	0.930	0.977

Source: The annual traffic census, Transport Department (2013)

The AADT figure for each coverage station is obtained by multiplying the observed short-period count of the station by a group scaling factor for the given day of the week and month of the year (Transport Department, 2013). For example, the daily and hourly vehicle flows are recorded at the core station (A) for the duration of one week in each of any three months (directional) and one week in each of the remaining nine months in the year (non-directional). Similarly, other core stations have their own recording periods. The core and coverage stations comprise both the major and minor roads of Hong Kong.

The hourly vehicle flow corresponding to each vehicle class is extracted from the AADT value of each station as recorded over a 16 hour period (07 am to 11 pm) in the day. The traffic flow figures associated with the image overpass times are extracted for all the major roads. The overpass times of ASTER during the day (11 am) and the night (11 pm) are at off-peak hours of traffic. The peak hours on the roads vary based on their locations. However, the overall peak hours on roads in

Hong Kong lie between 6 and 10 am during the morning and from 7 to 10 pm in the evening.

The number of vehicles of different types on each road at a particular time and the speeds at which they travel are used to calculate the speed dependent emission factors. The emission factor for a vehicle at a different speed is calculated from the corresponding 'Emission Factor' taken from the Environmental Protection Department (2014) of Hong Kong. The Environment Protection Department has built software called Emissions Fraction (EMFAC) which is used here to quantify pollutants based on vehicle speed and type.

The vehicle types used in EMFAC are motorcycles, private cars, taxis, buses, goods vehicles, public light buses, private light buses, and government vehicles. EMFAC calculates the average emissions of each vehicle class at different speeds. The average of each factor for each vehicle class is determined in EMFAC by considering the number of vehicles of each type, age, vehicle kilometres, engine type, efficiency, and speed. The EMFAC allows the user to model the average emission of each vehicle class based on the traffic flow of a year or traffic data of several years. In this study, the traffic flow of each year is taken into account while estimating hourly emissions.

In view of the lack of traffic details related to minor roads, emission calculations are limited only to vehicles on major roads. Smith *et al.* (2009) assume a uniform daily flow with an AADT of 1,700 for minor roads, which yielded considerable overestimates of flows on the majority of minor roads within the city, but could still be taken to be representative of the city as a whole. In our model, a different method is used by assuming that the emissions from a minor road are proportionate to those from a major road within the comprehensive transport study (CTS) zones of the planning department. To arrive at the emission figure for a minor road, a fraction (0.1) is applied with respect to the mean emission of a major road within the CTS zone at a specified time. The following equation captures the estimation process.

$$EM_{\mathrm{minor}} = \mathrm{Average}\,(EM_{\mathrm{major}}\ (z)\,(t)) \times 0.1 \qquad (5.6)$$

where, EM_{minor} is the emission from the minor road, z is the zone corresponding to the minor road, EM_{major} is the emission from a major road within zone z at time t (hours).

The emissions from minor and major roads are then added together to yield $Q_{veh\text{-}L}$:

$$EM_{\mathrm{major}} + EM_{\mathrm{minor}} = Q_{veh\text{-}L} \qquad (\mathrm{Wm}^{-2}) \qquad (5.7)$$

Table 5.3 Populations of vehicles of different fuel types in 2007.

Hong Kong SAR Population by Vehicle/Fuel	**Petrol**	**Diesel**	**LPG**
Private Cars (PC)	371,562	1.810	0
Taxi	0	0	18,164
Light Goods Vehicles <=2.5t	294	1,312	0
Light Goods Vehicles are 2.5-3t	1,730	39,813	0
Light Goods Vehicles>3.5t	0	26,603	0
Medium and Heavy Goods Vehicles	0	10,720	0
Medium and Heavy Goods Vehicles	0	31,423	0
Public Light Buses	0	1,855	2,495
Private Light Buses <=3.5t	2,383	494	0
Private Light Buses >3.5t	196	1,326	423
Non-franchised Buses<=6.4t	0	3,364	0
Non-franchised Buses 6.4-15t	0	2,697	0
Non-franchised Buses >15t	0	1,830	0
Franchised Buses (SD)	0	369	0
Franchised Buses (DD)	0	5,522	0
Motorcycles (MC)	38,370	0	0

Source: The EMFAC, Environment and Protection Department (2013)

5.3 Results and discussion

As in LUCY-HK, the model outputs are stored as 100 m grid cell. This helps improve the scale of output resolution because the information used for emission estimation is measured from individual roads and buildings. This also provides the finest possible measurement and, hence, allows the model to trim down the grid size to 10 m or smaller. However, the output resolution is fixed as 100 m grids in order to compare the results with those from other GIS and remote sensing models. The model also accounts for sources of anthropogenic emissions except for those arising from aviation, maritime, and industrial discharges. Since the present work is limited to the urban areas of Hong Kong, it is assumed that the main contributors are buildings, vehicles and humans.

Anthropogenic heat and its components are measured for a summer day (22nd August 2009, at 11 am) and a summer night (17th September 2009, at 11 pm). These days were selected because they were the hottest days in the corresponding months. The weather on these days was typical of Hong Kong at 11 am and 11 pm of that year. Details of seasonal and diurnal variations are discussed in Chapter 6.

5.3.1 Metabolic heat

The metabolic heat emissions calculated from the integrated population dataset across Hong Kong range from 0 Wm^{-2} to 47 Wm^{-2} during the summer day 22nd August 2009, at 11 am. As for summer nights, they range from 0 Wm^{-2} to 19 Wm^{-2}. The daytime emissions are higher due to the inflow of population to the workplace during the modelling period. During daytime, a maximum emission of 47 Wm^{-2} was observed over the business and commercial districts of Central-Western district, while at night, the maximum emission observed was 10 Wm^{-2} over the Sham Shui Po residential area.

The overall mean emissions were found to be 4.7 Wm^{-1} and 4.2 Wm^{-1} during the day and night, respectively. The standard deviation values of 4.6 (day) and 3.0 (night) for that dates suggested a greater variation in daytime emission from the mean.

Because of the larger number of people engaged in commercial and business related activities at 11 am, higher metabolic emissions were observed over the commercial and business districts of Hong Kong. Conversely, at night (11 pm), the maximum emission figures were observed over tall residential buildings, because of the huge population density of residential buildings. Figures 5.5 and 5.6 show the metabolic heat emissions over Hong Kong at 11am (22nd Aug 09) and 1pm (17th Sep 09), respectively.

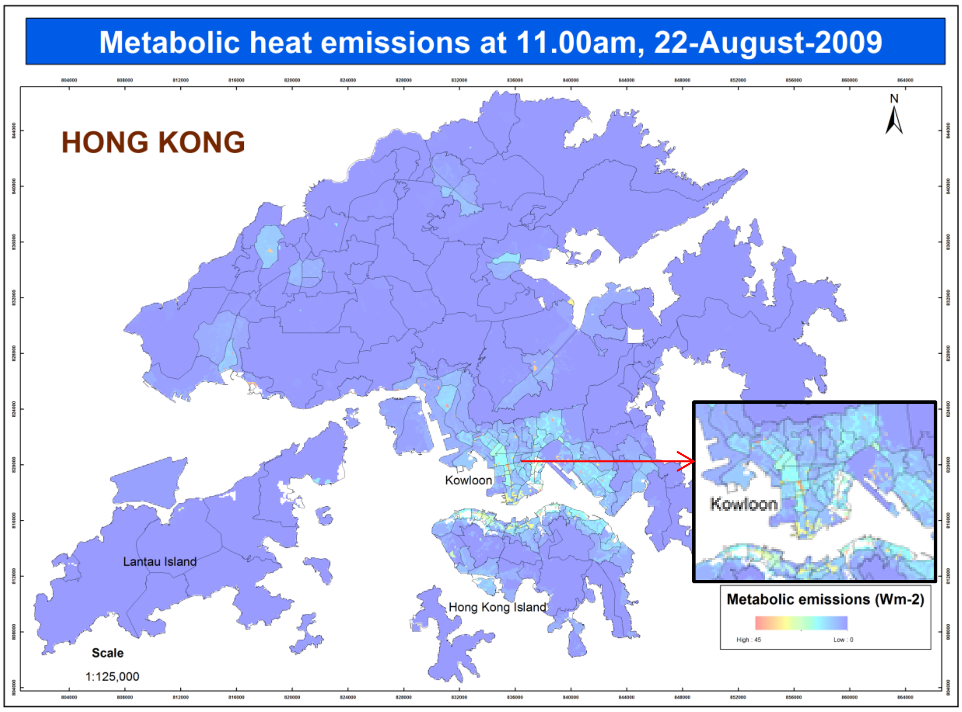

Figure 5.5 Metabolic heat emissions ($Q_{met\text{-}L}$) during daytime on 22nd August 2009 (a summer day) at 11 am.

It should be possible to estimate metabolic emissions at finer scales population datasets of each building become available along with the number of people travelling on a vehicle during transition hours. Details of the spatial relationships of metabolic heat emissions with parameters representing urban morphology will be discussed in Chapter 6. The night time metabolic emission is highly influenced by the census population, therefore the anthropogenic heat emissions were calculated at TPU level. Meanwhile daytime estimations are based on integrated population in which spatial variation is well accounted.

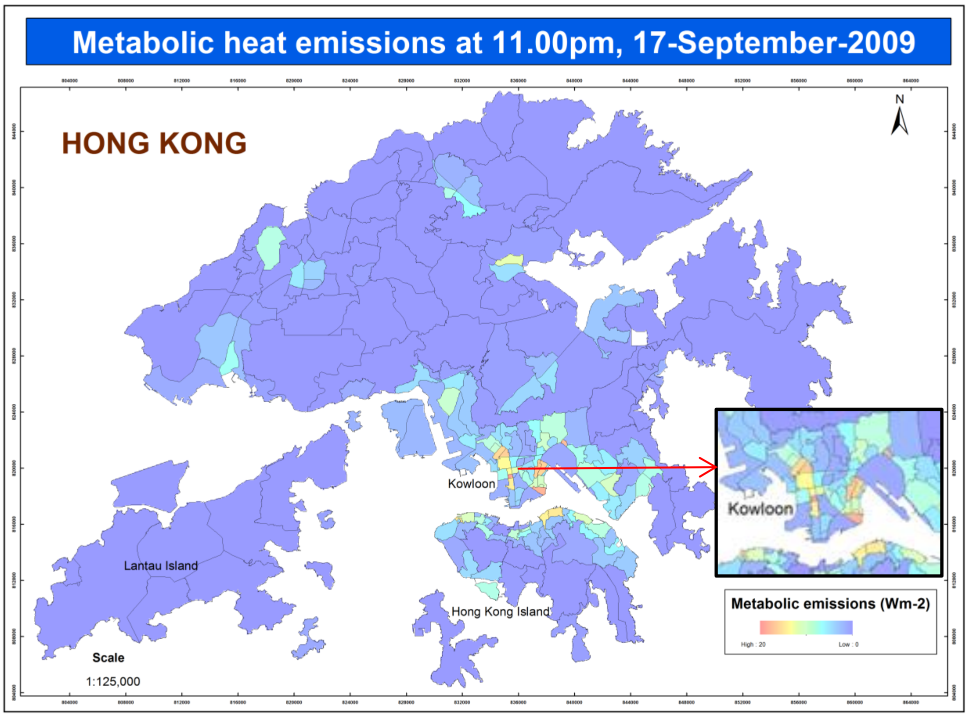

Figure 5.6 Metabolic heat emissions ($Q_{met\text{-}L}$) during the night of 17th September 2009 (a summer night) at 11 pm.

5.3.2 Vehicle heat

Emissions due to vehicle exhaust ranged between 0.1 Wm^{-2} on minor roads, and 210 Wm^{-2} on urban primary distributor during the day of 22nd August 2009 (Figure 5.7). During the night of 17th September 2009 (see Figure 5.8), it was between 0.1 Wm^{-2} and 168 Wm^{-2} and the mean vehicle emissions were 3.53 Wm^{-2} and 2.82 Wm^{-2} respectively. Urban primary distributors and trunk roads exhibited higher emissions when compared to other road types in the city. Since the modelled periods were off-peak hours, the emissions were much lower when compared to those at the peak hours. The emission intensity of a road depends on the number of vehicles and their type. The roads of urban primary distributors showed heavy traffic flows, so they were also associated with heavy emissions.

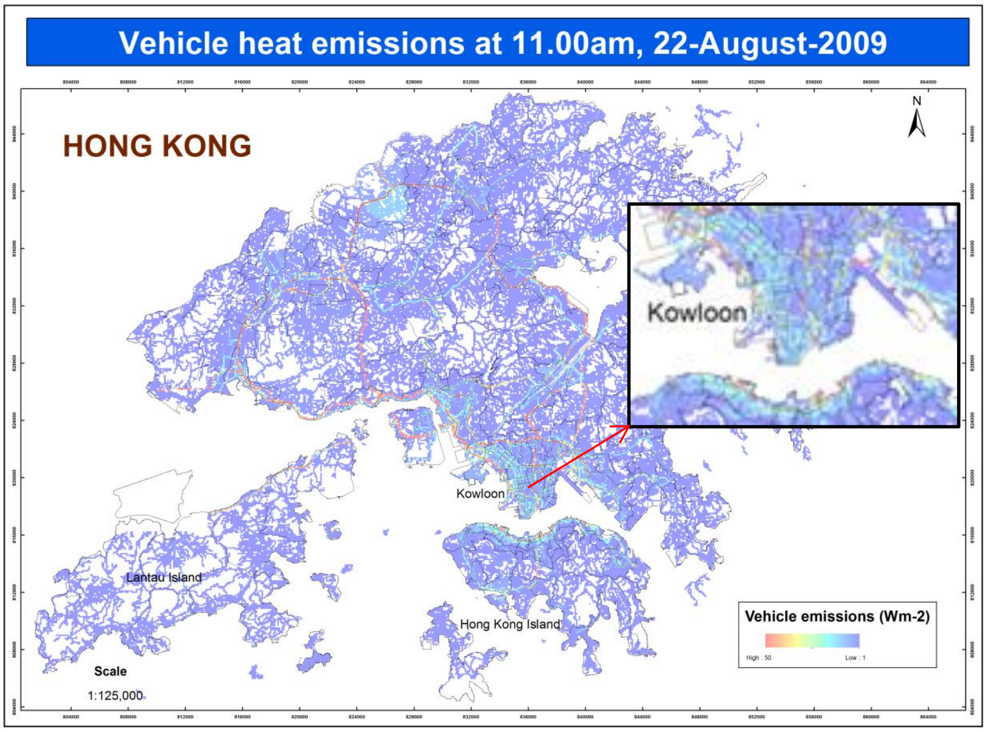

Figure 5.7 Vehicle heat emissions ($Q_{veh\text{-}L}$) during the daytime of 22nd August 2009 (summer day) at 11 am.

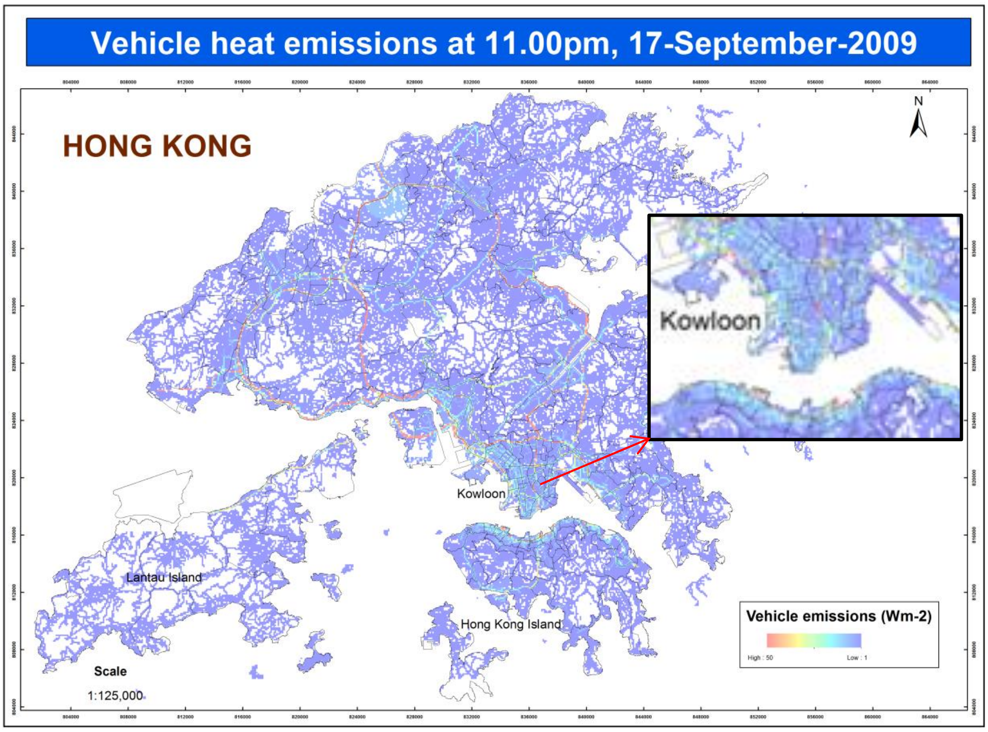

Figure 5. 8 Vehicle heat emissions ($Q_{veh\text{-}L}$) during the night of 17th September 2009 (a summer night) at 11 pm.

The average emission exhaust calculated using EMFAC is categorized into contributions due to carbon monoxide, carbon dioxide, oxides of nitrogen, volatile organic components, and total particulate matter. The quantity of pollutants which are estimated based on the fuel consumption (g/km) are transformed into heat emissions by assuming heat combustion figures of 45.85 Jkg^{-1} for petrol and 46 Jkg^{-1} for diesel. These are similar to those used by Smith *et al.* (2009). The heat combustion values for petrol range from 43 to 48 KJ g^{-1} and for diesel from 44.8 to 46 KJ g-1 (Hillier and Pittuck, 1991). The sensitivities of the fuel combustions studied by Smith *et al.* (2009) show that a 5 % change in calorific value results in changes of anthropogenic heat by 1 Wm^{-2}. Taking 1 Wm^{-2} as the nominal value, our model uses the standard calorific values for petrol and diesel.

Instead of considering the whole grid area, Smith *et al.* (2009) had restricted emissions to the areas of roads. They also tried to include the widths of different roads in the grid cell. However, restricting emissions to the road area made the emission values unrealistically large.

Since our model emissions are calculated for each hour in a day, it does not include a diurnal analysis of transport emissions. Therefore the emissions estimated, may have been underestimated, even while severe traffic congestions were being experienced. On the other hand, the model is designed to calculate possible variations from the available datasets. Further improvements are possible when detailed traffic information and finer details of traffic population become available for each hour.

5.3.3 Building heat emissions

During daytime, the building heat emissions observed are higher over the commercial downtown since energy consumptions there are higher when people are at work. The maximum values of building emissions ($Q_{bui\text{-}L}$) during the daytime (22-August-2009) at 11am ranged between 1.3 Wm^{-1} and 184.33 Wm^{-1}, while they ranged between 2.5 and 91 Wm^{-1} during the night of 17th September 2009 at 11pm. The mean values were 3.0 for daytime and 2.74 for night-time, i.e., they were similar over both the periods. The standard deviation was larger for daytime (6.84) than for night-time (4.82) due to increased energy consumption figures at work. During daytimes the highest emission were observed over the grid cells of commercial areas, while at night time they were observed over residential buildings. Rural settlements exhibited the lowest emissions throughout the day. Figures 5.9 and 5.10 show of the estimated building heat emissions at daytime and night-time, respectively.

Building emissions are calculated in the model by assuming little lag between emission and consumption. This implies that the estimates for evening emissions presented here are likely to be smaller than the actual building heat emissions (Heiple and Sailor, 2008; Smith *et al.,* 2009). It is assumed that all buildings consume energy during the design period, and there is no lag in emission. In reality, all the buildings are not active in consuming energy at any given time and there will certainly be a lag in energy release after consumption. To normalize the impacts of the above assumptions, a fraction based on energy consumption statistics for each sector is deployed in the model.

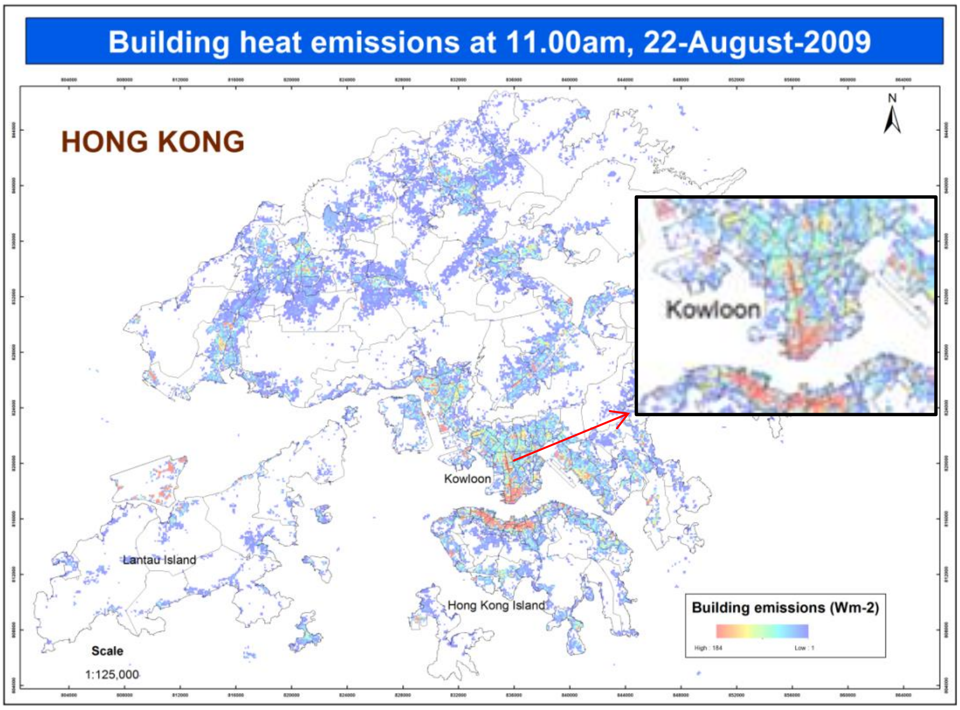

Figure 5.9 Building heat emissions (Q_{bui-L}) in the daytime of 22nd August 2009 (a summer day) at 11 am.

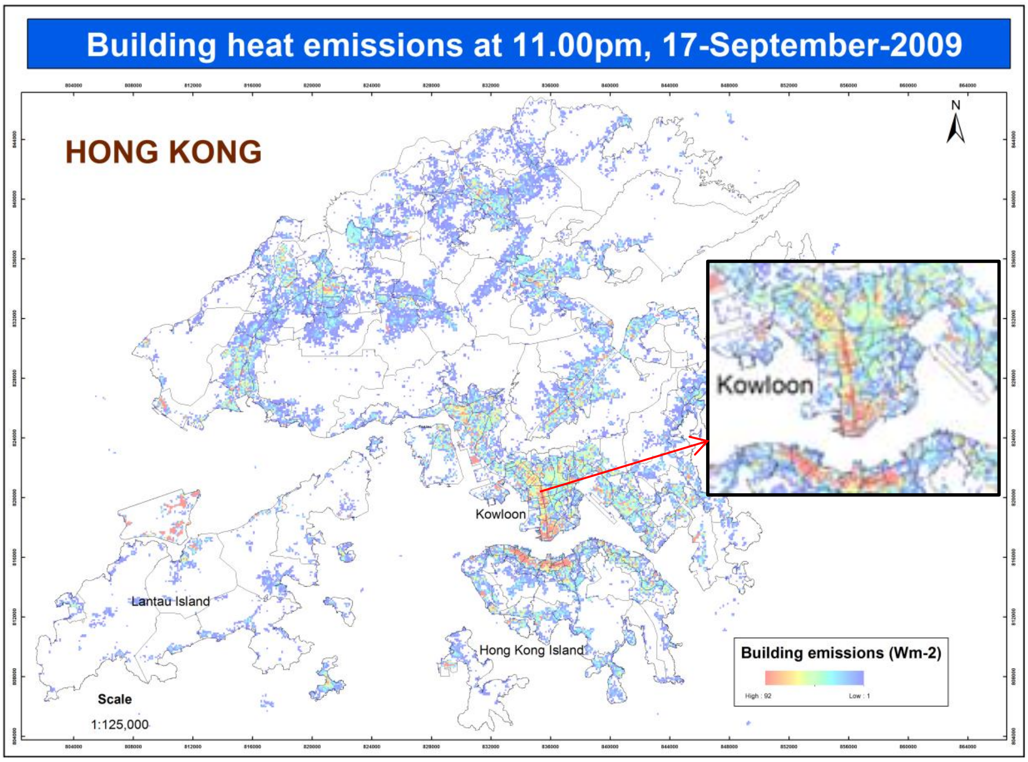

Figure 5.10 Building heat emissions (Q_{bui-L}) at night time on 17th September 2009 (in the summer night) at 11 pm.

5.3.4 Anthropogenic heat

On 22nd August 2009 at 11am, the total anthropogenic heat estimated over Hong Kong ranged between 0.004 and 224 Wm^{-2} with mean emissions of 10.6 Wm^{-2}. During the night of 17th September 2009 at 11pm, the figure ranged between 0.003 and 169 Wm^{-2} with a mean of 9.4 Wm^{-2}. The anthropogenic heat figures estimated for daytime are high when compared to night time emissions. Similar observations were made with respect to the components of anthropogenic heat. Figures 5.11 and 5.12 show anthropogenic heat flux over Hong Kong at two different periods. Although the spatial distributions are similar in the two maps, the intensities of anthropogenic heat flux vary with time. Figure 5.13 shows the frequency of emission amount by area for the two images. It may be noted that grid cells with higher emissions during daytimes remain roughly as high as those observed during night time. Grid cell with higher emission values over roads are similar in intensity during daytime to nighttimes. Urban primary distributors contribute significantly to road emissions. Commercial buildings and tall residential buildings contribute significantly to building emissions. The relationship between the estimated anthropogenic heat figures and the corresponding surface types will be discussed in Chapter 6. Chapter 6 will also compare the estimates of LUCY-HK with those from the remote sensing model.

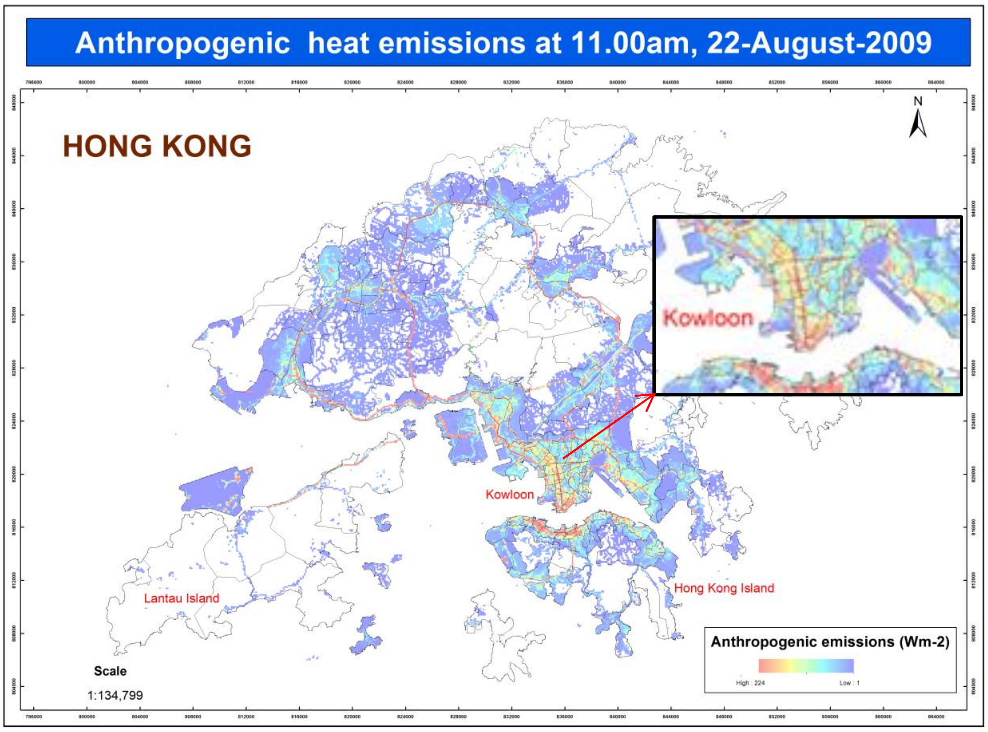

Figure 5.11 Anthropogenic heat emissions ($Q_{ahf\text{-}L}$) in the daytime on 22nd August 2009 (a summer day) at 11 am.

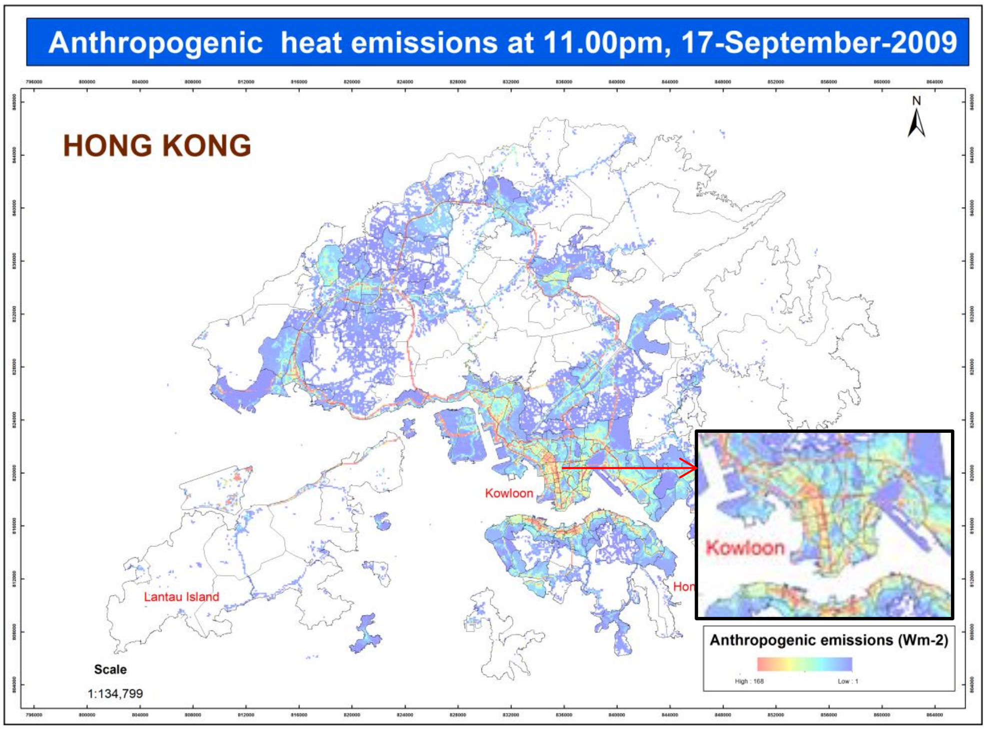

Figure 5.12 Anthropogenic heat emissions (Q_{ahf_L}) during the night-time on 17th September 2009 (a summer night) at 11 pm.

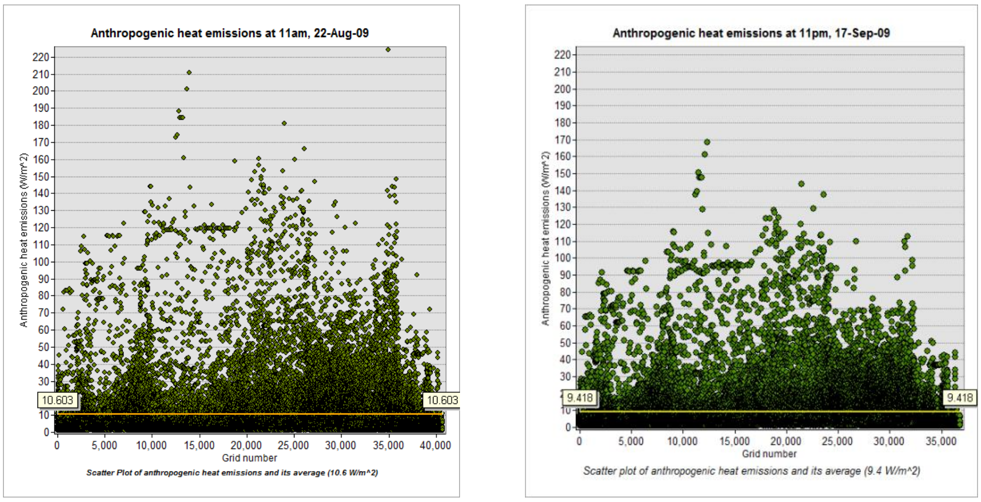

Figure 5.13 Scatter plots of anthropogenic heat emissions at each grid.

Chapter 6

OVERALL RESULTS AND DISCUSSION

6.1 Spatial analysis of anthropogenic heat flux

Tables 6.1, 6.2 and 6.3 list the spatial statistics for the anthropogenic heat flux values estimated by the three methods: remote sensing, LUCY, and GIS, respectively. The statistics take into account seasonal and the diurnal variations of anthropogenic heat over the study area. However, they are restricted to the acquisition times of the satellite images.

6.1.1 Anthropogenic heat estimated using remote sensing

As expected, anthropogenic heat values are much higher during daytime than at night. Likewise, emissions are higher during summer than in winter. Daytime emissions in commercial areas are mainly from buildings and vehicles, largely due to excessive use of air-conditioning and vehicle emission. Energy emissions from them are transformed into sensible and latent heat fluxes. Particularly high anthropogenic heat emissions are observed along Nathan road and from commercial buildings in Sham Shui Po. High nighttime emissions are observed mainly over residential areas with tall buildings. The spatial pattern of anthropogenic heat emission is not affected by seasonal changes, i.e. irrespective of the season, relatively high emission values are noted in commercial and residential areas during day and night respectively, compared to other land cover types. Although, its intensity depends on the season.

Table 6.1 shows the maximum, minimum and mean values of anthropogenic heat estimated by remote sensing for summer and winter seasons and for day and night. The intensities are high during summer with maximum value of 278 W m^{-2} on the 13 September 2008 and 250 W m^{-2} on the 22^{nd} of August 2009. Thus, when compared to the winter figure of 207 W m^{-2}. The daytime mean values of 53 and 79 W m^{-2} in summer are higher than the winter value of 11 W m^{-2}. The low mean values at night when compared to daytime are expected due to reduced activity of vehicles as well as building emissions from commercial areas.

Table 6.1 Anthropogenic heat over the Kowloon peninsula as estimated from remote sensing data

Date	Season	Period	Maximum (W m^{-2})	Minimum (W m^{-2})	Mean (W m^{-2})	SD %
31st January 07	Winter	Night	21	0	11	4
30th November 07	Winter	Day	207	0	39	30
13th August 08	Summer	Night	64	0	10	8
13th September 08	Summer	Day	278	0	53	39
22nd August 09	Summer	Day	250	0	79	36
17th September 09	Summer	Night	70	0	24	10

The standard deviation values in Table 6.1 shows higher deviation from the mean anthropogenic emission during day compared to night. This may due to increased daytime population in business and commercial districts. The lesser deviation in winter compared to summer, may due to the reduced use of air conditioners.

6.1.2 Anthropogenic heat estimated using the GIS approach

The spatial distribution of anthropogenic heat estimated by the GIS method is similar to that determined from remote sensing data. Higher emissions are observed again over commercial and business areas during the day and over residential areas with tall and dense buildings during the night. The maximum values occur on hot summer days: 198 W m^{-2} on the 13th of September 2008 and 188 W m^{-2} on the 22nd of August 2009, respectively (Table 6.2). Relatively lower intensities are experienced during summer nights: 158 and 150 W m^{-2} on the 13th of August 2008 and 17th of September 2009, respectively. The maximum values for winter are 164 and 148 W m^{-2} for daytime and night-time, respectively. The mean emission values range from 9 to 11 W m^{-2} during daytime and from 7 to 9 W m^{-2} during night-time. The model exhibits significant differences in terms of mean and maximum emission values as the season changes. Table 6.2 lists the anthropogenic heat values estimated for the entire Hong Kong. However, the mean values over the Kowloon peninsula (similar to the extent used in remote sensing estimations) are much higher than anthropogenic emission values of the entire Hong Kong. For example, the mean anthropogenic heat flux value estimated using GIS model for 13th September 2008 is 11.08 W m^{-2}, meanwhile, the value over Kowloon peninsula is 24.5 W m^{-2}. While identifying the relationships between the models, (see Section 6.2.1 for details), it is necessary to recall that the study area (the extent of satellite image used) was limited to the Kowloon Peninsula. The standard deviation values follow trend similar to the remote sensing estimation of anthropogenic heat (Section 6.1.1).

Table 6.2 Anthropogenic heat flux estimated over Hong Kong using the GIS approach

Date	Season	Period	Maximum (W m^{-2})	Minimum (W m^{-2})	Mean (W m^{-2})	SD %
31st January 07	Winter	Night	148	0	7.39	11
30th November 07	Winter	Day	164	0	9.17	14
13th August 08	Summer	Night	158	0	8.79	12
13th September 08	Summer	Day	198	0	11.08	16
22nd August 09	Summer	Day	188	0	11.06	16
17th September 09	Summer	Night	150	0	8.79	12

6.1.3 Anthropogenic heat figures estimated using LUCY

Table 6.3 shows the basic statistics associated with anthropogenic heat emissions at the image times from the LUCY model. The spatial distribution of LUCY emissions is a function of population density as well as air temperature. Anthropogenic heat values at pixels with higher daytime population densities (around 320,000 persons per square kilometer) exceed 600 W m^{-2} whereas the maximum night-time emissions are around 87 W m^{-2}. LUCY yields higher emission estimates for the winter nights than for summer nights. This is because the balance point temperature used for winter overestimates the energy required for heating. In reality, Hong Kong does not consume much energy for heating. The overestimation can however be rectified by modifying the balance point temperature used in the model while calculating the energies required for the purposes of heating and cooling. Identifying a suitable balance point by conducting field measurements is beyond the scope of this study. However, this feature is acknowledged as a limitation of this study. It may also be noted that the mean values calculated are for the entire Hong Kong whereas the anthropogenic heat values measured through remote sensing are only for the Kowloon Peninsula. The mean values for Kowloon are much higher than those estimated for the entire Hong Kong. Similar to Table 6.1 and 6.2 standard deviation values are higher in day when compared to night. However, In LUCY model the standard deviation are almost similar in both seasons, may due to the balance point value which induced overestimation (Section 6.1.3).

The spatial relationship between LUCY and the GIS-based model will be discussed in a later section.

Table 6.3. Overall anthropogenic heat values estimated by LUCY for Hong Kong

Date	Season	Period	Maximum (W m^{-2})	Minimum (W m^{-2})	Mean (W m^{-2})	SD %
31st January 07	Winter	Night	296	0.02	7.72	19
30th November 07	Winter	Day	598	0.03	9.53	27
13th August 08	Summer	Night	87	0.01	3.68	9
13th September 08	Summer	Day	655	0.03	10.46	30
22nd August 09	Summer	Day	654	0.03	10.47	30
17th September 09	Summer	Night	87	0.01	3.7	9

6.2 Spatial relationships among anthropogenic heat estimates obtained by different models

This section summarizes the spatial relationships (simple correlations) among the anthropogenic heat values estimated from the three different approaches (remote sensing, GIS, and LUCY). The grid size (100 m) and the extent (the Kowloon peninsula) are kept constant for all the output raster images used. The discussion is divided into two parts: a) comparing and evaluating the outputs from the remote sensing model with the GIS-based estimates, and b) comparing and evaluating the results from LUCY with the GIS-based estimates. The idea behind the first is to evaluate the remote sensing results against those from the field based GIS model. The idea behind the second is to evaluate the simple model (LUCY) against the GIS model. In both cases, the estimates from the GIS model are used as reference values because anthropogenic heat emission estimated by this method measures emissions directly from its source. It is built on an inventory based bottom-up approach, in which possible emission from individual buildings, vehicles and people are modelled for a given time. Therefore, the estimate of GIS method is used as a reference for evaluating the other two models.

The relationships between LUCY and satellite image based estimations are not examined since it is beyond the scope of this study.

6.2.1 Spatial relationship between the remote sensing and GIS model estimates

The anthropogenic heat values estimated by remote sensing are evaluated first against the GIS-based results. The comparison is not limited to anthropogenic heat estimations alone; the components of the energy balance equation are also compared individually with the corresponding estimations from the GIS model. Table 6.4 lists the correlation results between remote sensing images taken at different seasons and periods with the corresponding GIS-based estimates.

Table 6.4 Evaluation of remote sensing estimates of anthropogenic heat against the GIS-based estimations using a correlation (Pearson product-moment correlation coefficients) technique

Date	Period	E_{GIS} vs. E_{AHF}	E_{GIS} vs. E_{EBR}	E_{GIS} vs. E_{SH}	E_{GIS} vs. E_{LH}	E_{GIS} vs. E_{GH}	E_{GIS} vs. E_{NR}
31st January 07	Night	0.61	0.87	0.58	0.57	0.85	0.49
30th November 07	Day	0.22	0.63	0.31	0.78	0.76	0.61
13th August 08	Night	0.58	0.68	0.59	0.55	0.31	0.31
13th September 08	Day	0.31	0.73	0.34	0.90	0.94	0.94
22nd August 09	Day	0.41	0.7	0.4	0.76	0.92	0.56
17th September 09	Night	0.78	0.89	0.62	0.58	0.59	0.65

where,

E_{GIS} = Anthropogenic heat estimated using the GIS model,
E_{AHF} = Anthropogenic heat estimated using the remote sensing model,
E_{EBR} = Sum of components on the right side of the energy balance equations used in the remote sensing approach,
E_{SH} = Sensible heat flux estimated using the remote sensing approach,
E_{LH} = Latent heat flux estimated using the remote sensing approach,
E_{GH} = Ground heat flux estimated using the remote sensing approach,
E_{NR} = Net radiation heat flux estimated using the remote sensing approach.

The remote sensing method estimates anthropogenic heat emission as the imbalance between incoming energy and emitted energy values. Therefore, it is more appropriate to compare the anthropogenic heat measured using a GIS model with the emission components in the energy balance equations (sensible, latent and ground) rather than with the excess heat (anthropogenic heat). It is noted that the intensity of anthropogenic heat value estimated is not compared here, instead robustness of the remote sensing model is evaluated using the spatial distribution characteristics of the GIS model. It is found that, while the emission components show strong correlation, the anthropogenic heat figures estimated by the remote sensing method are more accurate because these are the sources of emission used to calculate residual anthropogenic heat.

The individual components (sensible heat, latent heat and ground heat) in the energy balance equation have yielded even better correlations with the anthropogenic heat figures estimated by the GIS model (see Table 6.4).

Table 6.4 lists the values of the coefficient of determination, r, between the anthropogenic heat values estimated using the remote sensing and the GIS-based methods. The maximum correlation figures relating the anthropogenic heat estimates from the two models are 0.61, 0.58, and 0.78 for the nighttime images of 31st January 2007, 13th August 2008 and 17th September 2009, respectively. The correlation is higher for the winter night (31st January 2007) than for the summer night (13th August 2008 and 17th September 2009). Lesser correlations are observed with respect to daytime anthropogenic heat estimates: the coefficients are 0.22, 0.31, 0.41 for the images of 30th November 2007, 13th September 2008, and 17th September 2009, respectively, compared to night time. This is a result of the strong influence of the energy from the sun (net radiation) on the surface materials during day time. In the GIS method, anthropogenic heat is estimated by assuming that sources emit a certain fraction of the maximum emission at a given time. i.e., energy sourced from the sun is not taken into account. For this reason, a direct comparison of the estimates of anthropogenic heat from the two models (Remote sensing and GIS based model) shows a lesser correlation during the day and higher correlation at night (in the absence of insolation). Therefore, the comparison with GIS model estimates is extended to the individual components in the energy balance (sensible, latent, ground heat, and net radiation) equations. Summed figures of sensible, latent and ground heat fluxes are equivalent to the estimates from the GIS approach, in which vehicle, building and human emissions are released in the form of the three component heat fluxes but neglecting the impacts of incoming solar radiation.

Table 6.5 Correlation and Covariance matrix value of remote sensing and GIS based estimations of anthropogenic heat.

Date	**Period**	**Correlation r**	**Covariance σ**	**Variance RS**	**Variance GIS**
31st January 07	Night	0.61	11.1	87	10
30th November 07	Day	0.22	82.9	615	215
13th August 08	Night	0.58	13.9	144	42
13th September 08	Day	0.31	194	1061	264
22nd August 09	Day	0.41	270	1499	292
17th September 09	Night	0.78	34.8	156	12

The correlation matrix and covariance matrix values are tabulated (Table 6.5) to show the spatial distribution characteristics of two models. The positive covariance value suggests that greater emission values of remote sensing method correspond with the emission values of the GIS model and the same holds for the smaller values. The covariance values of the daytime emission are much higher than the night. This is because of has higher anthropogenic heat intensity observed during the day in both the models, at similar locations. Moreover, at night the intensity reduces. High variance value (1061, 1499 and 615 of 13th September 08, 22nd August 09, and 30th November 07 respectively) during days in remote sensing estimation shows the emission values are spread out much from the mean value when compared to GIS model values (264, 292 and 215 of 13th September 08, 22nd August 09, and 30th November 07 respectively). At night, the anthropogenic heat emission distribution is less scattered, however the intensities are subjected to seasonal variations.

6.2.2. Spatial relationship between the GIS and the LUCY model

Table 6.6 lists the correlation results from the GIS-based estimation and LUCY model.

Table 6.6 Correlation between GIS and LUCY models

Date	Season	Period	Correlation	Covariance	Variance LUCY	Variance GIS
31st January 07	Winter	Night	0.85	39	183	12
30th November 07	Winter	Day	0.85	70	352	20
13th August 08	Summer	Night	0.89	21	41	14
13th September 08	Summer	Day	0.85	87	423	25
22nd August 09	Summer	Day	0.87	92	423	27
17th September 09	Summer	Night	0.89	21	41	15

It is seen from Table 6.6 that there is a high correlation between GIS and LUCY models in all seasons. At nights, the correlation values are slightly higher than the days. The LUCY's Variance values show that the range of emission values is much spread out compared to GIS model. Meanwhile, GIS model emission values are closer to the mean. The positive covariance in the images suggests that the spatial distribution of anthropogenic emission values is relative to each other. The statistical values in Table 6.6 indicate that the downscaled LUCY (LUCY-HK) estimation is at once reasonable and reliable. Therefore, it may be concluded that LUCY is not just a low-resolution anthropogenic heat model; it can also be used at finer city scales. Compared to other models, LUCY-HK requires fewer input data sets, so it is simpler to use. It is also capable of modelling and predicting anthropogenic heat values for each hour in the diurnal cycle. Furthermore, it can also estimate and calculate anthropogenic heat statistics for a complete season or even a full year.

6.3 Spatial relationship between emission estimates from remote sensing and those from urban morphometric parameters

Summations of sensible, latent and ground heat fluxes (E_{EBR}) are correlated with estimated urban morphometric parameters such as frontal area index, λ_F, the plane area index. λ_P, and air temperature, T_{air}, obtained from remote sensing. Note that the last parameter represents urban heat island intensity. The frontal area index is taken from Wong *et al.,* (2013), Plane area index is calculated in the study using a 3-Dimension building GIS dataset. Table 6.7 lists the overall correlation values. The frontal area index and plane area index of Kowloon Peninsula are shown in Figure 6.1 and 6.2.

Table 6.7 Correlation (R) between E_{EBR} (right side component in energy balance equation i.e. sensible, latent and ground heat) heat emissions estimated from remote sensing and values of urban morphometric parameters

Date	Season	Period	E_{EBR} vs. λ_F	E_{EBR} vs. λ_P	E_{EBR} VS T_{air}
13-Aug-08	Summer	Night	0.32	0.36	0.53
13-Sep-08	Summer	Day	0.41	0.30	0.19
31-Jan-07	Winter	Night	0.46	0.41	0.60
30-Nov-07	Winter	Day	0.21	0.34	0.48

Table 6.7 shows a moderate relationship between the estimates from remote sensing and those from the morphological parameters as derived from daytime and nighttime images of winter and summer seasons. The correlation coefficient is better between λ_F and E_{EBR} at night compared to daytime. Similarly, the λ_P has a better correlation at nights compared to daytime in all seasons. The highest correlation between E_{EBR} and two morphological parameters (λ_F and λ_P) were observed in a winter image (31st January 07) among the four images (Table 6.7). As expected, the air temperature has a better

correlation at night compared to day in both the seasons. The positive correlation suggests that a rise in any of these parameters (i.e. Frontal area index, Plane area index , and air temperature estimated using thermal satellite images) will increase emissions in the form of sensible, latent and ground heat fluxes. Therfore, it is necessary to estimate these parameters carefully for accurate estimation of anthropogneic heat.

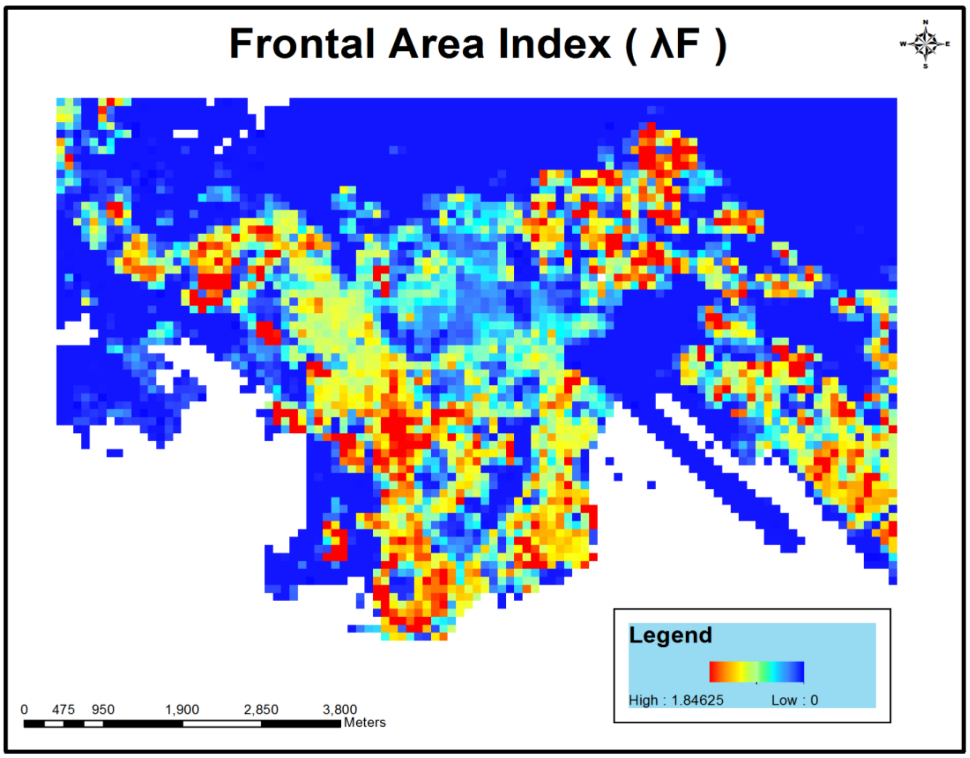

Figure 6.1 Frontal area index of Kowloon Peninsula (Wong *et al.*, 2013) at 100 m spatial resolution

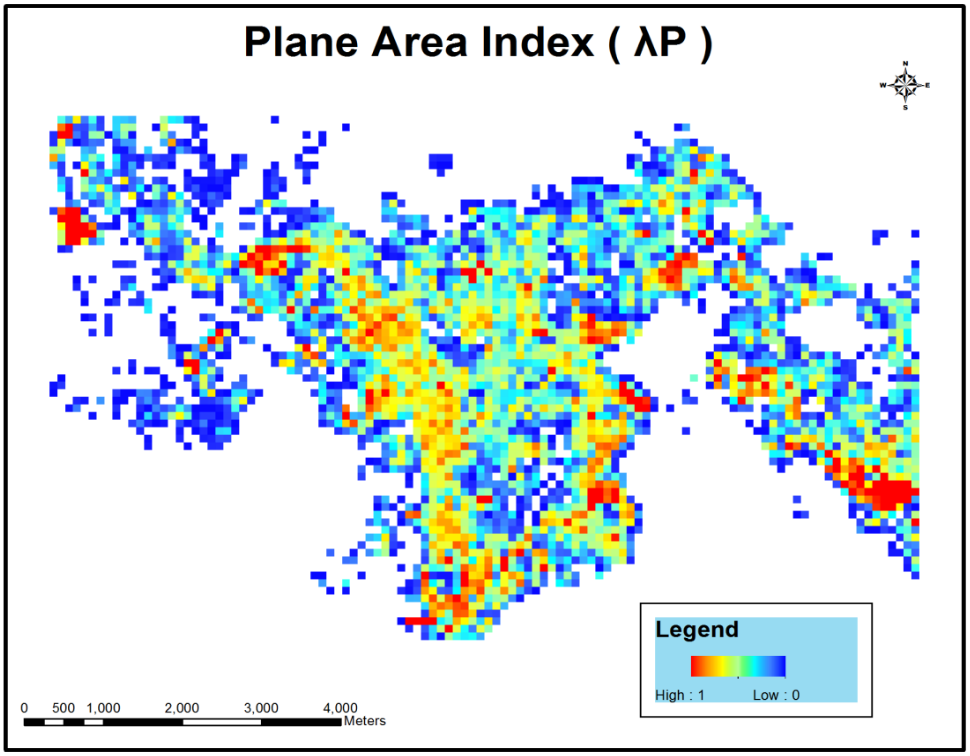

Figure 6.2 Plane area index of Kowloon Peninsula at 100 m spatial resolution

Chapter 7

CONCLUSION AND SUGGESTIONS

The three models (Remote sensing, GIS and LUCY based models) developed in this study are capable of mapping anthropogenic heat at high spatial and temporal resolutions. However, each model has its own advantages and limitations.

The remote sensing approach enables the estimation of surface heat fluxes at a spatial resolution of 30 m. This is the first time such a fine resolution has been achieved from Thermal remote sensing images. The remote sensing approach accounts for spatial variations in anthropogenic emission much better than the other two methods. It takes into account emissions from all possible sources at a given time in the form of sensible, latent and ground heat fluxes. However, there are difficulties with respect to obtaining cloud-free images over Hong Kong. A new emissivity technique (reflectance-based method) developed in this study maps surface temperature at a spatial resolution of 30 m. The method is simple and useful for other applications depending on surface emissivity. The atmospheric correction method used here demonstrates the need for defining atmospheric conditions locally in the calculation albedo and net radiation. The remote sensing based estimation can be further improved by measuring ground heat separately. It is noted that the method used in this study considers ground heat as a fraction of net radiation. Though the remote sensing model is more complicated to build, than the other two models used, it has the advantage of mapping anthropogenic heat more precisely.

Some additional benefits of the remote sensing approach, and how it can be used effectively are listed below

- The remote sensing approach does not require many assumptions when compared to other methods which require several assumptions regarding energy consumption and emission.
- The remote sensing method precisely maps all emissions for the given extent, but other approaches do not include emission for all sources. Most inventory approaches includes emission only from buildings, vehicles and human beings.
- The remote sensing method estimates anthropogenic heat in real time, and the lag between energy consumption and its emission is indirectly accounted.
- The energy balance components (Sensible, latent and ground heat) are measured individually, which helps to identify the characteristics of anthropogenic heat emission sources.
- The remote sensing approach can be simplified if roughness parameters are estimated using LIDAR techniques.
- Remote sensing images cover a larger area and are less expensive compared to inventory approaches which require intense data collection in the field, followed by complex computations.
- The remote sensing algorithm can be directly used in other cities with similar climatic conditions upon changing the input roughness parameters, whereas other approaches require serious modifications in the model.

The remote sensing method a few limitations which are listed below,

- It is difficult to account for hourly variations of anthropogenic heat emission using this approach since the temporal resolution of the satellites is low.
- Obtaining cloud free images is a challenge.
- It is difficult to validate because it requires instruments like EBBR (Energy Balance Bowen Ratio method) and ECOR (Eddy Correlation flux measurement system). The individual components of the energy balance system, i.e. Net radiation (net broadband total irradiance), Sensible heat (heat exchanges when temperature changes), Latent heat (heat exchanges during phase change) and

Ground heat (thermal conductivity of the surface) are measured using the above instruments. Setting up instruments requires large towers that are expensive. The spatial coverage of the instrument is small and it can only be used to validate a small part of the remote sensing image but not the whole extent.

- It can be validated if real-time energy consumption of buildings and vehicles are available, but these are difficult to obtain.

The GIS-based model maps anthropogenic heat using high-resolution spatial data sets. The GIS method is also efficient for mapping anthropogenic heat at the building scale, and it is better when compared to the LUCY model. It considers only the emissions from buildings, vehicles, and human beings and does not take into account those from industrial and other sources. The GIS model considers the building emission at three dimensions while previous studies are limited to two-dimensional estimation. Results of GIS model can be further improved, upon availability of the exact energy consumption of buildings and vehicles. The GIS model is capable of estimating anthropogenic heat at micro scale (at the building level), which is not possible with the other two models.

The other model, LUCY, is based on simple data sets consisting of population densities and air temperatures. The original version of LUCY was downscaled in the present study and customized to suit Hong Kong. Results from the revised version (LUCY- HK) have shown a high correlation with estimates from the GIS model for all seasons. This confirms that the spatial distribution characteristics of LUCY and the GIS model are almost similar. The LUCY can be used to map anthropogenic heat at any hour of the day. It calculates hourly statistics of anthropogenic heat and its components for a whole modelled period. This period can be hours, months or years. However, in this study anthropogenic heat estimation is limited to satellite overpass time. The LUCY enables one to identify hourly and seasonal variations in anthropogenic heat emissions using the simple computational method. However, a limitation is that, since it mainly depends on population density, all the other parameters are calculated based on that. This approach may not adequately account for realistic spatial distributions of anthropogenic heat.

Thus not be so accurate for mapping at finer scales. In addition, the temperature scheme used is based on monthly variations in temperature, which may not be able to capture daily variations adequately. Therefore, a new temperature scheme needs to be used so as to improve the estimation of anthropogenic heat emissions. However, not withstanding these limitations, it remains a very useful method for calculating of anthropogenic heat for longer periods. This is not possible with the other two models studied.

The anthropogenic heat values estimated by all the three models utilized or developed in this study have revealed higher emissions in Hong Kong during daytime compared to night. Similarly, the intensity is observed to be higher during the day than night. Compared to other regions of Hong Kong, a higher level of anthropogenic activity is seen over the Kowloon Peninsula and in parts of Hong Kong Island. At night, the tall residential towns in New Territories also exhibit higher heat emissions. On the Kowloon peninsula, the Sham Shui Po district showd particularly high anthropogenic heat emissions irrespective of the season, while high intensities are observed in the shopping and commercial districts of Nathan Road. Overall, the results from all the three models show that commercial areas are prone to higher anthropogenic heat emissions during the day while residential areas have higher night-time emissions. The correlation coefficient values between remote sensing and GIS based methods, evaluates robustness of the remote sensing model using spatial distribution characteristics of the GIS model. The high correlation between GIS and LUCY models evaluates the spatial distribution of the LUCY model with the spatial distribution characteristics of the GIS model. However, it is to remember that LUCY can be accurate only at certain resolutions.

To summarize, ASTER images have been used in this study for the purpose of estimating anthropogenic heat at high spatial and temporal resolutions. The results have been evaluated using the spatial distribution character of the high-resolution GIS model and the simplified LUCY model, both customized for Hong Kong.

The study has identified hotspots of anthropogenic heat emissions in Kowloon peninsula using the remote sensing model, and studied the same for the entire extent of Hong

Kong using the other two models. In addition, the spatial relationship between the anthropogenic heat measured using remote sensing, and the urban heat island (UHI), morphometric parameters (frontal area index, plane area index) have been studied. Seasonal and diurnal variation in anthropogenic heat emission is studied.

The outputs of the models should be very useful for researchers engaged in heat-related and environmental studies. The results can be incorporated as inputs in new climate models. The maps produced here should be particularly helpful to government agencies in planning a better urban environment. It may help to mitigate UHI effectively by minimizing anthropogenic heat contribution to the intensity of UHI. The methods developed here can be applied to any city with an urban environment similar to that of Hong Kong.

The models described in this thesis have been tailor-made for the conditions of Hong Kong and the resources available. Although each of the models developed is unique in its way, they can integrate into an overall model capable of estimating anthropogenic heat in a manner clarifying distributions in space and time.

The study has some limitations that are left to the future perspective of the research

- The intensity of anthropogenic heat estimated using all three approaches has not been validated using ground measurements due to lack of instruments in Hong Kong.
- The surface temperature determined using a new emissivity technique used only 10 points for validation. Since the field measurements were conducted earlier, and limited to a few locations.
- A remote sensing study conducted only in the part of Hong Kong, i.e. Kowloon peninsula, because Kowloon remains cloud free area for the whole model period. However, the other two models (GIS and LUCY model) estimate emission values for the whole extent of Hong Kong. Therefore it was unable to discuss the spatial relationship of models estimate for the entire Hong Kong.

- Only six remote sensing images and corresponding GIS and LUCY estimates are used to represent seasonal and diurnal variations. The results can be more accurate if several images used.
- The outputs of all these models are restricted to a resolution of 100 m in order to compare results with each other. A moderate spatial correlation between the model estimations is observed.
- Present-day models of anthropogenic heat fluxes are based on data sets that are more representative of the past, rather than the present or future state of city energy systems. However, many of these data sets are regularly updated making it possible to model representations of energy systems to capture the influence of those systems on heat fluxes. For instance, the remote sensing approach can be used to locate energy hotspots that can be related to the anthropogenic activity of any city at a given time. Combining such data into the numerical models will provide high accurate results of anthropogenic heat flux estimation. Integrating all three approaches might also be helpful to predict anthropogenic heat emissions of Hong Kong.

REFERENCES

Abrams, M. (2001). ASTER User Handbook. Version 2. Jet Propulsion Laboratory, 4800 Oak Grove Drive, Pasadena, CA.

Allen, R.G., Pereira, L.S., Raes, D., & Smith, M. (1998). Crop Evapotranspiration Guidelines for Computing Crop Water Requirements. Food and Agriculture Organization, Rome, Italy.

Allen, L., Lindberg, F., & Grimmond, C.S.B. (2011). Global to city scale urban anthropogenic heat flux: model and variability. International Journal of Climatology, 31, 1990-2005.

Amato, A.D., Ruth, M., Kirshen, P., & Horwitz, J. (2005). Regional energy demand responses to climate change: Methodology and application to the commonwealth of Massachusetts. Climatic Change, 71, 175-201.

Anthes, R.A. *(*1990). Recent applications of the Penn State/NCAR mesoscale model to synoptic, mesoscale, and climate studies. Bulletin of the American Meteorological Society *71*, 1610–1629.

Artis, D.A., & Carnahan, W.H. (1982). Survey of emissivity variability in thermography of urban areas. *Remote Sensing of Environment*, *12,* 313-329.

Brutsaert, W. (1982). Evaporation into the Atmosphere. D. Reidel, Norwell, Publishing company, Holland.

Carr, S.B. (2005). The Aerosol Models in MODTRAN: Incorporating Selected Measurements from Northern Australia, Retrieved *12th August 2013.*

Carlson, T.,N., & Boland, F.,E. (1978). Analysis of Urban-Rural Canopy Using a Surface Heat Flux/Temperature Model. *Journal of Applied Meteorology*, *17,* 998-1013.

Census and Statistics Department (2013). Population statistics, Hong Kong: Census and Statistics Department: Available from: http://www.censtatd.gov.hk/hong_kong_statistics/, Accessed January, 23rd, 2013.

Census and Statistics Department (2014). Hong Kong Energy Statistics, Annual Report. Hong Kong: Census and Statistics Department: Available from: http://www.censtatd.gov.hk/hong_kong_statistics/ , Accessed April, 3rd, 2014.

Chander, G., Markham, B.L., & Helder, D.L. (2009). Summary of current radiometric calibration coefficients for Landsat MSS, TM, ETM+, and EO-1 ALI sensors. *Remote Sensing of Environment*, *113,* 893-903.

Clothier, B.E., Clawson, K.L., Pinter Jr., P.J., Moran, M.S., Reginato, R.J., & Jackson, R.D. (1986). Estimation of soil heat flux from net radiation during the growth of alfalfa. *Agricultural and Forest Meteorology, 37*, 319-329.

Coppin, P.R., & Bauer, M.E. (1994). Processing of multitemporal Landsat TM imagery to optimize extraction of forest cover change features. *IEEE Transactions on Geoscience and Remote Sensing, 32*, 918-927.

Dupont, S., *&* Mestayer P.G. *(*2006)*.* Parameterization of the urban energy budget with the sub mesoscale soil model*.* Journal of Applied Meteorology and Climatology 45*:* 1744–1765*.*

Dyer, A.J. (1974). A review of flux-profile relationships. *Boundary-Layer Meteorology, 7*, 363-372

EIA. (2013). International Energy Statistics: Total Primary Energy Consumption. [Online]. Available from: http://tonto.eia.doe.gov/cfapps/ipdbproject/IEDIndex3.cfm?tid = 44&pid = 44&aid = 2, Accessed January, 30th, 2013.

Eiker, U. (2009). Low Energy Cooling for Sustainable Buildings. John Wiley & Sons Ltd, Chichester, UK (2009) p. 264.

Electrical and Mechanical Services Department (EMSD) (2013). *Energy Consumption Indicators and Benchmarking Tools* [online]. Available from: http://www.emsd.gov.hk/emsd/eng/pee/ecib.shtml, Accessed January, 23rd, 2013.

Electrical and Mechanical Services Department (E&MSD) (2014). Energy land Land: Energy uses in Hong Kong [online]. Available from: http://www.energyland.emsd.gov.hk/en/energy/energy_use/energy_scene.html, Accessed March, 20th, 2014.

Environmental Protection Department (EPD) (2014).: EMFAC- HK Vehicle emission calculation [online]. Available from: http://www.epd.gov.hk/epd/english/environmentinhk/air/guide_ref/emfac.html, Accessed January, 23rd, 2014.

Flanner, M.G. (2009). Integrating anthropogenic heat flux with global climate models. Geophysical Research Letters, 36.

Fung, W.Y., Lam, K.S., Ginn, E.W.L., & Chan, Y.W. (August 2011). Net radiation, and albedo study at Ta Kwu Ling. *Hong Kong Meteorological Society Bulletin* (2009),*19*. Reprint 978, August 2011.

Gillespie, A., Rokugawa, S., Matsunaga, T., Cothern, J.S., Hook, S., & Kahle, A.B. (1998). A temperature and emissivity separation algorithm for Advanced Spaceborne Thermal Emission and Reflection Radiometer (ASTER) images. *IEEE Transactions on Geoscience and Remote Sensing, 36*, 1113-1126.

Ginn, E.W.L., Tai, S.C., Lee, O., Ho, K.L., Chow, C.H., & Chow, T.H. (2004). Severe Weather in HK, *HKO bulletin.*

Grimmond, C.S.B. (1992). The suburban energy balance: Methodological considerations and results for a mid-latitude west coast city under winter and spring conditions. International Journal of Climatology, 12, 481- 497.

Grimmond, C. S. B., H. A. Cleugh. (1994). A simple method to determine obukhov lengths for suburban areas. *, J. Appl. Meteor.*, 435-440.

Grimmond, C.S.B., & Oke, T.R. (1999). Aerodynamic properties of urban areas derived from analysis of surface form. *Journal of Applied Meteorology, 38,* 1262-1292.

Hallenbeck, M., Rice, M., Smith, B., Cornell-Martinez, C., & Wilkinson, J. (1997). Vehicle Volume Distribution by Classification. [Online]. Available from: http://depts.washington.edu/trac/bulkdisk/pdf/VVD_CLASS.pdf, Accessed July, 15th, 2009.

Hamilton, I.G., Davies, M., Steadman, P., Stone, A., Ridley, I., & Evans, S. (2009). The significance of the anthropogenic heat emissions of London's buildings: A comparison against captured shortwave solar radiation. Building and Environment, 44, 807-817.

Harrison, R., McGoldrick, B., & Williams, C.G.B. (1984). Artificial heat release from greater London, 1971–1976. *Atmospheric Environment* (1967), 18, 2291-2304.

Heiple, S., & Sailor, D.J. (2008). Using building energy simulation and geospatial modeling techniques to determine high resolution building sector energy consumption profiles. *Energy and Buildings, 40*, 1426-1436.

Hernandez-Baquero, E. (2000). Characterization of the Earth’s Surface and Atmosphere from Multispectral and Hyperspectral Thermal Imagery. Ph.D. Dissertation, Rochester Institute of Technology, Chester F. Carlsom Center for Imaging Science, Rochester, NY.

Högström, U. (1988). Non-dimensional wind and temperature profiles in the atmospheric surface layer: A re-evaluation. *Boundary-Layer Meteorology, 42*, 55-78.

Ichinose, T., Shimodozono, K., & Hanaki, K. (1999). Impact of anthropogenic heat on urban climate in Tokyo. Atmospheric Environment, 33, 3897-3909.

Johnson, B. R., & Young, S. J. (1998). In-Scene Atmospheric Compensation: Application to SEBASS Data Collected at the ARM Site. Technical Report, Space and Environment Technology Center, the Aerospace Corporation.

Kahle, A. B., Madura, D.P. and Soha. J.M. (1980). Middle infrared multispectral aircraft scanner data: analysis for geological applications, *Appl. Opt.*, *19(14)*, 2279 – 2290.

Kato, S., & Yamaguchi, Y. (2005). Analysis of urban heat-island effect using ASTER and ETM+ Data: Separation of anthropogenic heat discharge and natural heat radiation from sensible heat flux. *Remote Sensing of Environment, 99*, 44-54.

Kato, S., & Yamaguchi, Y. (2007). Estimation of storage heat flux in an urban area using ASTER data. *Remote Sensing of Environment, 110*, 1-17.

Kato, S., Yamaguchi, Y., Liu, C.-., & Sun, C.-. (2008). Surface heat balance analysis of Tainan City on March 6, 2001 using ASTER and Formosat-2 data. *Sensors, 8*, 6026-6044.

Kato, S., Liu, C.-., Chen, P.-., Sun, C.-., Tsai, H.-., & Yamaguchi, Y. (2009). Heat balance analysis in Taiwanese cities using aster and formosat-2 data. *30th Asian Conference on Remote Sensing 2009, ACRS 2009, 3*, 1739-1744

Klysik, K. (1996). Spatial and seasonal distribution of anthropogenic heat emissions in Lodz, Poland. Atmospheric Environment, 30, 3397-3404.

Kondo, H., & Kikegawa, Y. (2003). Temperature variation in the urban canopy with anthropogenic energy use. Pure and Applied Geophysics, 160, 317-324.

Kotchenova, S.Y., Vermote, E.F., Matarrese, R., & Klemm, F.J., Jr. (2006). Validation of a vector version of the 6S radiative transfer code for atmospheric correction of satellite data. Part I: Path radiance. *Applied Optics,* 45(26), 6726-6774.

Kyle, B. (1999) Hong Kong Meteorological Society – Bulletin, Volume 3, Number 1.

Lam, J.C. (1995). Degree-day climate parameters for Hong Kong. International Journal of Ambient Energy, 16, 209-218.

Lee, B. Y., Mok, H. Y., & Lee, T. C. (2010). Reprint 920. The Latest on Climate Change in Hong Kong and its Implications for the Engineering Sector Presented by DHKO in the HKIE Conference on Climate Change – Hong Kong Engineers ' Perspective, 18-19 October 2010. THE LATEST ON CLIMATE CHANGE IN HONG (pp. 18–19).

Lee, S.-., Song, C.-., Baik, J.-., & Park, S.-. (2009). Estimation of anthropogenic heat emission in the Gyeong-In region of Korea. *Theoretical and Applied Climatology, 96*, 291-303.

Lemonsu, A., *&* Masson, V. *(*2002). Simulation of a summer urban breeze over Paris. Boundary-Layer Meteorology, *104*, 463–490.

Liang, S. (2001). Narrowband to broadband conversions of land surface albedo. *Remote Sensing of Environment, 76*, 213-238.

Lindberg, F., Grimmond, C.S.B., Yogeswaran, N., Kotthaus, S., & Allen, L. (2013). Impact of city changes and weather on anthropogenic heat flux in Europe 1995–2015. Urban Climate, 4, 1-15.

Lu, D., & Weng, Q. (2006). Spectral mixture analysis of ASTER images for examining the relationship between urban thermal features and biophysical descriptors in Indianapolis, Indiana, USA. *Remote Sensing of Environment, 104*, 157-167.

Macdonald, R.W., Griffiths, R.F., & Hall, D.J. (1998). An improved method for the estimation of surface roughness of obstacle arrays. *Atmospheric Environment, 32*, 1857-1864.

Makar, P.A., Gravel, S., Chirkov, V., Strawbridge, K.B., Froude, F., Arnold, J., *et al.* (2006). Heat flux, urban properties, and regional weather. Atmospheric Environment, 40, 2750-2766.

Masson, V. (2000). A physically-based scheme for the urban energy budget in atmospheric models. Boundary-Layer Meteorology, *94*, 357–397.

Martilli, A, Clappier A, & Rotach M.W. (2002). An urban surface exchange parameterisation for messocale models. Boundary-Layer Meteorology, *104*, 261–304.

MHU&RD. (2005). The Ministry of Housing and Urban-Rural Development, the People Republic of China. Design Standard for Energy Efficiency of Residential Buildings in Hot Summer and Cold Winter Zone.

Myrup, L.O. (1969). A numerical model of the urban heat island. Journal of Applied Meteorology, *8*, 908–918.

NASA Technical Reports Server (2014) - Equations for the determination of humidity from dew point and psychometric data, *http://www.nasa.gov/centers/dryden/pdf/87878main_H-937.pdf*.

Newcombe, K. (1975). Energy use in Hong Kong: Part I, an overview. Urban Ecology, 1, 87-113.

Nichol, J. (2005). Remote sensing of urban heat islands by day and night. *Photogrammetric Engineering and Remote Sensing*, *71*, 613-621.

Nichol, J.E., &Wong, M.S. (2008). Spatial variability of air temperature and appropriate resolution for satellite-derived air temperature estimation. *International Journal of Remote Sensing*, 29(24), 7213-7223.

Nichol, J.E., Fung, W.Y., Lam, K.-., & Wong, M.S. (2009). Urban heat island diagnosis using ASTER satellite images and 'in situ' air temperature. *Atmospheric Research*, *94*, 276-284.

Nichol, J. (2009). An emissivity modulation method for spatial enhancement of thermal satellite images in urban heat island analysis. *Photogrammetric Engineering and Remote Sensing*, *75*, 547-556.

Nicodemus, F. E. (1965). Directional reflectance and emissivity of an opaque surface. *Applied Optics*, 4, 767-773.

Nicol, J.F., & Humphreys, M.A. (2002). Adaptive thermal comfort and sustainable thermal standards for buildings. Energy and Buildings, 34, 563-572.

Oke, T.R. (1987). Boundary Layer Climates, *Second edition, ISBN 0-415-04319-0.*

Oke, T.R. (1988). The urban energy balance. *Progress in Physical Geography, 12*, 471-508.

Otte T.L., Lacser, A., Dupont, S., & Ching, J.K.S. *(*2004). Implementation of an urban canopy parameterization in a mesoscale meteorological model. Journal of Applied Meteorology, *43*, 1648–1665.

Paulson CA. (1970). Mathematical representation of wind speed and temperature profiles in the unstable atmospheric surface layer. *Journal of Applied Meteorology, 9*, 857-861

Pigeon, G., Legain, D., Durand, P., & Masson, V. (2007). Anthropogenic heat release in an old European agglomeration (Toulouse, France). International Journal of Climatology, 27, 1969-1981.

Planning Department (2013). *Land utilization in Hong Kong* [online]. Available from: http://www.pland.gov.hk/pland_en/info_serv/statistic/landu.html, Accessed May, 23rd, 2013.

Prata, A.J. (1996). A new long-wave formula for estimating downward clear-sky radiation at the surface. *Quarterly Journal of the Royal Meteorological Society*, *122*, 1127-1151.

Quattrochi, D.A., & Luvall, J.C. (1999). Thermal infrared remote sensing for analysis of landscape ecological processes: Methods and applications. *Landscape Ecology*, *14*, 577-598.

Ren, C., & Ng, E. (2007). An investigation of ventilation at ground level in high density cities - An initial study in Hong Kong. *Sun, Wind and Architecture - The Proceedings of the 24th International Conference on Passive and Low Energy Architecture, PLEA 2007*, 155-160.

Richardson, R., & Brusasca, G. (1989). Numerical experiments on urban heat island intensity. Quarterly Journal of Royal Meteorological Society, *115*, 983–995.

Roth, M., Oke, T.R., & Emery, W.J. (1989). Satellite-derived urban heat islands from three coastal cities and the utilization of such data in urban climatology *International Journal of Remote Sensing*, *10*, 1699 – 1720.

Sailor, D.J., & Lu, L. (2004). A top-–down methodology for developing diurnal and seasonal anthropogenic heating profiles for urban areas. Atmospheric Environment, 38, 2737 -2748.

Sailor, D.J. (2011). A review of methods for estimating anthropogenic heat and moisture emissions in the urban environment. International Journal of Climatology, 31, 189-199.

Smith, C., Lindley, S., & Levermore, G. (2009). Estimating spatial and temporal patterns of urban anthropogenic heat fluxes for UK cities: The case of Manchester. Theoretical and Applied Climatology, 98, 19-35.

Taha, H. (1997). Urban climates and heat islands: Albedo, evapotranspiration, and anthropogenic heat. *Energy and Buildings*, 25, 99-103.

Transport Department (2013). *The Annual Traffic Census* [online]. Available from: http://www.td.gov.hk/en/publications_and_press_releases/publications/free_publications/the_annual_traffic_census_2012/index.html, Accessed May, 23rd, 2013.

United Nations Population Fund (UNFPA) (2011). Urbanization: A Majority in Cities: Population & Development. http://www.unfpa.org/pds/urbanization.htm.

United States Environmental Protection Agency (2013) Heat Island Effect | U.S. EPA. http://www.epa.gov/heatisland/.

Verma, S.B. (1989). Aerodynamic resistances to transfers of heat, mass and momentum. *Estimation of Areal Evapotranspiration, 177*, 13-20.

Vermote, E.F., El Saleous, N.Z., Justice, C.O., Kaufman, Y.J., Privette, J., Remer, L. Roger, J.-C., & Tanré, D. (1997). Atmospheric correction of visible to middle infrared EOS-MODIS data over land surface, background, operational algorithm and validation. *J. Geophysical Research*. 102, 17131-17141.

Voogt, J.A., & Oke, T.R. (1998). "Effects of urban surface geometry on remotely-sensed surface temperature," *Int. J. Remote Sensors*, *19*, 895-920.

Voogt, J.A., & Grimmond, C.S.B. (2000). Modeling surface sensible heat flux using surface radiative temperatures in a simple urban area. *Journal of Applied Meteorology, 39*, 1679-1699.

Voogt, J.A., & Oke, T.R. (2003). Thermal remote sensing of urban climates. *Remote Sensing of Environment*, *86*, 370-384.

Weng, Q., Liu, H., Liang, B., & Dengsheng, Lu. (2008). The Spatial Variations of Urban Land Surface Temperatures: Pertinent Factors, Zoning Effect, and Seasonal Variability *IEEE Journal of Selected Topics in Applied Earth Observations and Remote Sensing*, *1*, 154 -166

Weng, Q., & Hu, X. (2008). Medium spatial resolution satellite imagery for estimating and mapping urban impervious surfaces using LSMA and ANN. *IEEE Transactions on Geoscience and Remote Sensing, 46*, 2397-2406.

Wong, M.S., Nichol, J.E., To, P.H., & Wang, J. (2010). A simple method for designation of urban ventilation corridors and its application to urban heat island analysis *Building and Environment, 45*, 1880-1889.

Wong, M.S., & Nichol, J.E. (2013). Spatial variability of frontal area index and its relationship with urban heat island intensity. *International Journal of Remote Sensing, 34*, 885-896.

Worldmapper. (2011). Transport maps. [Online]. Available from: http://www.worldmapper.org/textindex/text_transport.html, Accessed June, 30th, 2011.

World Travel Guide. (2009). Travel Guide Information: Country Guides. [Online]. Available from: http://www.worldtravelguide.net/country/countries.ehtml, Accessed June, 30th, 2009.

Xu, W., Wooster, M.J., & Grimmond, C.S.B. (2008). Modelling of urban sensible heat flux at multiple spatial scales: A demonstration using airborne hyperspectral imagery of Shanghai and a temperature-emissivity separation approach. *Remote Sensing of Environment, 112*, 3493-3510.

Zhou, Y., Weng, Q., Gurney, K.R., Shuai, Y., & Hu, X. (2012). Estimation of the relationship between remotely sensed anthropogenic heat discharge and building energy use. *ISPRS Journal of Photogrammetry and Remote Sensing, 67*, 65-72.

Zhang, Y., Balzter, H., & Wu, X. (2013). Spatial-temporal patterns of urban anthropogenic heat discharge in Fuzhou, China, observed from sensible heat flux using Landsat TM/ETM+ data. *International Journal of Remote Sensing, 34*, 1459-1477.